PB-223 003

NITRIC OXIDE FORMATION IN COMBUSTION PROCESSES WITH STRONG RECIRCULATION

UNITED AIRCRAFT RESEARCH LABORATORIES

PREPARED FOR
ENVIRONMENTAL PROTECTION AGENCY

JULY 1973

DISTRIBUTED BY:

NTIS
National Technical Information Service
U. S. DEPARTMENT OF COMMERCE

PB 223 003

EPA-R2-73-291

July 1973

Environmental Protection Technology Series

NITRIC OXIDE FORMATION IN COMBUSTION PROCESSES WITH STRONG RECIRCULATION

Reproduced by
NATIONAL TECHNICAL
INFORMATION SERVICE
U S Department of Commerce
Springfield VA 22151

Office of Research and Monitoring
U.S. Environmental Protection Agency
Washington, D.C. 20460

BIBLIOGRAPHIC DATA SHEET	1. Report No. EPA-R2-73-291	2.	3. Recipient's Accession No. PB-222 066
4. Title and Subtitle Nitric Oxide Formation in Combustion Processes with Strong Recirculation			5. Report Date July 1973 6.
7. Author(s) C. T. Bowman, L. S. Cohen, and M. N. Director			8. Performing Organization Rept. No.
9. Performing Organization Name and Address United Aircraft Research Laboratories East Hartford, Connecticut 06108			10. Project/Task/Work Unit No. 11. Contract/Grant No. 68-02-0252
12. Sponsoring Organization Name and Address EPA, Office of Research and Development NERC-RTP, Control Systems Laboratory Research Triangle Park, North Carolina 27711			13. Type of Report & Period Covered Final 14.

15. Supplementary Notes

16. Abstracts This reports the results of an investigation of NO formation in a premixed turbulent flame stabilized on the recirculation zone (RZ) downstream from a bluff-body. Objectives were to investigate factors affecting NO formation in the RZ and to assess the relative importance of NO production in the RZ to overall NO production. To characterize NO formation in the RZ, dependence of NO formation on the RZ volume, temperature and residence time of the gas in the RZ, and O-atom concentration in the RZ were determined. NO production in the RZ was strongly influenced by non-equilibrium chemical effects and by the turbulent exchange processes. Data on turbulent exchange was obtained in a complementary investigation of RZ fluid dynamics in non-reacting flows. Comparison of volumetric NO production rates in the RZ with overall volumetric NO production rates indicates that, for the experimental configuration, NO production in the RZ is not a major factor in overall NO formation. An analytical model for NO production in the burner was developed. Results from this model suggest that the RZ can be a major factor in NO production in practical combustion devices.

17. Key Words and Document Analysis. 17a. Descriptors
Air Pollution
Nitrogen Oxide (NO)
Circulation
Combustion
Turbulent Flow
Mathematical Models

17b. Identifiers/Open-Ended Terms
Air Pollution Control
Stationary Sources
Recirculating Flow

17c. COSATI Field/Group 21B, 13B

18. Availability Statement	19. Security Class (This Report)	21. No. of Pages
Unlimited	UNCLASSIFIED	~~145~~ 144
	20. Security Class (This Page) UNCLASSIFIED	22. Price $4.50 ~~$1.45~~

EPA-R2-73-291

NITRIC OXIDE FORMATION IN COMBUSTION PROCESSES WITH STRONG RECIRCULATION

by

C.T. Bowman, L.S. Cohen, and M.N. Director

United Aircraft Research Laboratories
East Hartford, Connecticut 06108

Contract No. 68-02-0252
Program Element No. 1A2014

EPA Project Officer: G.B. Martin

Control Systems Laboratory
National Environmental Research Center
Research Triangle Park, North Carolina 27711

Prepared for

OFFICE OF RESEARCH AND MONITORING
U.S. ENVIRONMENTAL PROTECTION AGENCY
WASHINGTON, D.C. 20460

July 1973

10

This report has been reviewed by the Environmental Protection Agency and approved for publication. Approval does not signify that the contents necessarily reflect the views and policies of the Agency, nor does mention of trade names or commercial products constitute endorsement or recommendation for use.

ABSTRACT

An investigation of NO formation in a premixed, turbulent flame stabilized on the recirculation zone downstream from a bluff-body has been carried out. The objectives of this investigation were to investigate the factors affecting NO formation in the recirculation zone and to assess the relative importance of NO production in the zone to overall NO production.

The dependence of NO formation in the recirculation zone on the properties of the zone was determined. NO production in the recirculation zone was strongly influenced by non-equilibrium chemical effects and by turbulent exchange processes. Information on turbulent exchange was obtained in a complementary investigation of recirculation zone fluid dynamics in non-reacting flows. Comparison of NO production in the recirculation zone with overall NO production indicates that, for the experimental configuration, the recirculation zone is not a major factor in overall NO production.

An analytical model for NO production in the burner was developed. Results from this model suggest that the recirculation zone can be a major factor in NO production in practical combustion devices.

This report was submitted in fulfillment of Contract 68-02-0252, by United Aircraft Research Laboratories, under the sponsorship of the Environmental Protection Agency. Work was completed as of March 1973.

CONTENTS

		Page
Abstract		iii
List of Figures		vi
List of Tables		x
Acknowledgments		xi
Sections		
I	Introduction	1
II	Background Information	3
III	Combustion Experiments	12
IV	Cold Flow Experiments	51
V	Analytical Investigation	78
VI	Conclusions	103
VII	References	105
VIII	Nomenclature	109
IX	Appendices	113

Preceding page blank

FIGURES

No.		Page
1	Wake Flow Behind Circular Cylinder	6
2	Schematic Diagram of the Two-Dimensional Burner Facility	13
3	Typical Velocity Profile at the Test Section Entrance	14
4	Two-Dimensional Test Section with Injecting Flameholder	15
5	Stability Limits for Methane-Air Flames in Two-Dimensional Burners with 0.32-cm Diameter Cylindrical Flameholders	16
6	Spark Schlieren Photograph of a Methane-Air Flame	20
7a	Typical Dependence of Recirculation Zone Length/Flameholder Diameter on Inlet Velocity	21
7b	Typical Dependence of Maximum Recirculation Zone Width/ Flameholder Diameter on Inlet Velocity	22
8	Dependence of Recirculation Zone Volume on Inlet Velocity and Equivalence Ratio for Methane-Air Mixtures	23
9	Time-Exposure (1/500 Sec) Schlieren Photograph of a Methane-Air Flame	26
10a	Typical Dependence of the Maximum Flame Angle on Inlet Velocity for a Stoichiometric Methane-Air Mixture	27
10b	Typical Dependence of the Maximum Flame Angle on Equivalence Ratio for Methane-Air Mixtures	28
11	Typical Temperature Distribution in the Recirculation Zone	31
12	Typical Dependence of Recirculation Zone Temperature on Equivalence Ratio	32
13	Typical Dependence of Recirculation Zone Temperature on Inlet Velocity	33

No.		Page
14	Dependence of Mean Residence Time on Inlet Velocity, Equivalence Ratio and Measurement Location	37
15	Hydroxyl Radical Concentration in the Recirculation Zone as a Function of Equivalence Ratio and Inlet Velocity	41
16a	Typical Dependence of Nitric Oxide Concentration in the Recirculation Zone on Equivalence Ratio and Measurement Location	44
16b	Typical Dependence of Nitric Oxide Concentration in the Recirculation Zone on Inlet Velocity	45
17a	Typical Species Concentration Profiles at the Exhaust of the Combustion Test Section	46
17b	Typical Nitric Oxide Concentration Profiles at the Exhaust of the Combustion Test Section	47
18	Cold Flow Fluid Dynamics Test Facility	52
19	Schematic Daigram of Cold Flow Fluid Dynamics Test Section	53
20	Fiber Optic Probe	56
21	Typical Velocity Profiles in Cold Flow Test Section	57
22	Cold Flow Test Section with Hot Wire Probe Installed	58
23	Turbulence Level Downstream of Screens	60
24	Schlieren Photograph of Near-Wake Region	63
25	Vortex Shedding Sequence	64
26	Recirculation Zone Geometrical Characteristics	65
27	Residence Time Determination	67
28	Residence Time Correlating Parameter for Cold Flow	69
29	Oscilloscope Trace of Typical Tracer Concentration Distribution	71

No.		Page
30	Axial Variation of Temperature in Recirculation Zone	72
31	Typical Tracer Centerline Concentration Distribution	73
32	Tracer Concentration Distribution on Recirculation Zone Centerline	74
33	Tracer Concentration Contour Map	75
34	Analytical Model	85
35	Methane-Air Ignition Delay Time	91
36	Calculated Flame Boundary	98
37	Calculated Wake Velocity Profile	99
38	NO Concentration Distribution	100
39	Calculated Species Distributions	101
A-1	Schematic Diagram of the Schlieren Optical System	115
A-2	Schematic Diagram of the Sodium D-Line Photometer	115
A-3	Typical Experimental Traces Obtained from the Temperature Measurement Experiments	117
A-4	Typical Oscilloscope Trace from Residence Time Experiments	119
A-5	Typical Semi-Logarithmic Plot of Absorption Decay Curve	120
A-6	Schematic Diagram of the UV Photometer	122
A-7	Typical Nitric Oxide Absorption Spectrum-Nitric Oxide Mole Fraction = 2×10^{-3}	124
A-8	Schematic Diagram of Probe and Sampling System Used for Exhaust Concentration Measurements	126
A-9	Sampling Probe in Combustor Exhaust	128

No.		Page
A-10a	Typical Observed Mass Spectra of the Combustor Exhaust in the Range m/e = 28-30	129
A-10b	Typical Deconvolved Mass Spectra	129
B-1	Schematic Diagram of Fiber Optic Instrumentation	132
B-2	Component and System Performance of Fiber Optic Probe for NO_2-N_2O_4 Tracer	132
B-3	Properties of NO_2-N_2O_4 Tracer	133

TABLES

No.		Page
I	Residence Times for Three-Dimensional Bluff Bodies	11
II	Combustion Test Matrix	18
III	Recirculation Zone Volume and Flame Spreading Rates	24
IV	Recirculation Zone Temperatures	34
V	Mean Residence Times	36
VI	OH Concentration	40
VII	Nitric Oxide Concentrations in Recirculation Zone	42
VIII	Nitric Oxide Concentrations in Exhaust Gas	48
IX	Ratio of Nitric Oxide Production in the Recirculation Zone to Total Nitric Oxide Production	50
X	Screens for Turbulence Production	59
XI	Cold Flow Test Matrix	62
XII	Residence Times and Correlation Parameter	68
XIII	Tracer Concentration Distribution Data	76
XIV	Summary of Analytical Results	96

ACKNOWLEDGMENTS

The time-of-flight mass spectrometer used in the combustion experiments was designed by Dr. M. F. Zabielski. His assistance with the exhaust sampling portion of the combustion experiments is gratefully acknowledged.

The authors thank Dr. L. J. Coulter, Mr. Richard Roback, Mr. David B. Smith and Mrs. L. Rufleth for their help in the analytical investigation. In addition, the authors thank Mr. J. L. Wright and Mr. R. Smus for valuable assistance in the experimental program.

This research program was carried out under the sponsorship of the Environmental Protection Agency, Durham, North Carolina with Dr. G. Blair Martin as Project Officer.

SECTION I

INTRODUCTION

Recent experimental investigations of factors affecting pollutant emissions from various continuous combustion systems (Refs. 1-3) have shown that changes in operating conditions, which alter the flow patterns in the combustion chamber, can have a substantial effect on nitrogen oxide emissions. This observation suggests that coupling between fluid dynamic and chemical processes in the combustion chamber is a major factor governing nitrogen oxide emissions. In many practical continuous combustion systems, such as furnaces and gas turbines, the flame is stabilized by a primary combustion zone, characterized by strong recirculation patterns. Because of the high temperatures and relatively long residence times associated with these regions, it appears likely that a substantial amount of nitric oxide formation occurs in the recirculation zones. Hence, changes in operating conditions which alter recirculation zone characteristics -- notably recirculation zone size and the temperature and residence time of gas in the zone -- can be expected to produce changes in nitrogen oxide emissions. To gain an initial understanding of how coupling between fluid dynamic and chemical processes in a combustion device governs nitrogen oxide emissions, one can first examine the nitric oxide formation process in recirculation zones.

The present report documents the results of an investigation, sponsored by EPA Contract 68-02-0252, of nitric oxide formation in a combustion process with strong recirculation. The objectives of this investigation were to (a) investigate the factors affecting nitric oxide formation in the recirculation zone and (b) assess the relative importance of nitric oxide production in the recirculation zone to overall nitric oxide production.

In this investigation, a simplified experimental configuration was used to permit detailed examination of the nitric oxide formation process in the combustor as burner input parameters (fuel/air ratio and inlet velocity) were varied. To assist in interpretation of the experimental results and to permit extrapolation of these results to conditions outside the range of the present study, an analytical model for nitric oxide formation in the model combustor was developed. To obtain necessary background information on the fluid dynamics of recirculation zones, a detailed experimental investigation of recirculation zones downstream

from bluff-bodies in non-reacting flows was carried out. The various aspects of the investigation, outlined above, are discussed in Sections III, IV, and V.

SECTION II

BACKGROUND INFORMATION

II-A. COMBUSTION EXPERIMENTS

The principal objective of the combustion experiments was to obtain information on the nitric oxide formation process in a continuous flow combustion system in which the flame is stabilized by recirculation. Specifically, the factors affecting nitric oxide production in the recirculation zone were to be identified and the importance of nitric oxide production in the recirculation zone to overall nitric oxide production in the combustor was to be determined.

A simplified experimental configuration was used to permit detailed examination of the nitric oxide formation process in the combustor. In this configuration, a flame was stabilized in a two-dimensional turbulent, premixed, gaseous fuel-air stream by introducing a 0.318-cm diameter cylinder into the flow. The mixture of burned and unburned gases, entrained into the two-dimensional recirculation zone located downstream from the cylinder, served to stabilize the flame in the combustor. A detailed description of the combustor is given in Section III-A.

The amount of nitric oxide produced in the recirculation zone is known to depend on four principal factors -- the recirculation zone volume, the temperature and residence time of the gas in the zone and the O-atom concentration in the zone. To characterize the nitric oxide formation process in the recirculation zone, the dependence of the nitric oxide concentration in the zone on these four factors must be determined. Each of the four factors depends, to a certain extent, on the burner input parameters -- fuel/air ratio, inlet velocity and turbulence level. Hence, to obtain the dependence of nitric oxide production in the recirculation zone on the zone characteristics, the burner input parameters were varied systematically, and the subsequent variations in recirculation zone volume, temperature and residence time of the gas in the zone and O-atom and nitric oxide concentrations in the zone were determined. These data then were used to correlate nitric oxide production in the recirculation zone with the important zone characteristics. To assess the relative importance of the recirculation zone to the overall nitric oxide

formation process, the nitric oxide produced in the recirculation zone was compared to the total nitric oxide produced in the combustor, as measured in the exhaust gas.

Results from the combustion experiments are discussed in Section III, and a detailed description of the experimental techniques is given in Appendix A.

II-B. COLD FLOW EXPERIMENTS

Development of a model for nitric oxide production in the recirculation zone requires knowledge of the turbulent transport processes within the recirculation zone and between the zone and the outer flow. This information was not readily obtained from the combustion experiments due to the high temperature and small size of the stabilizing recirculation zone. To provide some understanding of the turbulent transport processes, the two-dimensional recirculation zone downstream from a 1.59-cm diameter cylinder placed with its axis normal to a cold, nonreacting flow was investigated experimentally. In these tests, a tracer material was injected through holes in the cylinder wall into the recirculation zone where tracer residence times and tracer concentration distributions were determined using a fiber optic probe. Recirculation zone geometry was determined from spark schlieren photographs taken using injected helium tracer. High speed schlieren movies also were obtained to aid in the understanding of the vortex shedding phenomenon encountered with two-dimensional bluff-bodies. Measurements were taken at several approach velocities, free-stream densities and several initial levels of turbulent intensity. Results from the cold flow experiments are discussed in Section IV, and a detailed description of the fiber optic measurement techniques is given in Appendix B.

II-C. FLOW FIELD DOWNSTREAM FROM 2-DIMENSIONAL BLUFF-BODIES

For the Reynolds number range covered in the present experiments the flow in the two-dimensional near-wake downstream from the cylindrical body, which includes the recirculation zone, is categorized as subcritical. In non-reacting flow, the subcritical near-wake regime, which extends from Reynolds numbers of about 300 to 2×10^5, manifests a nearly constant Strouhal number, corresponding to a dominant Kármán vortex double-street instability (Ref. 4). The Strouhal number, or dimensional vortex shedding frequency, is given by

$$Sh \equiv \frac{D}{U_\infty \tau_v} \qquad (1)$$

Figure 1a is a sketch of the incompressible near-wake flow for a circular cylinder, revealing its nonsteady vortex shedding character. The sketch in Fig. 1b is the equivalent mean flow, which is obtained by averaging over times which are large compared to the significant periods of the nonsteady flows, eg., the vortex-shedding period. It has been pointed out in Ref. 5, that the closure point "r" in Fig. 1b occurs in the same region where the vortices complete their growth and then break away. In the Reynolds number range from 1500 to 2×10^5, the predominant phenomenon in the near wake region is the upstream movement of the transition point along the free shear layers, from near the closure point to near the separation point, "s" (Ref. 6). However, at a Reynolds number of about 10^4, the transition point has approached quite close to the cylinder separation point and the major portion of the free shear layer in the near wake is turbulent. For Reynolds numbers in excess of 2×10^5 but less than 3×10^6, comprising the so-called critical flow regime, the vortex shedding is less definite and regular than in the subcritical regime (Ref. 4), and there is strong sensitivity to free stream turbulence and surface roughness. The near-wake characteristics enumerated here for a circular cylinder also are displayed with other two-dimensional bodies such as wedges, although the Reynolds number ranges do not necessarily correspond.

The vortex shedding phenomenon which is characteristic of two-dimensional bluff-body flows under nonreacting conditions, nas not been observed in combusting flows (cf., Ref. 7 and results of the present burner tests). It may be anticipated, therefore, that the nature of the transport processes in a reacting two-dimensional flow field will differ from those in cold flow. Nevertheless, detailed cold flow measurements can be useful in the interpretation and modeling of hot flow data, and in providing a basis of comparison for reacting flows.

II-D. TRANSPORT PROCESSES IN THE NEAR-WAKE REGION

In the analytical treatment of transitional/turbulent shear flows, the local shear stress may be expressed as the product of an eddy viscosity and the local velocity gradient by analogy with the laminar flow representation. However, while the molecular viscosity for laminar flow depends only on the fluid properties, the eddy viscosity is related to the length and time scales which characterize the transition/turbulence structure of the shear flow. At present, transitional/turbulent flow phenomena are not well-understood so that empirical hypothyses are used to create a mathematical basis for the investigation

a) INSTANTANEOUS, NONSTEADY FLOW (WITH VORTEX SHEDDING)

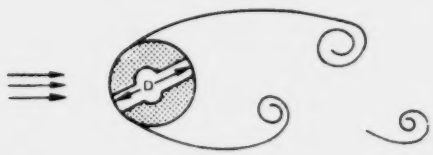

b) MEAN FLOW

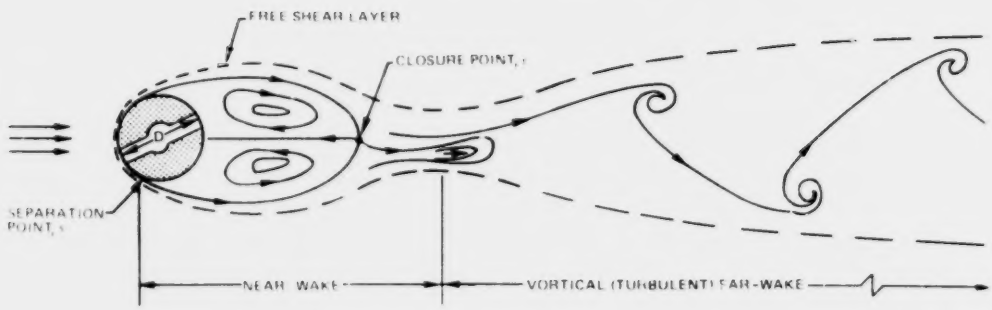

FIG. 1 **WAKE FLOW BEHIND CIRCULAR CYLINDER.**

of such flows. These phenomenological theories lead to a formulation of the eddy viscosity which may be used with the equations of motion and a suitable equation of state to determine the local time-average conditions throughout a flow field.

In any general formulation of the eddy viscosity for two-dimensional bluff-body near-wake flows, it is necessary to consider the body-related turbulence associated with vortex shedding, the turbulence initially present in the flow ("preturbulence"), which may be augmented with the use of mixing aids such as screens, and the turbulence produced as a result of the interactions between the outer flow and the wake. In the Reynolds number range of the present cold flow experiments, it may be expected that the body-related turbulence plays an important role since the well-established vortex shedding produces significant lateral agitation through periodic distortions of the near-wake region. At higher Reynolds numbers, in the critical flow regime, the Strouhal number increases rapidly and the distinctive vortex shedding pattern is lost. Thus, in the critical flow regime, it is anticipated that body-related turbulence is less important than free stream-wake interactions which produce shearing stresses of large magnitude which, in turn, induce high levels of turbulent intensity. The presence of screens or other mixing aids at any Reynolds number will be effective in influencing transport only if the levels of turbulence generated exceed those produced by other competing mechanisms. For any given set of flow conditions, mixing aid geometry and location, and bluff-body geometry and blockage, it is likely that only one of the three turbulence producing mechanisms dominates the transport.

II-D.1. Body-Related Turbulent Transport

For the purpose of developing a formulation of the eddy viscosity for body-related transport and the associated recirculation zone residence time, it is convenient to begin with the basic expression,

$$\epsilon / \hat{\rho} = -\overline{v' \ell'} \qquad (2)$$

(see Ref. 8). Equation 2 relates the eddy viscosity, ϵ, to a parameter associated with the characteristic disturbance size within the turbulence field, ℓ', and the transverse fluctuating velocity or transport velocity, v'. The density $\hat{\rho}$ is some appropriate reference value for the system

under consideration. In the spirit of Prandtl's mixing length hypothesis (cf., Ref. 9), it is assumed that the mean of the product of fluctuating quantities is proportional to the product of the means of the absolute values of these quantities, ie.,

$$\epsilon/\hat{\rho} = -C|\overline{v'}|\cdot|\overline{\ell'}| \tag{3}$$

with the constant c being less than or equal to unity. Since vortex shedding is the phenomenon which characterizes the body-related transport process, it is natural to express the transport velocity as,

$$\overline{|v'|} \sim D/\tau_v \sim (Sh)U_\infty \tag{4}$$

where τ_v is the vortex shedding period and Sh is the Strouhal number. Furthermore, since the laminar separation process on the bluff body, the onset of transition in the shear layer and the formation of the vortex-street must be intimately related (cf., Ref. 5), then

$$\overline{|\ell'|} \sim x_s \sim \delta_s \sim D\sqrt{1/Re} \tag{5}$$

where the Reynolds number is based on the body diameter and approach flow conditions. Thus,

$$\epsilon/\hat{\rho} \sim \frac{(Sh)U_\infty D}{\sqrt{Re}} \tag{6}$$

A relationship between the eddy viscosity and the recirculation zone residence time is established by balancing the quantity of the tracer material within the zone at steady-state conditions with that which is transported out of the zone following suspension of tracer flow into the zone. Thus,

$$y_t \rho_w V_w \sim \frac{\epsilon A_w \tau_t}{D} \tag{7}$$

where τ_t is the residence time and V_w and A_w are the recirculation zone volume and surface area, respectively. The tracer concentration, y_t, and the zone density, ρ_w, are expected to vary throughout the recirculation zone.

If Eqs. 6 and 7 are combined, there results

$$\frac{\tau_t U_\infty}{D} \sim \left(\frac{y_t \rho_w}{\hat{\rho}}\right)\left(\frac{V_w}{A_w D}\right)\frac{\sqrt{Re}}{(Sh)} \qquad (8)$$

Thus, for the present cold flow experiments in which Sh is approximately constant and only a single body diameter is considered, it is predicted that the residence time varies inversely as the square root of the velocity or since $U_\infty \sim (\tau_v)^{-1}$, the residence time varies directly as the square root of the vortex shedding period. The influence of density level on τ_t is not immediately obvious due to the unknown variation of $\hat{\rho}$ in terms of $y_t \rho_w$ and ρ_∞.

II-D.2. Free Stream - Wake Interaction Transport

Turbulence developed due to interactions between streams having different velocities and/or densities typically is characterized in terms of the velocity difference between streams and the transverse extent of the mixing (shear) layer (Ref.10), ie.,

$$\epsilon/\hat{\rho} \sim bU_\infty(1-U_w/U_\infty) \qquad (9)$$

where U_w is some appropriate (mean) wake velocity. Noting that the slope of the mixing layer may be taken as constant (Ref.9), ie., $b \sim L$, it follows that

$$\frac{\tau_t U_\infty}{D} \sim \left(\frac{y_t \rho_w}{\hat{\rho}}\right)\left(\frac{V_w}{A_w D}\right)\frac{D}{L} \qquad (10)$$

where it has been assumed that $U_w << U_\infty$.

The free stream-wake interaction model can be tested by referring to the data of Winterfeld, Ref.11, for three-dimensional bodies in isothermal flow, since no vortex shedding occurs in this case. It was shown in the cited work that the zone volume and surface area are proportional to the product of the zone length and maximum width, ie.,

$$V_w = (0.54 \rightarrow 0.58)LB_M$$

$$A_w = (2.70 \rightarrow 2.90)LB_M$$

independent of velocity in the range 20 to 80 m/sec, for a circular disc,

and 45 deg and 90 deg cones. Thus, at any given velocity, it follows from Eq. 10 that the residence time ratio for any two bluff-bodies varies as,

$$\frac{\tau_{t_1}}{\tau_{t_2}} = \frac{(L/D)_2}{(L/D)_1} \qquad (11)$$

Winterfeld's data for the range of velocity 20-80 m/sec is given in Table I. Also indicated in Table I are the residence times computed from Eq. 11 using the 90 deg cones as a reference, and the error between observed and calculated values. The degree of agreement attained is considered satisfactory.

TABLE I

RESIDENCE TIMES FOR THREE-DIMENSIONAL BLUFF BODIES

BODY	(L/D) – REF. 11	τ_1/U_∞ – REF. 11	CALCULATED τ_1/U_∞	ERROR
CIRCULAR DISC	2.08	0.925	1.11	18%
90 DEG CONE	1.92	1.20	1.20 (REFERENCE)	—
45 DEG CONE	1.67	1.425	1.38	3%

SECTION III

COMBUSTION EXPERIMENTS

III-A. TURBULENT FLAME BURNER

The combustion experiments were carried out in a two-dimensional burner facility, Fig. 2. Methane (Technical Grade) and air (-60°C dew point), metered by calibrated critical flow orifices, enter a mixing chamber through an impinging-type injector. Complete mixing of the methane and air is obtained by flowing the gases through a tightly-packed bed of stainless steel balls. The methane-air mixture flows through stainless-steel calming screens, a 25 to 1 contraction-ratio nozzle and a turbulence-generating screen and enters the test section with essentially a uniform velocity profile, Fig. 3. Four different turbulence-generating screens, 20-, 60-, 100- and 200-mesh stainless-steel screens, with blockages ranging from 33% to 54%, were available for use in the present investigation. The uncooled stainless-steel test section, Fig. 4, is 15 cm long and has a rectangular cross-section (1.27 cm x 3.81 cm). A wall static pressure tap, located near the entrance, is used to measure the test-section pressure drop. The test section is fitted with two fused silica windows to permit visual observation of the flame in the vicinity of the flameholder. A cylindrical flameholder (0.32-cm diameter) is located in the center of the test-section cross-section approximately 1.0 cm downstream from the turbulence generating screen. The flameholder blockage ratio (B_R = flameholder diameter/test section height) was 0.25. Two different types of flameholders were used in the investigation -- a solid, stainless steel rod and a water-cooled, hollow, stainless-steel injecting flameholder (shown in Fig. 4). Most of the experiments were carried out using the solid-rod flameholder. However, when it was necessary to inject tracer material into the recirculation zone (as, for example, in the experiments designed to measure the residence time of gas in the recirculation zone), the injecting flameholder was used. The injecting flameholder is described in greater detail in Appendix A.

The range of stable operating conditions for the two-dimensional burner, using methane-air, is shown in Fig. 5. The solid curve indicates the range of stable operating conditions (inlet velocity and equivalence ratio*) for the uncooled rod flameholder. For inlet velocities and equivalence ratios lying within the bounds of this curve, a flame can

---

*Equivalence ratio, $\phi \equiv \dfrac{\dot{m}_{fuel}/\dot{m}_{air}}{(\dot{m}_{fuel}/\dot{m}_{air})_{stoichiometric}}$

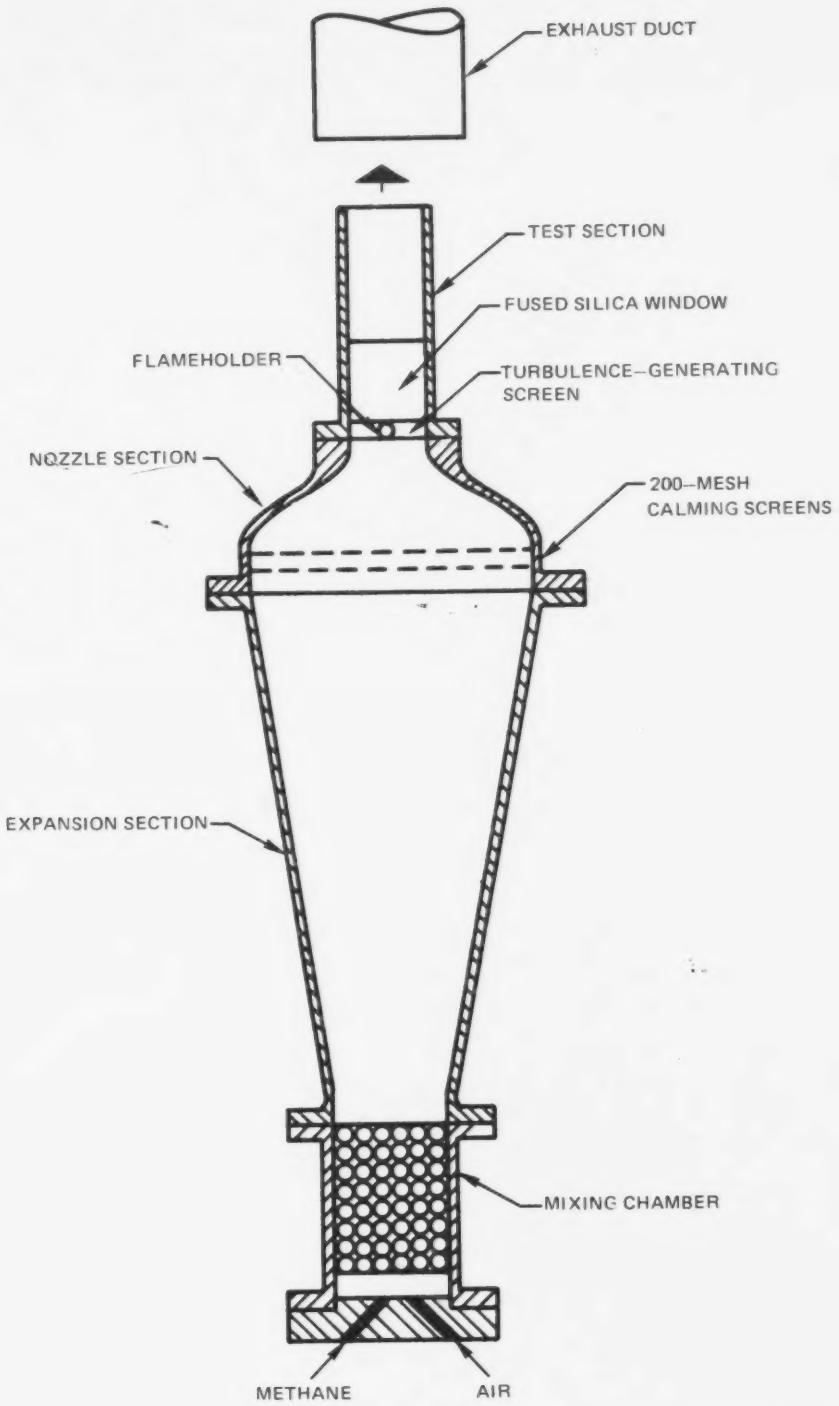

FIG. 2 **SCHEMATIC DIAGRAM OF THE TWO–DIMENSIONAL BURNER FACILITY.**

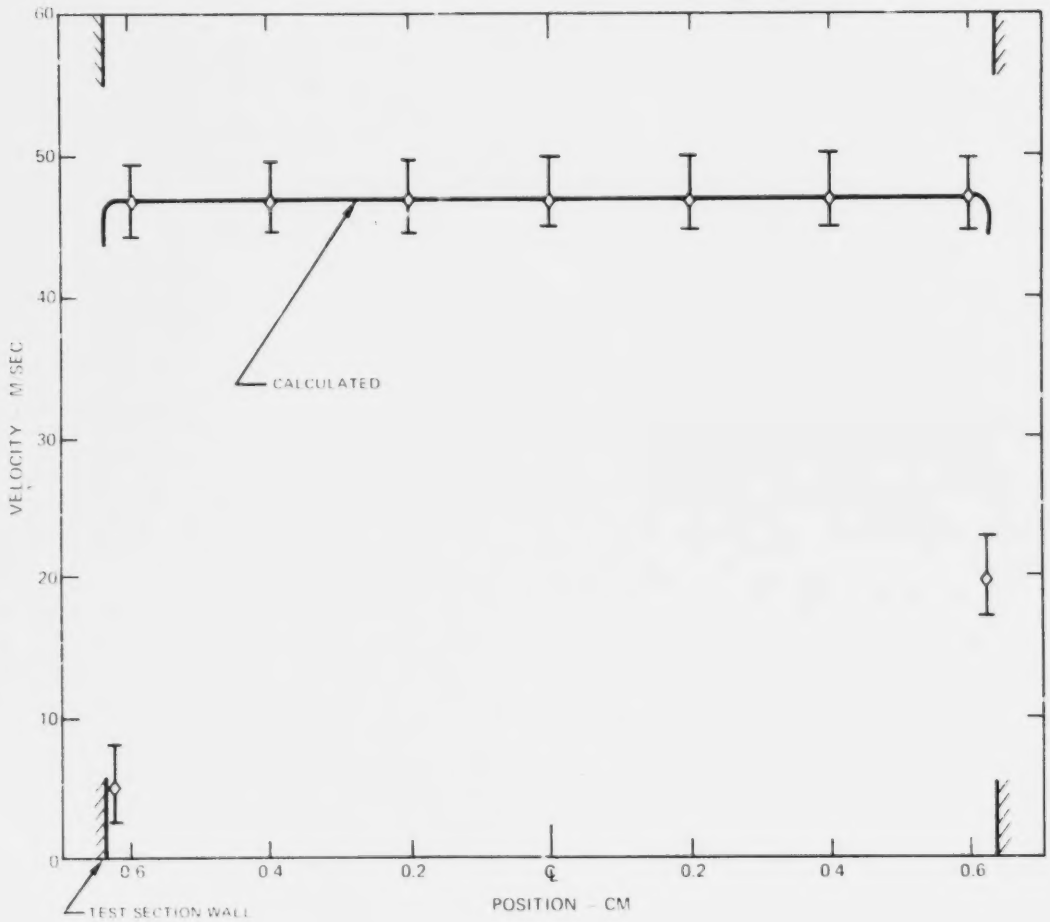

FIG 3 TYPICAL VELOCITY PROFILE AT THE TEST SECTION ENTRANCE.

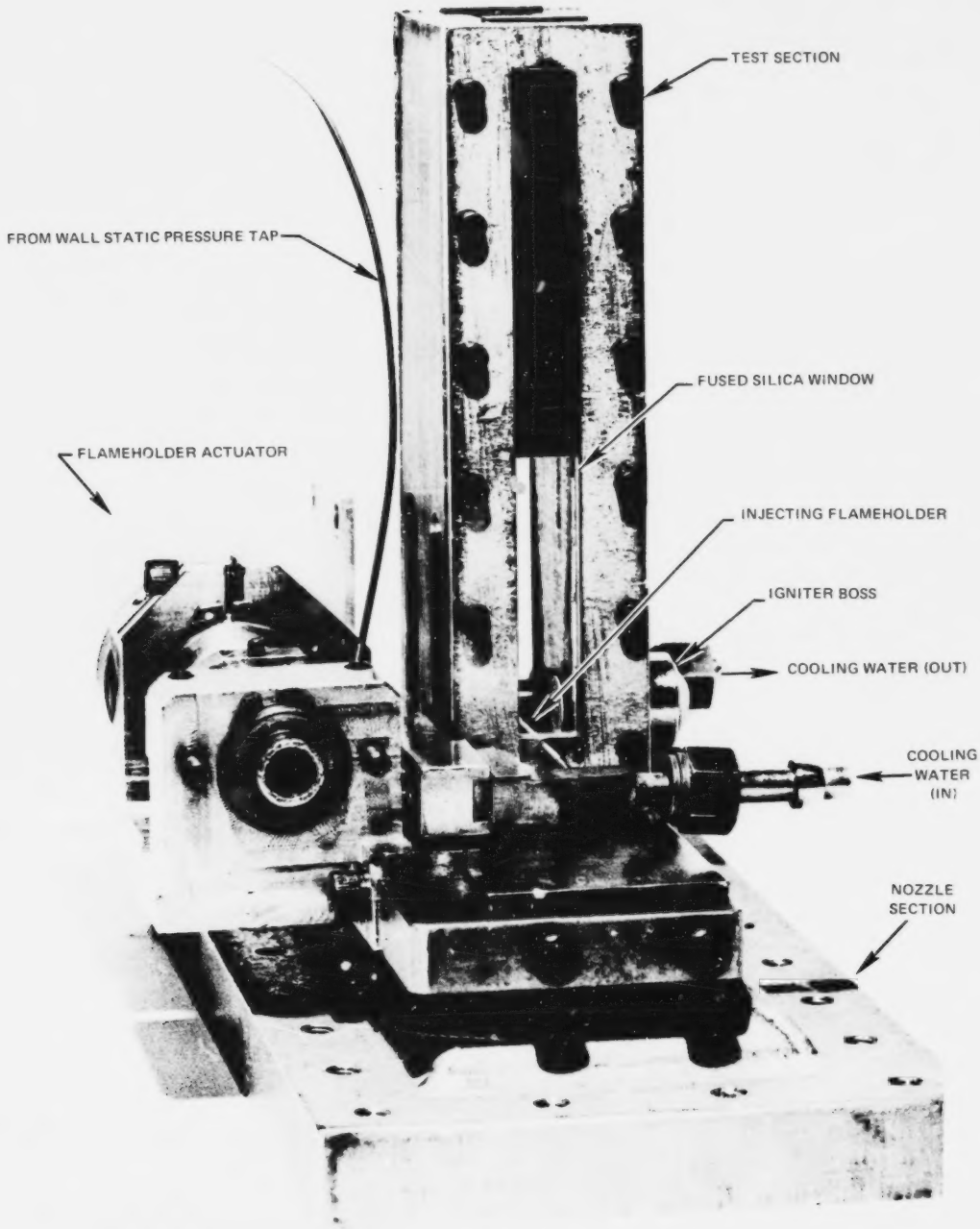

FIG. 4 TWO–DIMENSIONAL TEST SECTION WITH INJECTING FLAMEHOLDER

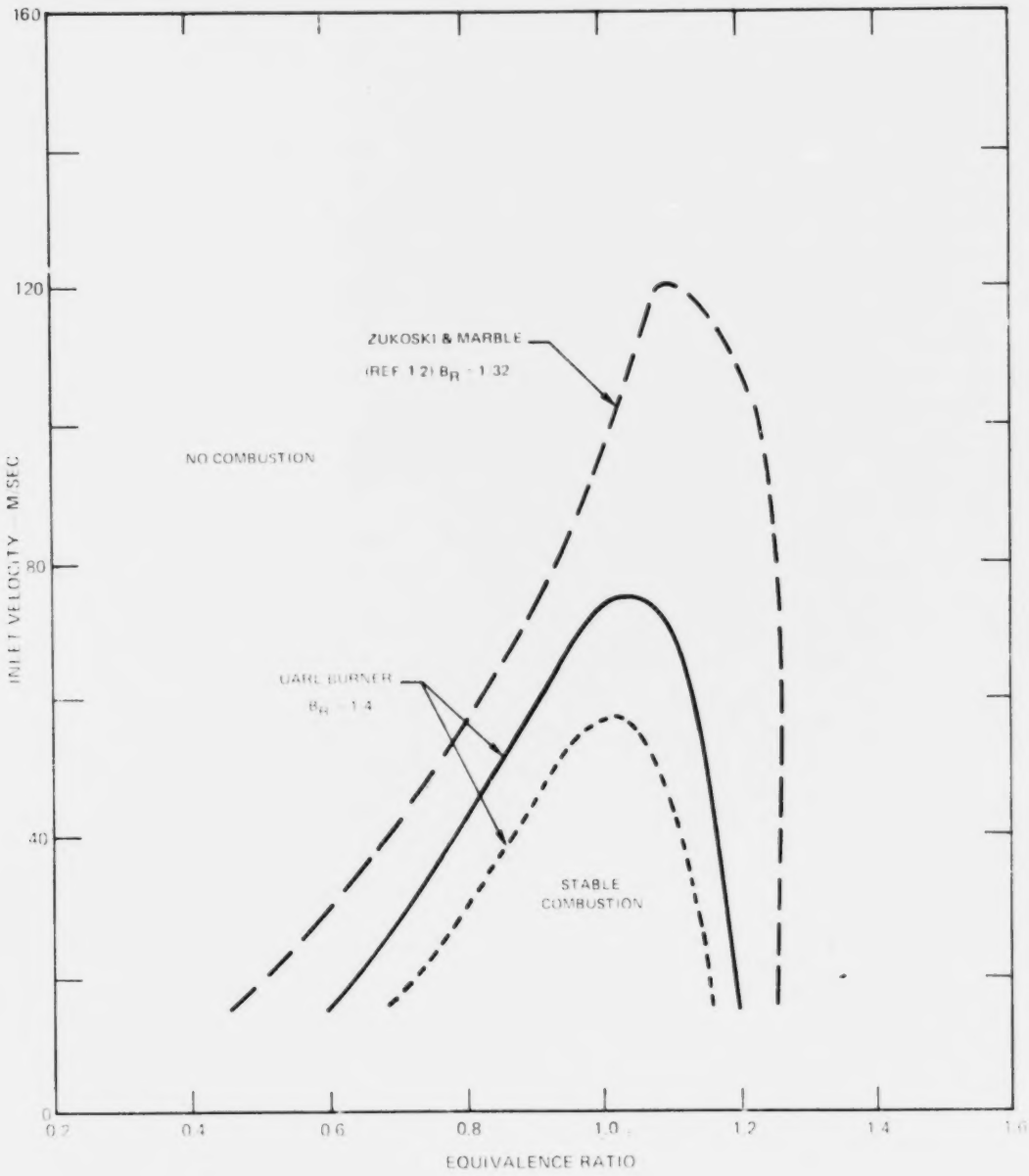

FIG. 5 STABILITY LIMITS FOR METHANE–AIR FLAMES IN TWO–DIMENSIONAL BURNERS WITH 0.32–CM DIAMETER CYLINDRICAL FLAMEHOLDERS.

be stabilized in the test section. For inlet velocities and equivalence ratios lying outside this curve, a flame cannot be stabilized in the test section. The dotted curve indicates the range of stable operating conditions for the cooled, injecting flameholder (with tracer injection). Tracer injection results in a significant reduction in the range of stable operating conditions. No variation in stability limits with the mesh size of the turbulence-generating screens was observed. The dashed curve shows the range of stable operating conditions reported by Zukoski and Marble (Ref.12) for methane-air in a burner with a flameholder blockage ratio of 1/32.

Based on the experimental stability limits, a test matrix was established for combustion experiments. This test matrix, Table II, indicates the nominal test conditions (inlet velocity and equivalence ratio) for which the various experimental measurements were made. The flow visualization experiments, discussed in Section III-B, were carried out to obtain information on recirculation zone geometry and flame spreading rates. The temperature measurement experiments, discussed in Section III-C, provided information on the temperature distribution in the recirculation zone. The residence time measurements, discussed in Section III-D, provided information on the turbulent exchange process between the recirculation zone and the main flow. The OH concentration measurements, discussed in Section III-E, were carried out to obtain information on radical concentrations (OH, O) in the recirculation zone. The NO concentration measurements, discussed in Section III-E, provided information on the nitric oxide concentration in the recirculation zone and in the exhaust gas.

III-B. FLOW VISUALIZATION EXPERIMENTAL RESULTS

The volume of the recirculation zone is an important factor in determining the amount of nitric oxide produced in the zone. For a given volumetric nitric oxide production rate, the total nitric oxide production rate in the recirculation zone is proportional to the volume of the zone. In the present investigation, a spark-source schlieren optical system was used to determine the volume of the recirculation zone located downstream from the flameholder. A schematic diagram and detailed description of the schlieren optical system are given in Appendix A.

The sharp concentration and density gradients associated with the flame surrounding the recirculation zone result in a fairly well-defined

TABLE II

COMBUSTION TEST MATRIX

U_∞ (M/SEC) \ ϕ	0.8	0.9	1.0	1.1
20	F, T, R OH, NO	F, T, R OH, NO	F, T, R OH, NO	F, T, R OH, NO
25	F, T, R	F, T, R OH	F, T, R OH	F, T, R
30	F, T	F, T, R	F, T, R	F, T, R
40		F, T, R NO	F, T, R NO	F, T, R NO
50		F, T	F, T	F, T
60			F NO	F NO

F = FLOW VISUALIZATION
T = TEMPERATURE MEASUREMENT
R = RESIDENCE TIME MEASUREMENT
OH = OH CONCENTRATION MEASUREMENT
NO = NO MEASUREMENT

recirculation zone boundary, Fig. 6. From spark schlieren photographs, such as Fig. 6, the length, width and "cross-sectional" area of the recirculation zone can be determined.

A typical variation of recirculation zone length/flameholder diameter with inlet velocity is shown in Fig.7a. Vertical bars through the present experimental results indicate the uncertainty in recirculation zone length, resulting from the lack of definition in the recirculation zone boundary. Results from two other investigations of two-dimensional bluff-body stabilized flames are shown in Fig. 7a. Wright (Ref.13) measured recirculation zone lengths for two-dimensional hydrocarbon-air flames stabilized on flat plates and cylinders, located transverse to the flow direction. Pein, Peschel and Fetting (Ref.14) reported recirculation zone lengths for a two-dimensional propane-air flames stabilized on a triangular rod. Results from these two studies are consistent with results from the present investigation and indicate that the recirculation zone length increases slightly with increasing inlet velocity for the range of experimental conditions investigated. The recirculation zone length was found to be independent of the mesh size of the turbulence-generating screens.

A typical variation of maximum recirculation zone width/flameholder diameter with inlet velocity is shown in Fig.7b. Vertical bars through the present experimental results indicate the uncertainty in recirculation zone width, resulting from the lack of definition in the recirculation zone boundary. A result from another investigation of recirculation zones in two-dimensional propane-air flames also is shown on Fig.7b. The experimental data indicate that the recirculation zone width is independent of velocity and the mesh size of the turbulence-generating screen for the range of experimental conditions investigated.

The dependence of recirculation zone volume on inlet velocity and equivalence ratio is given in Table III and Fig. 8. The recirculation zone volume was determined using the recirculation zone "cross-sectional area", obtained from the spark schlieren photographs, and the test section width, corrected for boundary layer growth on the test section walls. The vertical bar in Fig.8 indicates the uncertainty in recirculation zone volume, resulting from the lack of definition in the recirculation zone boundary. For the range of experimental conditions investigated, the recirculation zone volume was independent of equivalence ratio and mesh-size of the turbulence-generating screen and increased slightly with increasing inlet velocity.

A careful examination of the spark-schlieren photograph, Fig. 6 , reveals

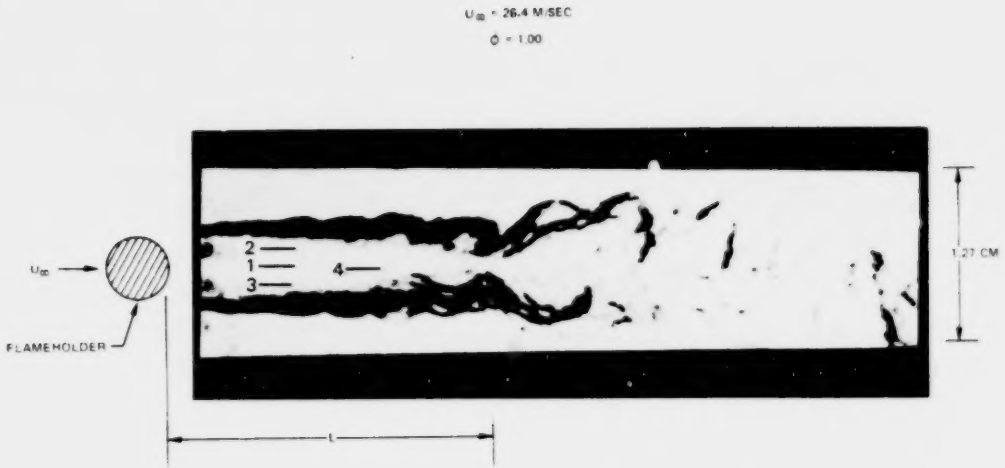

FIG. 6 SPARK SCHLIEREN PHOTOGRAPH OF A METHANE–AIR FLAME.

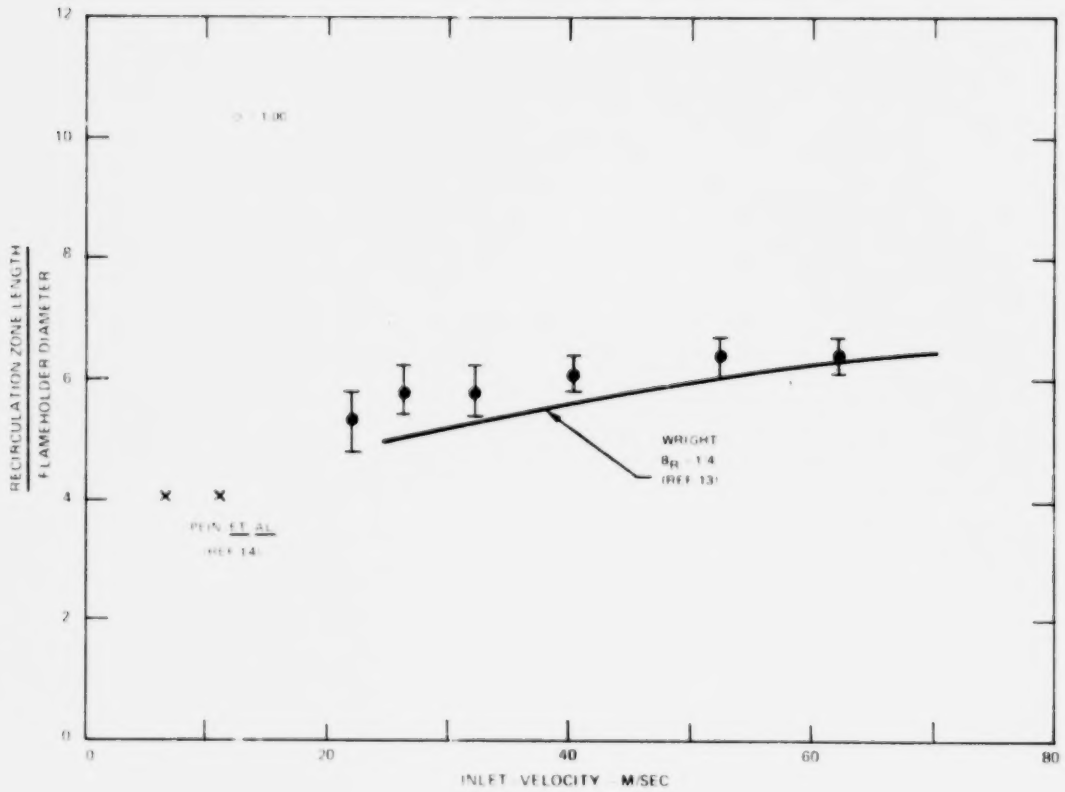

FIG. 7.4 TYPICAL DEPENDENCE OF RECIRCULATION ZONE LENGTH/FLAMEHOLDER DIAMETER ON INLET VELOCITY

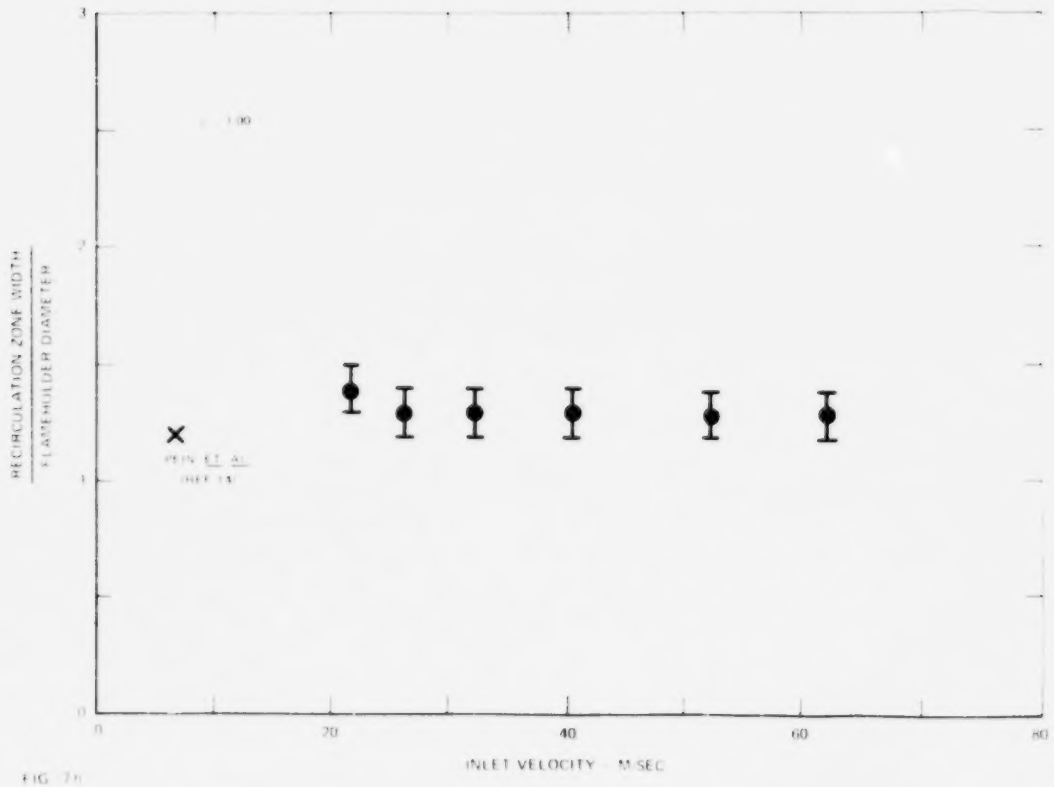

FIG. 7-11

TYPICAL DEPENDENCE OF MAXIMUM RECIRCULATION ZONE WIDTH/FLAMEHOLDER DIAMETER ON INLET VELOCITY

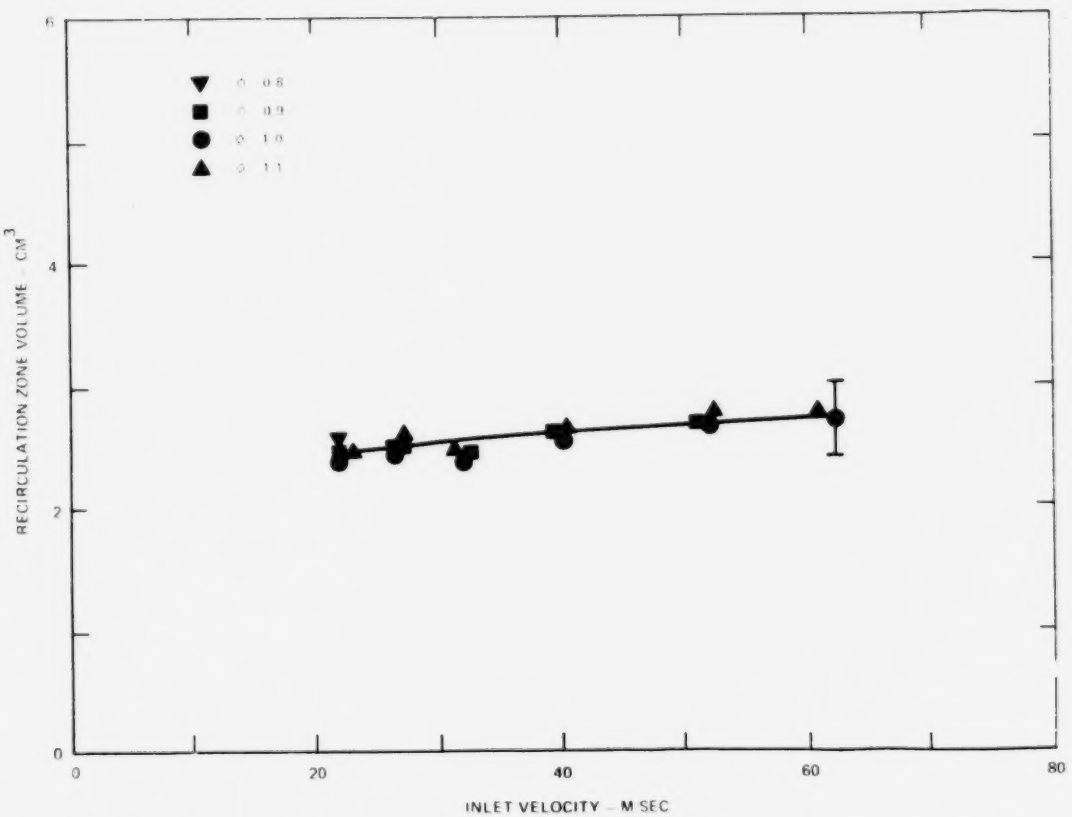

FIG. 8 DEPENDENCE OF RECIRCULATION ZONE VOLUME ON INLET VELOCITY AND EQUIVALENCE RATIO FOR METHANE–AIR MIXTURES.

TABLE III
RECIRCULATION ZONE VOLUME AND FLAME SPREADING RATES

U_∞(M/SEC)	ϕ	V_W (CM^3)	TAN α_{MAX}
21.9	0.83	2.54 $\pm$ 0.30	0.066 $\pm$ 0.07
21.4	0.92	2.45	0.082
21.8	1.01	2.40	0.082
22.6	1.10	2.49	0.086
22.0 *	1.11	2.52	0.084
26.4	0.80	2.52	0.066
26.2	0.89	2.52	0.070
26.4	1.00	2.44	0.076
26.7	1.12	2.61	0.074
31.8	0.81	2.44	0.060
32.5	0.92	2.44	0.070
32.1	1.03	2.40	0.068
31.4	1.10	2.48	0.072
39.5	0.89	2.59	0.066
40.1	1.00	2.55	0.063
40.1	1.10	2.63	0.068
40.2 *	1.10	2.60	0.070
51.2	0.93	2.68	0.060
52.2	1.01	2.68	0.059
52.3	1.11	2.76	0.064
62.0	1.00	2.71	0.058
61.2	1.09	2.79	0.066
61.1 *	1.10	2.80	0.062

100-MESH TURBULENCE SCREEN USED FOR ALL RUNS EXCEPT THOSE MARKED * WHICH USED A 20-MESH TURBULENCE SCREEN

that, in the vicinity of the flameholder, the flame zone is well-defined and appears to be laminar. At a distance downstream of approximately two flameholder diameters, the flame begins to undergo a transition from laminar to turbulent. The transition is essentially complete at a distance downstream of approximately six flameholder diameters, and the flame structure is characterized by random turbulent fluctuations (eddys). At the smallest Reynolds number investigated ($Re = 0.5 \times 10^4$, based on inlet conditions and flameholder diameter), the turbulent transition point occurred very near the end of the recirculation zone. As the Reynolds number was increased, the transition point moved upstream until, at the largest Reynolds number investigated ($Re = 1.4 \times 10^4$), the transition point appeared to be less than one diameter downstream from the flameholder. Zukoski and Marble (Ref.12) have reported similar wake transition phenomena in bluff-body-stabilized hydrocarbon-air flames. The gradual change in the flame zone bounding the recirculation region from laminar to turbulent, with increasing Reynolds number, likely will affect nitric oxide production in the recirculation region due to changes in the recirculation zone characteristics.

To assist in the development of an analytical model for nitric oxide formation in the burner, flame spreading rates in the burner test section were determined as functions of inlet velocity and equivalence ratio. These spreading rates were measured on time-exposure schlieren photographs, taken using the schlieren system with the spark source replaced by a Hg-Xe dc arc lamp. These time-exposure schlieren photographs, Fig. 9, give a time-averaged picture of the reacting flow field. Examination of Fig. 9 reveals that in the vicinity of the recirculation zone the flame spreads very slowly. Downstream from the recirculation zone the flame spreads more rapidly until the flame approaches the test section wall, where the spreading rate decreases. For present purposes, flame spreading in the burner is characterized by the maximum flame spreading rate. This maximum spreading rate is expressed in terms of the tangent of the maximum angle between the leading edge of the flame front and the direction of the approach flow of unburned gas. While determination of the maximum angle is somewhat subject to personal interpretation, several different observers did agree on the angle to within ±10%. Typical experimental results are presented in Fig.10, and all measured flame angles are tabulated in Table III. The vertical bars through the experimental results represent the range of flame angles measured by several different observers. These experimental results will be discussed in detail in the section on analytical modeling, Section V.

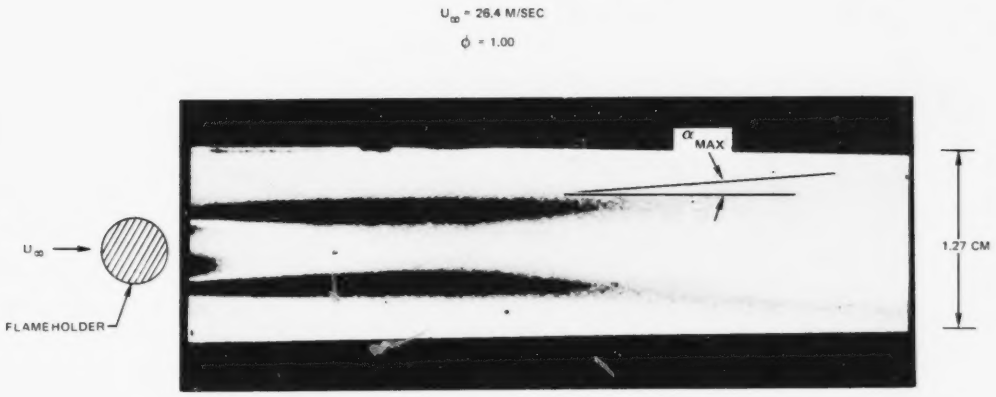

FIG. 9 TIME–EXPOSURE (1/500 SEC) SCHLIEREN PHOTOGRAPH OF A METHANE–AIR FLAME

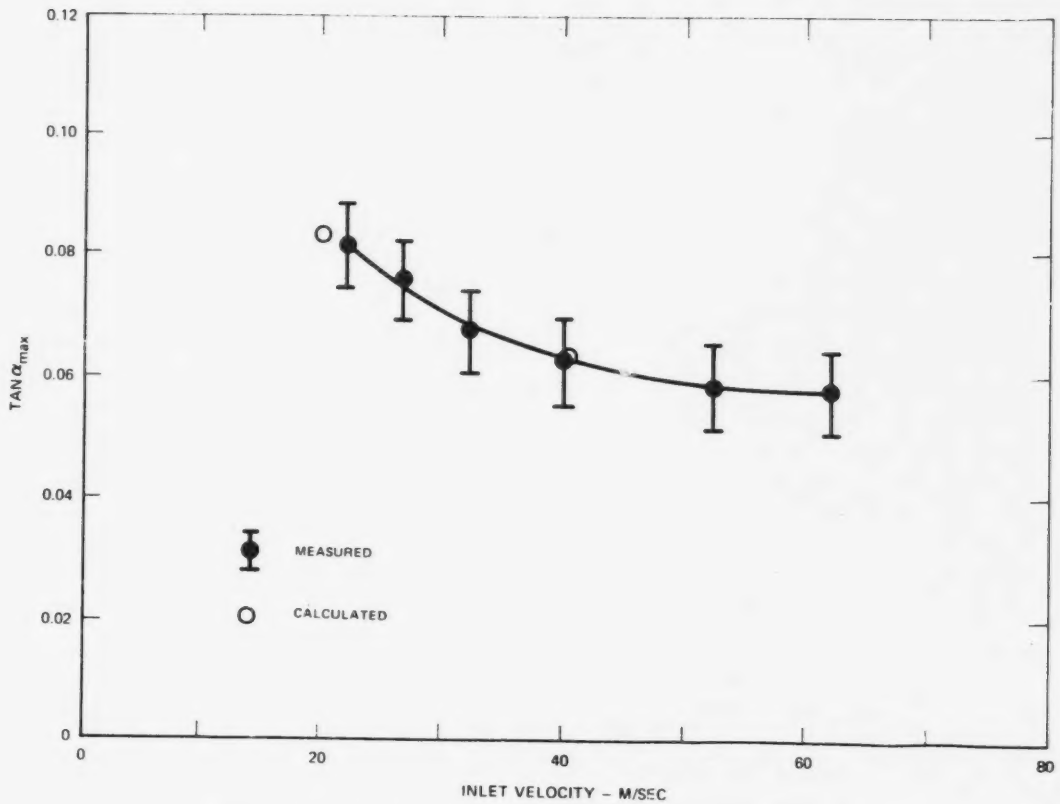

FIG. 10a **TYPICAL DEPENDENCE OF THE MAXIMUM FLAME ANGLE ON INLET VELOCITY FOR A STOICHIOMETRIC METHANE–AIR MIXTURE.**

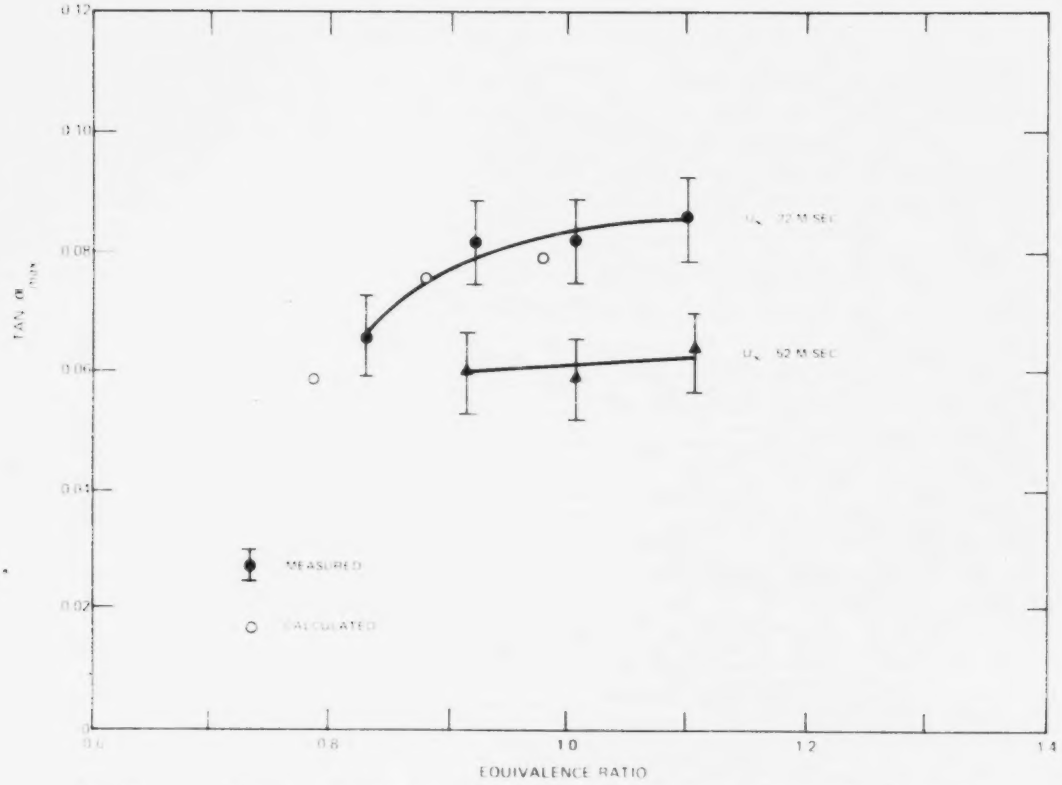

FIG. 10b TYPICAL DEPENDENCE OF THE MAXIMUM FLAME ANGLE ON EQUIVALENCE RATIO FOR METHANE–AIR MIXTURES.

III-C. TEMPERATURE MEASUREMENT EXPERIMENTAL RESULTS

The rate of formation of nitric oxide from atmospheric (molecular) nitrogen is strongly dependent on temperature. Hence, to characterize the nitric oxide formation process in the recirculation zone, the temperature distribution in the zone must be determined. Two different experimental approaches can be used to measure the temperature of the hot gas in the recirculation zone -- probe thermometry (eg. thermocouples) and optical techniques (eg. sodium-line reversal). Probe thermometry can provide a measure of the local time-mean temperature; however, probe techniques have the major disadvantage of disturbing the flow field. This disturbance can be particularly severe for the relatively small-scale recirculation zones in the present investigation. Optical techniques can be used to measure temperature without disturbing the flow field; however, these techniques can provide only an average-value of the temperature along the optical path. In the two-dimensional flows, used in the present investigation, flow properties are essentially constant across the flow (ie. in the direction parallel to the flameholder axis), so that the space-averaging of the optical techniques is not a serious drawback.

In the present experiments, a modified sodium-line reversal technique was used to measure the gas temperature in the recirculation zone. The basic principal underlying the sodium-line reversal technique is that of matching the spectral brightness of a light source to the spectral brightness of sodium emission from the flame (Ref.15). At the matching point, the translational temperature of the flame is equal to the brightness temperature of the light source (at the wavelength of the sodium emission). A detailed discussion of the experimental technique used in the present investigation and a schematic diagram of the optical system are given in Appendix A.

In the present experiments, two different techniques were used to inject sodium tracer into the recirculation zone. For most of the measurements, the solid, uncooled flameholder was used, and a small amount of crystalline sodium chloride was placed on the downstream side of the flameholder. During combustion, the salt crystals vaporized, and sodium entered the recirculation zone by convection. In a limited number of experiments, the injecting flameholder was used to inject a water/sodium chloride solution into the recirculation zone.

Temperature measurements were made at four locations in the recirculation

zone for conditions presented in the combustion test matrix, Table II. The four locations are illustrated in Fig. 6. At a distance of 0.5 cm downstream from the trailing edge of the flameholder, the temperature was measured at three different transverse positions -- positions 1 (centerline), 2 and 3. The temperature also was measured at a second axial position on the recirculation zone centerline, approximately 0.75 cm downstream from the flameholder -- position 4. The measured temperatures are, in fact, volume-averaged values, the volume, over which the average is taken, being determined by the image of the monochromator entrance slit in the test section. The approximate cross-section of this volume, shown in Fig. 6, is 0.01 cm x 0.20 cm.

Some typical experimental observations are illustrated in Figs. 11-13, and all of the temperature data are tabulated in Table IV. The data plotted in Fig. 11 suggest that, within experimental uncertainty, the temperature is uniform throughout most of the recirculation zone. The data in Fig. 12 show that the recirculation zone temperature is approximately 10-15% lower than the adiabatic combustion temperature for the freestream equivalence ratio. Heat losses to the flameholder and test section walls cannot account for the low recirculation zone temperatures. It appears that the low zone temperatures are due in part to unreacted fuel in the zone. In Fig. 13, the recirculation zone temperature increases with increasing inlet velocity, possibly reflecting an increase in transport rates due to movement of the turbulent transition point upstream with increasing velocity. In an investigation of temperature distributions in the recirculation zone of bluff-body-stabilized propane–air flames (Ref. 14), observations similar to those of Figs. 11 and 13 were reported. Limited experiments with the injecting flameholder have shown that tracer injection reduces the recirculation zone temperature by approximately 75°K. This decrease in temperature can be attributed to the heat capacity of the water/salt solution injected into the recirculation zone.

III-D. RESIDENCE TIME MEASUREMENT EXPERIMENTAL RESULTS

If the recirculation zone is considered to be a chemical reactor in which nitric oxide is produced, then the nitric oxide concentration in the zone, as well as the net nitric oxide production rate, will depend on the rate of mass exchange between the recirculation zone and the outer flow. Each gas element entering the recirculation zone will remain there for different periods of time. The net mass exchange rate may be calculated considering an ensemble of gas elements with a distribution of residence times.

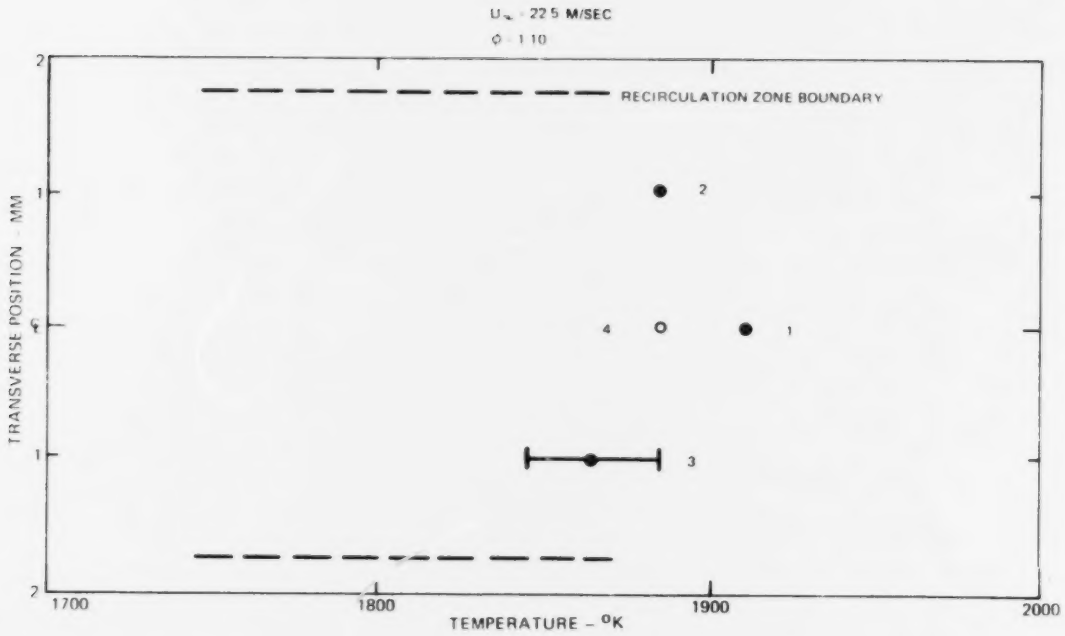

FIG. 11 **TYPICAL TEMPERATURE DISTRIBUTION IN THE RECIRCULATION ZONE.**

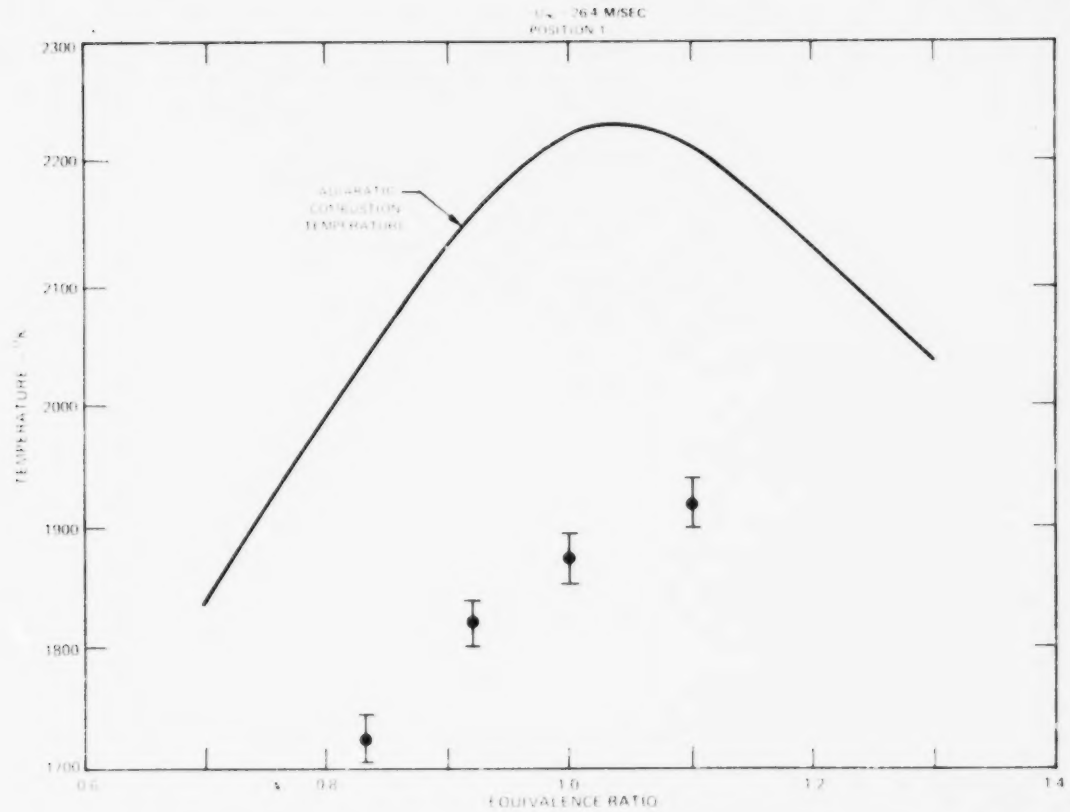

FIG. 12 TYPICAL DEPENDENCE OF RECIRCULATION ZONE TEMPERATURE ON EQUIVALENCE RATIO

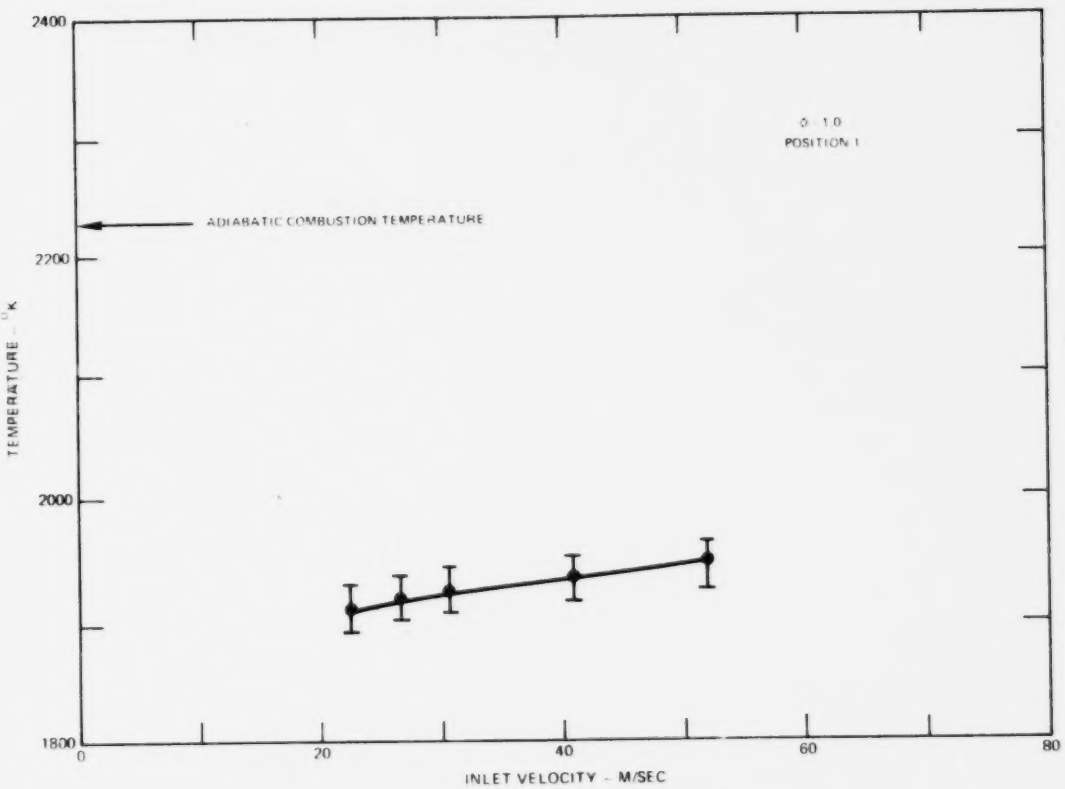

FIG. 13 **TYPICAL DEPENDENCE OF RECIRCULATION ZONE TEMPERATURE ON INLET VELOCITY.**

TABLE IV

RECIRCULATION ZONE TEMPERATURES

U_∞ (M/SEC)	ϕ	POSITION	T(^{o}K)
22.0	0.80	1	1690
21.8	0.91	1	1805
22.9	1.01	1	1870
23.2	1.00	1	1865
23.2	1.00	1	1855
22.5	1.10	1	1910
23.3	1.01	2	1850
22.5	1.10	2	1885
23.2	1.00	3	1845
22.6	1.10	3	1865
23.2	1.00	4	1880
22.5	1.10	4	1885
23.1	1.00	4	1810 *
22.7	1.09	4	1805 *
26.2	0.83	1	1725
26.6	0.92	1	1820
26.4	1.00	1	1875
26.6	1.11	1	1920
32.2	0.82	1	1735
32.1	0.90	1	1830
33.0	1.02	1	1890
30.8	1.12	1	1925
41.1	0.91	1	1835
40.4	1.00	1	1890
41.0	1.10	1	1935
40.8	0.90	4	1850
40.5	1.00	4	1900
40.7	1.11	4	1950
51.1	0.92	1	1840
53.3	1.00	1	1910
52.2	1.10	1	1940

100 MESH TURBULENCE SCREENS USED FOR ALL RUNS

* MEASURED WITH TRACER INJECTION

Alternatively, it is possible to define a mean residence time for the gas elements, which is related to the mass exchange rate by Eq. 7 . For reasons of simplicity, this latter approach was adopted in the present experiments. The mean residence time of gas particles in the recirculation zone can be determined by measuring the time decay of an injected tracer, following rapid shut-off of the tracer supply (Refs. 11 and 16). If the tracer is well-distributed throughout the recirculation zone and if the mass exchange rate/unit area is essentially constant over the boundary of the recirculation zone, then the tracer concentration decreases exponentially with time, with the time constant of the tracer decay identified as the mean residence time (cf., Appendix B).

The tracer material used in the present combustion experiments was sodium. In these experiments, a water/sodium chloride solution was injected into the recirculation zone through the rear of the flameholder. The injecting flameholder is discussed in detail in Appendix A.

The optical system used to make the residence time measurements was essentially the same as was used for the temperature measurements, (see Appendix A). However, in the residence time experiments, the photomultiplier output was displayed on an oscilloscope. The oscilloscope sweep was triggered on the termination of tracer flow. The experimental procedure followed in making the residence time measurements is outlined in Appendix A.

The residence time data obtained in the present investigation are tabulated in Table V and are plotted in Fig. 14. The experimental data show that the mean residence time is independent of the freestream equivalence ratio, the mesh size of the turbulence-generating screen and the location in the recirculation zone where the measurement was made. For inlet velocities greater than 25 m/sec, the mean residence time varies inversely with the inlet velocity U_∞, according to

$$\frac{\tau_r U_\infty}{D} = 90 \qquad (12)$$

where D = flameholder diameter. A similar correlation has been reported in two previous investigations of exchange processes behind bluff-body flameholders (Refs. 11 and 16). Results from these two investigations are plotted on Fig. 14. The data of Bovina (Ref. 16) for two-dimensional benzene-air flames stabilized on v-gutters are in approximate agreement

TABLE V
MEAN RESIDENCE TIMES

U_∞ (M/SEC)	ϕ	POSITION	τ_1 (MSEC)
21.8	0.80	1	16.0
21.8	0.91	1	14.5
22.2	1.01	1	14.2
22.1	1.11	1	15.5
21.6	1.01	1	14.5*
22.0	1.00	1	14.0**
22.2	0.99	1	14.1 +
26.1	0.81	1	11.5
26.0	0.91	1	11.0
26.4	1.00	1	12.1
26.1	1.12	1	11.0
31.1	0.92	1	10.0
30.9	1.00	1	9.5
32.0	1.09	1	8.9
40.2	0.91	1	7.2
41.0	1.02	1	7.0
40.1	1.08	1	7.0
41.0	0.99	1	6.9
41.1	1.00	1	7.1*
40.9	1.01	1	7.0**
44.8	0.99	1	6.5 +
22.0	0.90	4	15.1
22.2	1.00	4	13.7
22.1	1.09	4	16.4

MEASUREMENTS MADE WITH 100-MESH SCREEN EXCEPT AS INDICATED.

* 20-MESH SCREEN

** 60-MESH SCREEN

\+ 200-MESH SCREEN

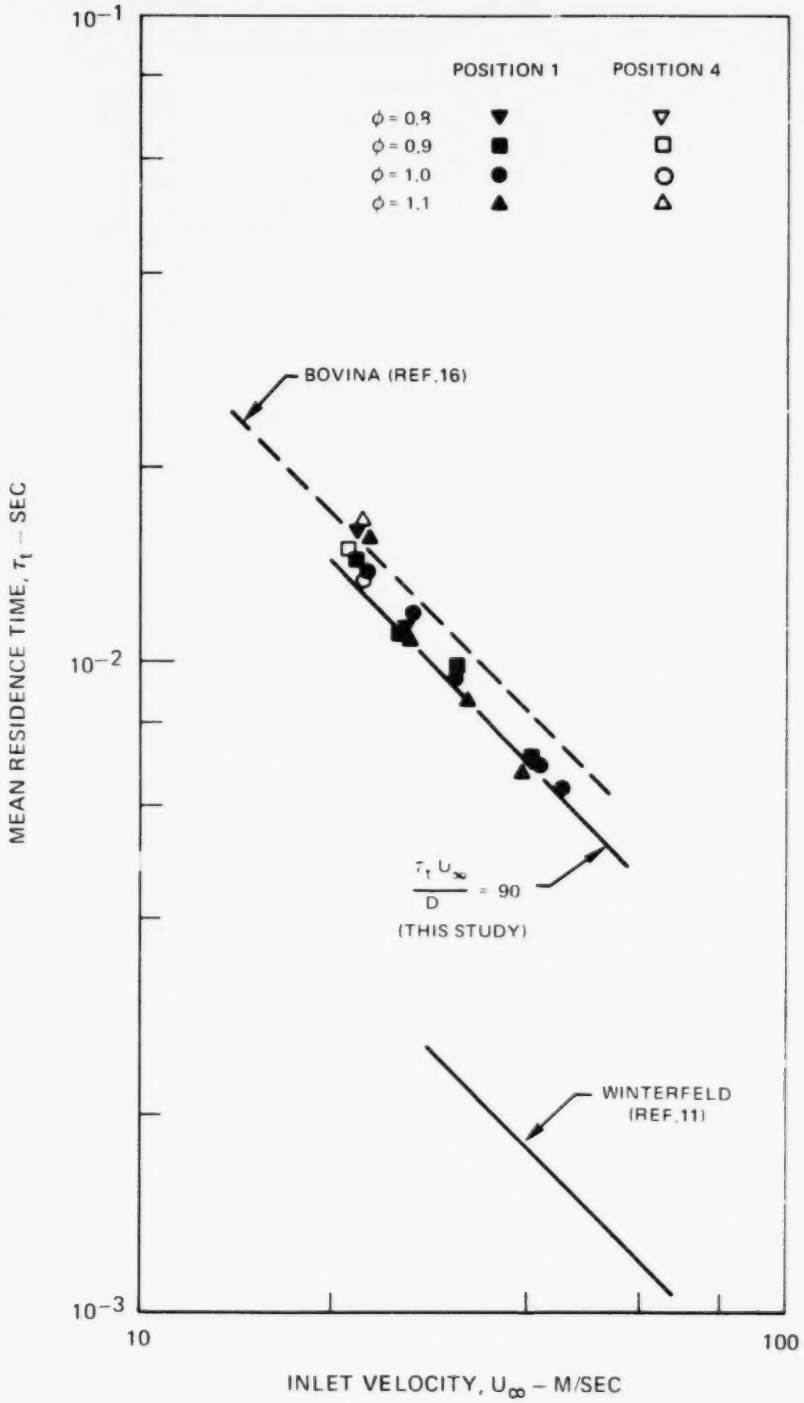

FIG. 14 **DEPENDENCE OF MEAN RESIDENCE TIME ON INLET VELOCITY, EQUIVALENCE RATIO AND MEASUREMENT LOCATION .**

with results from the present study. Winterfeld's data (Ref. 11) for propane-air flames stabilized on axisymmetric flameholders are significantly different from the data obtained in the two studies in two-dimensional flows. This deviation may reflect differences in the flow fields behind flameholders of differing geometry. For the lowest inlet velocity investigated, the measured residence times are somewhat longer than would be predicted by Eq. (12). These longer residence times may be due to the fact that the exchange process at the low inlet velocity is dominated by laminar transport while at higher velocities turbulent phenomena are more important.

The observation that the measured residence times are independent of measurement location tend to support the assumption of an exponential tracer decay. The observation that the measured residence times are independent of the mesh-size of the turbulence-generating screens indicates that the freestream turbulence produced by these screens does not affect the mass exchange rate between the recirculation zone and the outer flow. A likely explanation for this result is that the turbulence produced by the screens decays with downstream distance to the extent that, at the flameholder position, the screen-induced turbulence is small compared to the turbulence produced by the shear-layer downstream from the flameholder. The burner configuration was such that it was not possible to closely couple the turbulence-generating screens and the flameholder. Hence, independent variation of freestream turbulence could not be obtained in the combustion experiments.

III-E. CONCENTRATION MEASUREMENT EXPERIMENTAL RESULTS

Three different sets of concentration data were obtained in the combustion experiments. In the recirculation zone, the nitric oxide formation rate depends on the concentration of radical species, specifically O, OH and N, in the zone. To obtain an estimate of radical concentrations in the zone, the time-average OH concentration was measured at a single location in the zone using an ultraviolet absorption technique. The nitric oxide concentration at two locations in the recirculation zone also was measured using an ultraviolet absorption technique. The ultraviolet absorption technique and the experimental procedures used in making the concentration measurements in the recirculation zone are discussed in Appendix A. The overall nitric oxide production in the combustor test section was determined by measuring the nitric oxide concentration in the exhaust gas using a sampling probe coupled to a time-of-flight mass spectrometer. The sampling system and experimental techniques used for

the exhaust concentration measurements are discussed in Appendix A.

III-E.1 OH Concentration Measurements

The mean OH concentration in the optical path was determined at a single location in the recirculation zone (position 1) by measuring absorption of ultraviolet radiation by the $\Sigma\Pi(0,0)$ band of the molecule. The measured OH concentrations are tabulated in Table VI, and are plotted as a function of equivalence ratio and inlet velocity in Fig. 15. The measured OH concentration is weakly dependent on equivalence ratio, and attains a maximum value for stoichiometric mixtures. For the two velocities investigated, the measured OH concentration was essentially independent of inlet velocity. Three curves showing OH concentration for several different sets of assumptions and conditions also are plotted on Fig. 15. The OH-concentration curve labeled "equilibrium-nonadiabatic" was calculated for the freestream equivalence ratios assuming chemical equilibration at the measured recirculation zone temperature. The curve labeled "equilibrium-adiabatic" was calculated for the freestream equivalence ratios assuming chemical equilibration at the adiabatic combustion temperature. The curve labeled "equilibrium-stirred reactor" was calculated for a perfectly-stirred reactor assuming chemical equilibration at the measured recirculation zone temperature. This stirred-reactor calculation is discussed in more detail in Section V-A. Comparison of the three calculated equilibrium OH-concentration curves with the experimental data shows that the OH concentrations, measured in the recirculation zone, exceed OH concentrations corresponding to any possible equilibrium state. It follows from this observation that the OH concentrations (and the concentrations of other radical species such as O and N) in the recirculation zone are kinetically controlled and hence, an assumption of equilibrium hydrocarbon chemistry cannot be used to model the nitric oxide formation process in the recirculation zone.

III-E.2 Nitric Oxide Concentration Measurements - Recirculation Zone

The mean nitric oxide concentration in the optical path was determined at two locations in the recirculation zone (positions 1 and 4) by measuring the absorption of ultraviolet radiation by the $\gamma(0,0)$-band of the molecule (see Appendix A). A similar optical technique has been used to measure nitric oxide concentrations in several recent investigations of pollutant formation in combustion processes (Refs. 17-20).

The nitric oxide concentrations measured in the recirculation zone are tabulated in Table VII, and are plotted as a function of equivalence ratio

TABLE VI
OH CONCENTRATION

U_∞(M/SEC)	ϕ	C_{OH} (10^{-8} MOLE/CM^3)
21.6	0.81	2.0 $\pm$ 0.3
21.6	0.87	2.3
21.7	0.91	2.4
21.6	0.91	2.8
21.9	1.01	2.8
21.8	1.01	3.2
21.7	1.18	2.8
26.4	0.88	2.4
26.7	0.92	2.4
26.7	1.02	3.0

ALL MEASUREMENTS MADE AT POSITION 1 (FIG. 6), USING 100-MESH TURBULENCE GENERATING SCREEN

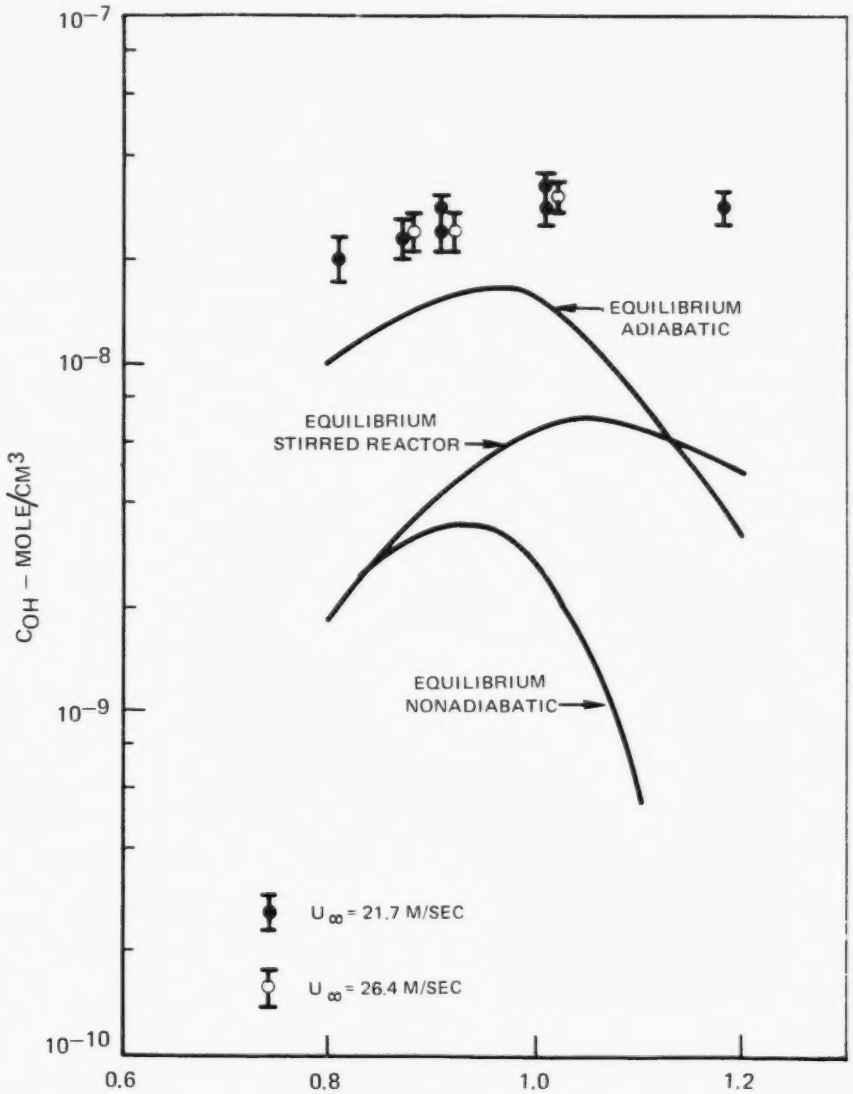

FIG. 15

HYDROXYL RADICAL CONCENTRATION IN THE RECIRCULATION ZONE AS A FUNCTION OF EQUIVALENCE RATIO AND INLET VELOCITY.

TABLE VII

NITRIC OXIDE CONCENTRATIONS IN RECIRCULATION ZONE

U_∞ (M/SEC)	ϕ	POSITION	NO MOLE FRACTION — PPM (V)		
			MEASURED*	CALC – EQ STIRRED REACTOR	CALC – NON-EQ STIRRED REACTOR
21.4	0.81	1	NOT MEASURABLE	0.05	4
21.2	0.90	1	40 ± 10	0.50	19
21.6	1.01	1	65 ± 5	1.7	42
21.4	1.01	1	75 ± 5	—	—
21.4	1.00	1	62 ± 5	—	—
22.0	1.10	1	105 ± 5	4.1	75
41.3	0.91	1	30 ± 15	0.36	14
41.1	1.00	1	44 ± 10	1.4	35
41.0	1.11	1	60 ± 5	2.6	47
58.8	1.12	1	40 ± 10	2.0	42
21.8	1.02	1	55 ± 5	—	—
21.6	1.00	1	56 ± 5	—	—
21.6	1.11	1	90 ± 5	—	—

* NO MOLE FRACTION CALCULATED FROM

$$\text{NO MOLE FRACTION } C_{NO} \frac{P(\text{MEASURED})}{RT(\text{MEASURED})}$$

and measurement location in Fig. 16a and as a function of inlet velocity in Fig. 16b. The vertical bars through the symbols indicate the uncertainty in the concentration measurement resulting from uncertainties in the calibration, in determination of the mean transmissivity (see Appendix A) in the combustion experiment and in the measured temperature used to calculate total nitric oxide concentration from the measured ground-state concentration. The experimental data in Fig. 16a indicate that the nitric oxide concentration is nearly constant throughout the recirculation zone. However, the nitric oxide concentrations measured at the downstream axial position appear somewhat lower than the concentrations measured at the upstream position. In an investigation of concentration distributions in the recirculation zone of bluff-body-stabilized propane-air flames (Ref. 14), CO_2, H_2O, and O_2 concentrations were found to be uniform throughout the zone. The nitric oxide concentration in the recirculation zone increases as the equivalence ratio increases from 0.8 to 1.1. The experimental data in Fig. 16b show that the nitric oxide concentration in the recirculation zone decreases as the inlet velocity increases from 20 to 60 m/sec. The solid lines in Figs. 16a and 16b are calculated nitric oxide concentrations obtained from various analytical models for the nitric oxide formation process in the recirculation zone. These models are discussed in detail in Section V-A.

III-E.3 Exhaust Concentration Measurements

The concentration distributions of nitric oxide, methane, oxygen, carbon dioxide and carbon monoxide in the exhaust gas from the combustion test section were determined using a traversing sampling probe coupled to an on-line time-of-flight mass spectrometer. A schematic diagram of the sampling system and associated data processing equipment is shown in Appendix A.

Typical species concentration profiles in the exhaust, measured at the exit plane of the combustor test section, are shown in Figs. 17a and 17b. Fig. 17a shows the concentration profiles of methane, oxygen and carbon dioxide. Fig. 17b shows the nitric oxide concentration profiles. These data show that there are substantial concentration variations in the exhaust and that there is a significant amount of unreacted fuel at the test section exit. An average exhaust nitric oxide concentration can be determined from the concentration profile in Fig. 17b. Some uncertainty is introduced in the determination of the average nitric oxide concentration by the lack of concentration data near the test section walls. Average exhaust nitric oxide concentrations are tabulated in Table VIII for a range of inlet velocities and equivalence ratios.

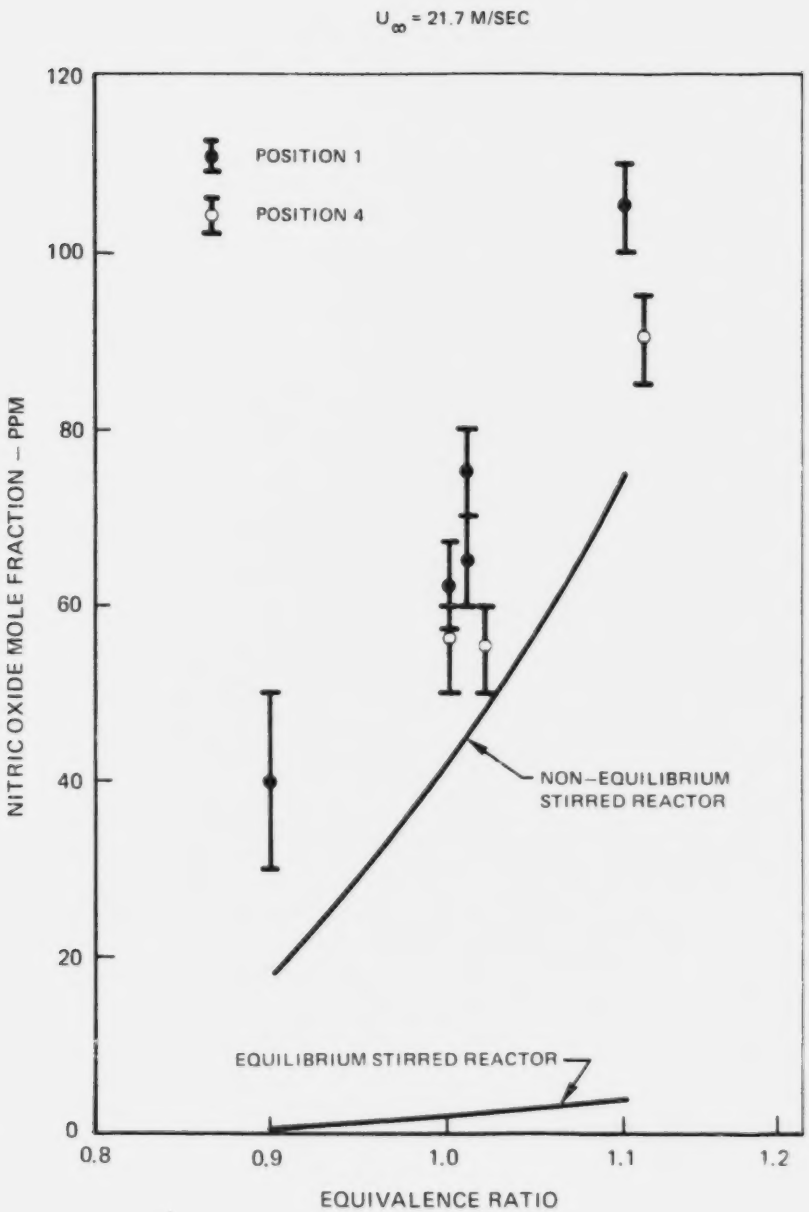

FIG. 16a **TYPICAL DEPENDENCE OF NITRIC OXIDE CONCENTRATION IN THE RECIRCULATION ZONE ON EQUIVALENCE RATIO AND MEASUREMENT LOCATION.**

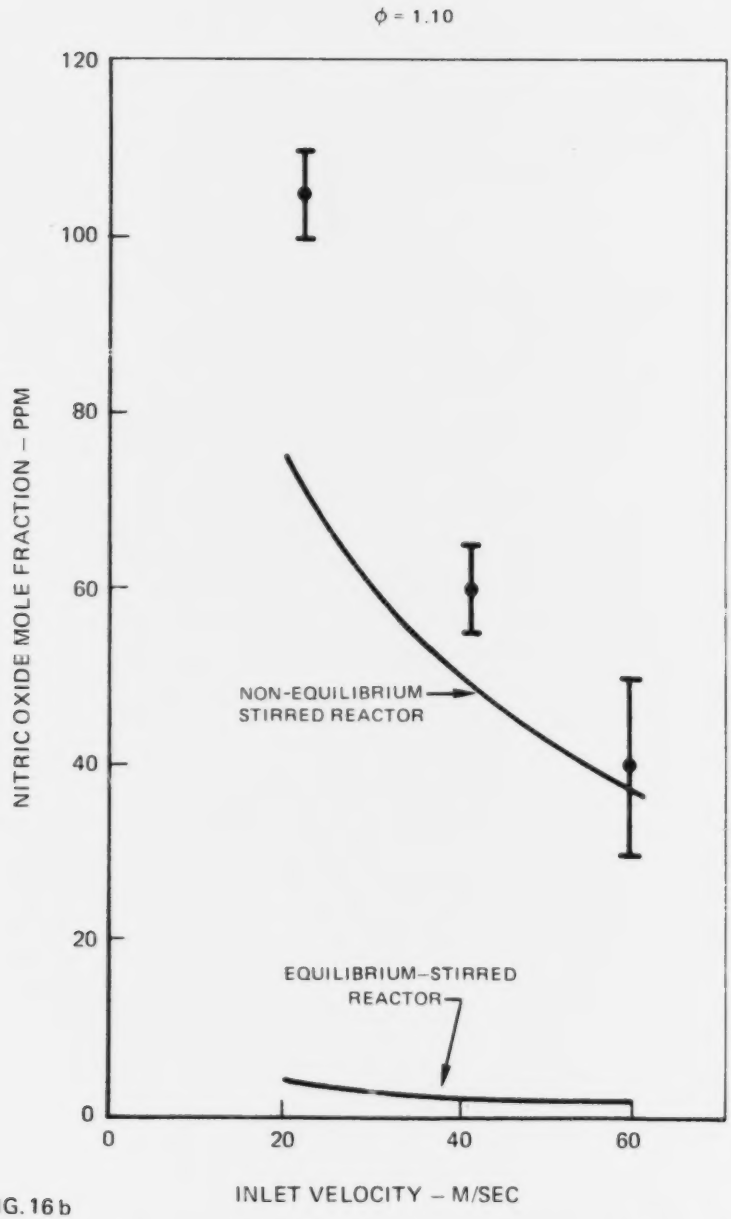

FIG. 16 b

TYPICAL DEPENDENCE OF NITRIC OXIDE CONCENTRATION IN THE RECIRCULATION ZONE ON INLET VELOCITY.

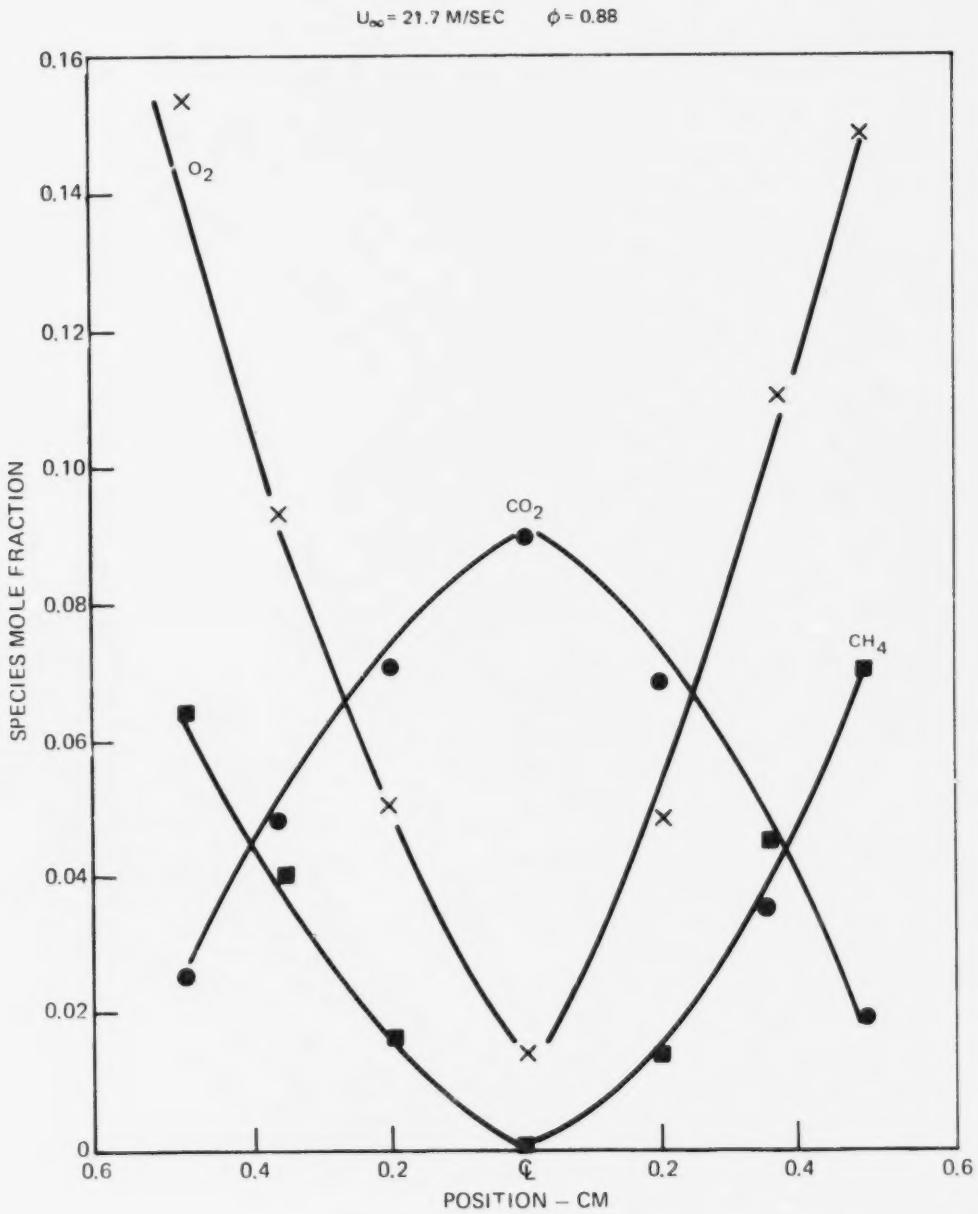

FIG. 17a

TYPICAL SPECIES CONCENTRATION PROFILES AT THE EXHAUST OF THE COMBUSTOR TEST SECTION.

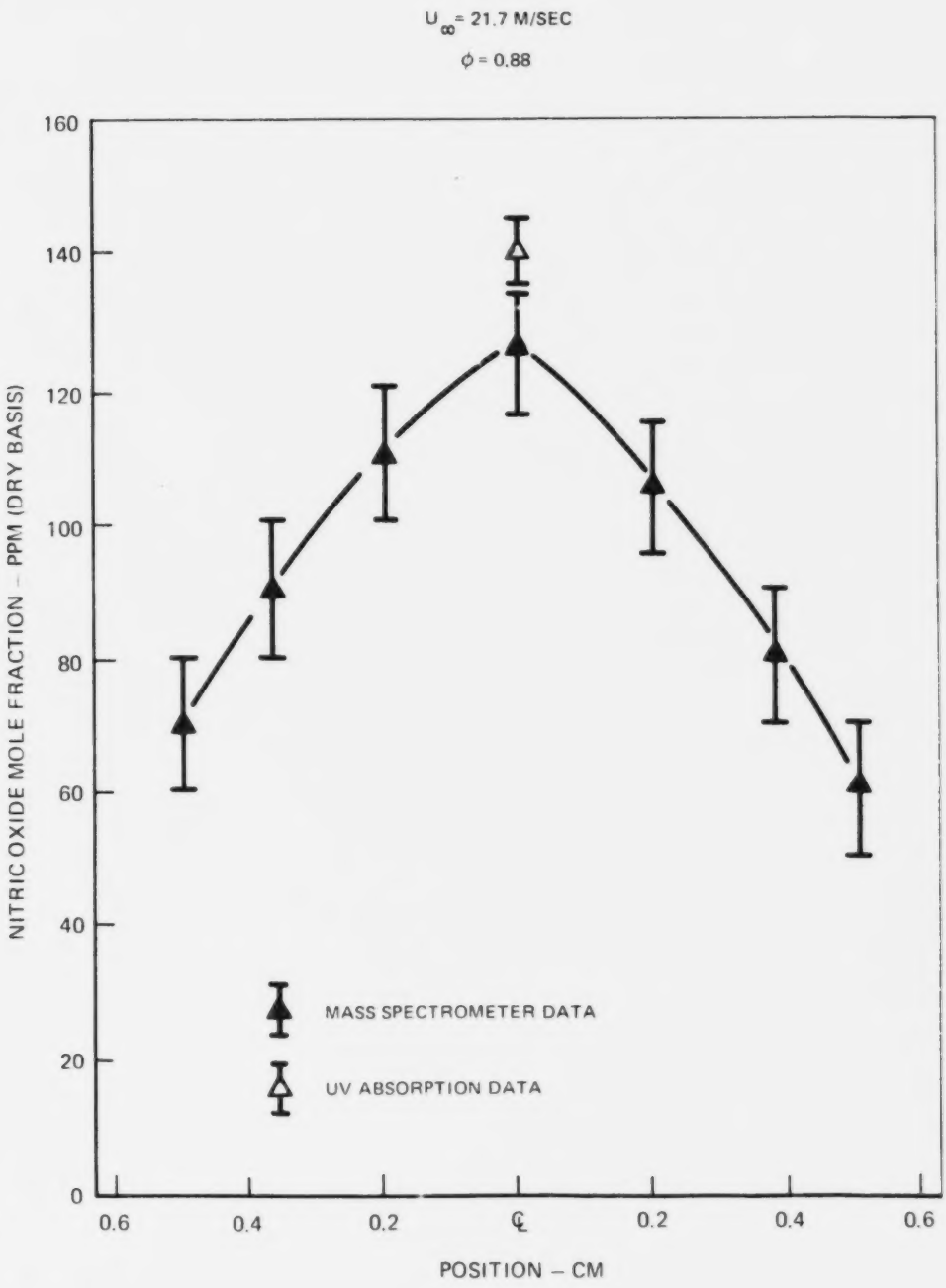

FIG. 17b **TYPICAL NITRIC OXIDE CONCENTRATION PROFILES AT THE EXHAUST OF THE COMBUSTOR TEST SECTION.**

TABLE VIII

NITRIC OXIDE CONCENTRATIONS IN EXHAUST GAS

U_∞ (m/sec)	ϕ	AV. NO MOLE FRACTION – PPM (DRY)
21.4	0.81	60 ± 15
21.2	0.88	90 ± 10
21.5	1.00	128 ± 10
21.6	1.10	49 ± 15
41.0	0.88	48 ± 15
41.1	1.01	62 ± 15

The experimental results, discussed above, can be used to assess the relative importance of nitric oxide production in the recirculation zone to overall nitric oxide production in the burner. The mean volumetric nitric oxide production rate in the recirculation zone is given by

$$(\dot{m}_{NO}/V)_w = \frac{\bar{C}_{NO_w} M_{NO}}{\tau_t}$$

where $(\dot{m}_{NO}/V)_w$ = mean volumetric nitric oxide production rate in the recirculation zone (gm/cm^3-sec), $\bar{C}_{NO}$ = mean nitric oxide concentration in the zone (mole/cm^3), M_{NO} = molecular weight of nitric oxide (gm/mole) and τ_t = mean residence time of the gas in the zone (sec). A mean volumetric nitric oxide production rate in the burner may be expressed

$$(\dot{m}_{NO}/V)_{tot} = y_{NO} \left(\frac{\dot{m}}{V}\right)_{tot} \left(\frac{M_{NO}}{\bar{M}}\right)$$

where y_{NO} = mean nitric mole fraction at the burner exhaust, M = mean molecular weight of the exhaust gas (gm/mole), $\dot{m}_{tot}$ = total volumetric nitric oxide production rates in the zone are compared with overall nitric oxide production rates in Table IX. For the present experimental configuration, nitric oxide production in the recirculation zone is not a major factor in overall nitric oxide formation. This situation is a direct result of the relatively low temperature associated with the recirculation zone downstream from the cylindrical flameholder.

TABLE IX

RATIO OF NITRIC OXIDE PRODUCTION IN THE RECIRCULATION ZONE TO TOTAL NITRIC OXIDE PRODUCTION

U_∞ (M/SEC)	ϕ	$\frac{(\dot{m}_{NO}/V)_W}{(\dot{m}_{NO}/V)_{TOTAL}}$
21.4	0.90	0.04
21.4	1.00	0.04
21.4	1.10	0.14
41.0	0.90	0.05
41.0	1.00	0.06

SECTION IV

COLD FLOW EXPERIMENTS

IV-A. TEST EQUIPMENT

IV-A.1. Test Facility

The investigation of the characteristics of the two-dimensional recirculation zone downstream of a cylindrical bluff-body was conducted at the UARL fluid dynamics test facility (Fig. 18). The facility consists of a nominal 10 x 10 cm cross-section test chamber in which a two-dimensional cylinder, 1.59 cm in diameter, is installed with its axis normal to the air flow. Variation of velocity in the range 20-75 m/sec is effected by throttling the vacuum exhauster system connected to the facility. Density levels from 1 atm (1.2 kg/m^3) to 1/3 atm (0.41 kg/m^3) are established by installing suitable throttling plates at the facility inlet to restrict air weight flow.

The cylindrical bluff-body is composed of an outer shell which contains 39 injector ports distributed in three rows at angles of 135, 180 and 225 deg measured from the leading edge, to facilitate injection of a suitable tracer gas. Each injector port is 0.132 cm in diameter. Internal to the (primary) cylindrical shell is a second concentric cylindrical shell containing matching injector ports. The internal cylindrical shell is closely machined to fit the internal diameter of the primary cylindrical shell. In the normal open position injector ports in both cylindrical shells are aligned, thereby allowing unimpeded tracer flow through the shell ports into the recirculation zone. Rotation of the inner cylinder 20 deg seals off all ports in the outer shell, thereby stopping all tracer flow. Closure is accomplished through the use of a high speed pneumatic cylinder which has been calibrated for a closure time of approximately 1 msec. The cylinder body is traversable as a unit in the transverse (z) direction to allow the acquisition of data at locations removed from the test section center-plane (Fig. 19).

An assembly for installation of screens is incorporated in the design of the test facility at a location 1.25 cm upstream of the cylinder centerline, as shown in Fig. 19. Screens with various mesh spacing to wire diameter ratios are employed to vary the level of initial free

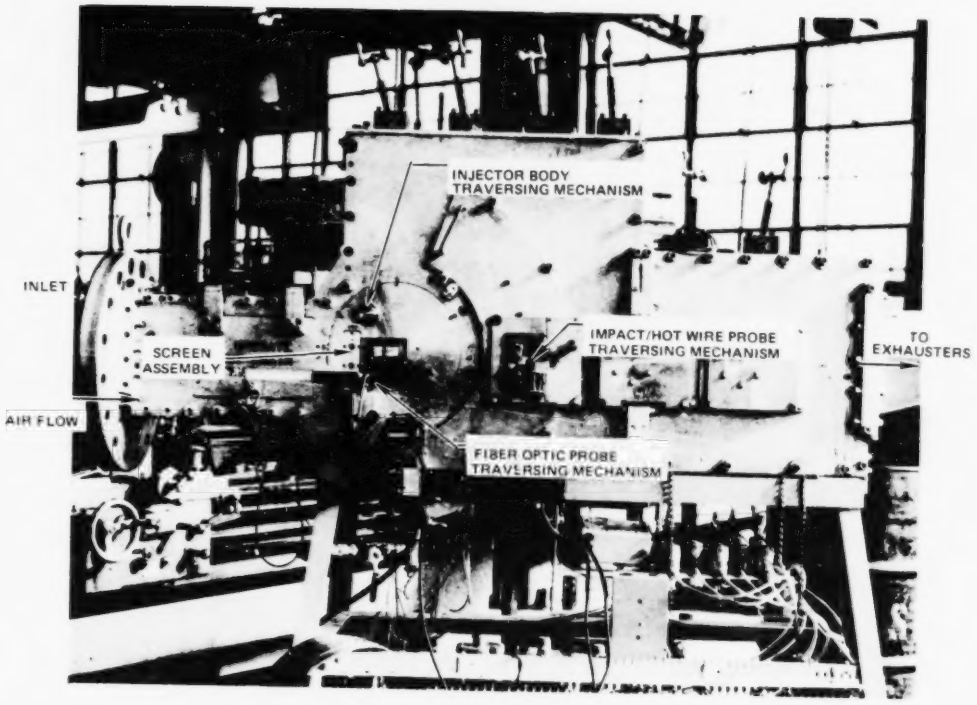

FIG. 18 COLD FLOW FLUID DYNAMICS TEST FACILITY

a) TOP VIEW

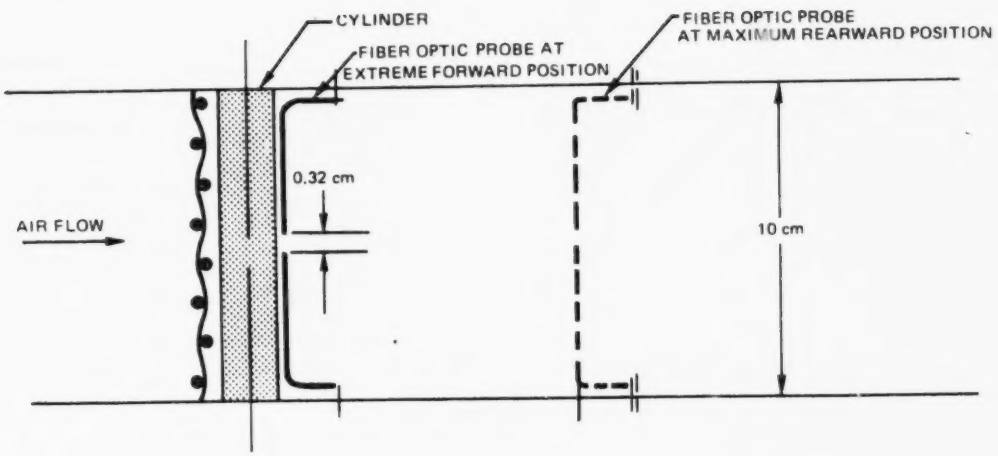

b) SIDE VIEW

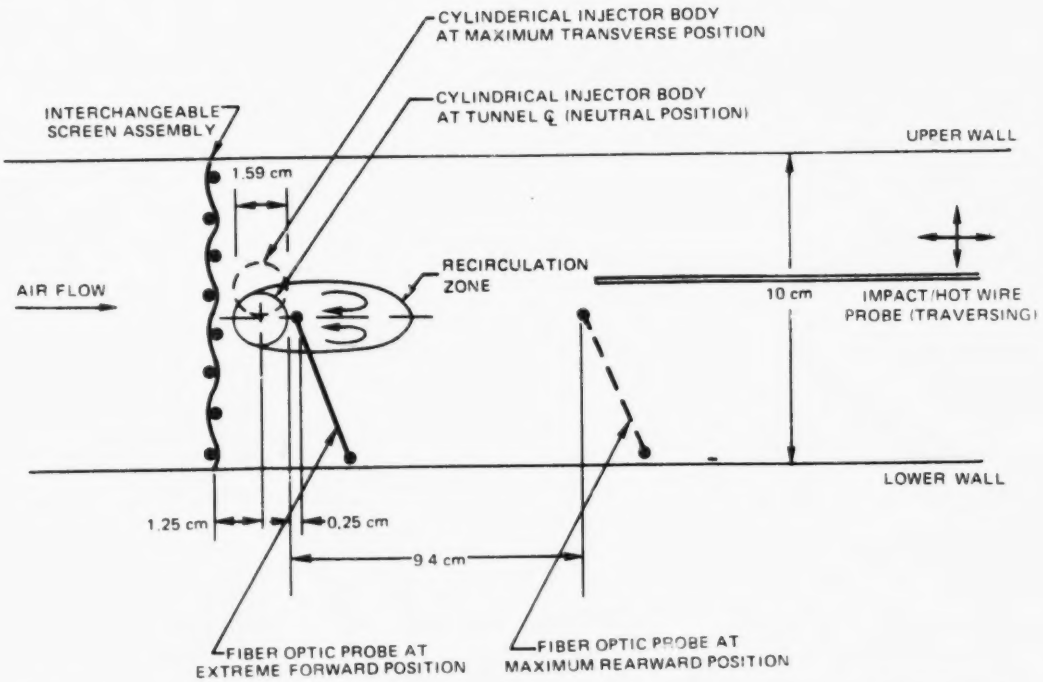

FIG. 19 SCHEMATIC DIAGRAM OF COLD FLOW FLUID DYNAMICS TEST SECTION

stream turbulence in the flow. The mesh spacings and wire diameters of the screens selected for use in this investigation, and the associated turbulent intensities measured at two locations downstream of each screen are given in Table X . Note that intensities vary from a high value of about 11 percent to a low of 3 percent at location "1". This location directly downstream of the screen is not significantly influenced by either the body or the confining walls and, therefore, measured turbulence levels can be characterized in terms of screen geometrical parameters. Measurements at a location near the end of the near-wake region will be discussed later.

Tracer concentration distributions and residence times are determined using fiber-optic probes (Fig. 20) which consist of a pair of sheathed bundles of glass fibers. One bundle of fibers serves as a transmitter and the other as a detector of visible light. The probe is integrated into a photometer system containing appropriate optics and electronic readout devices. Spacing between the probes is maintained at a value of 0.32 cm. The fiber optic probes are installed in a traversing mechanism actuated by a variable-speed electric motor to allow measurements to be taken throughout the near-wake region.

The tracer material used for the optical investigation consisted of an equilibrium mixture of NO_2 and N_2O_4 (see Appendix B). Initially, NH_4Cl particles were investigated as a possible tracer but the tendency of this material to coat the surfaces of the fiber optic probe eliminated it from further consideration.

IV-A.2. Facility Calibration and Operating Characteristics

Flow field uniformity in both the transverse (z) and axial (x) directions were ascertained from measurements of velocity profiles at several test chamber axial locations. Velocity profile information acquired at three approach velocities without screens for $\rho_\infty = 1.2$ kg/m^3 (Fig. 21) are typical of these data. Note that the outer, inviscid flow is quite uniform throughout the near-wake region. Velocity profiles taken with the turbulence-producing screens installed displayed a comparable degree of uniformity.

Turbulent intensities were determined using a constant temperature hot-wire anemometer (Fig.22). Hot-wire measurements were gathered at two locations: (1) x = 0.2 cm, z = 2.5 cm; and (2) x = 3.4 cm, z = 2.5 cm.

TABLE X
SCREENS FOR TURBULENCE PRODUCTION

SCREEN	S (CM)	b (CM)	S/b	U_∞ (M/SEC)	TURBULENT INTENSITIES (%)			
					POSITION "1"		"2"	
					u'/U_∞	v'/U_∞	u'/U_∞	v'/U_∞
1	1.27	0.203	6.25	19.5 57.5	9 11	11 10	12 9	11 10
2	1.27	0.160	7.93	19.5 57.5	– 7	– 6	11 –	12 –
3	1.27	0.124	10.2	19.5 57.5	5 –	6 –	10 –	11 –
4	1.27	0.104	12.2	19.5 57.5	5 3	6 4	10 –	11 –

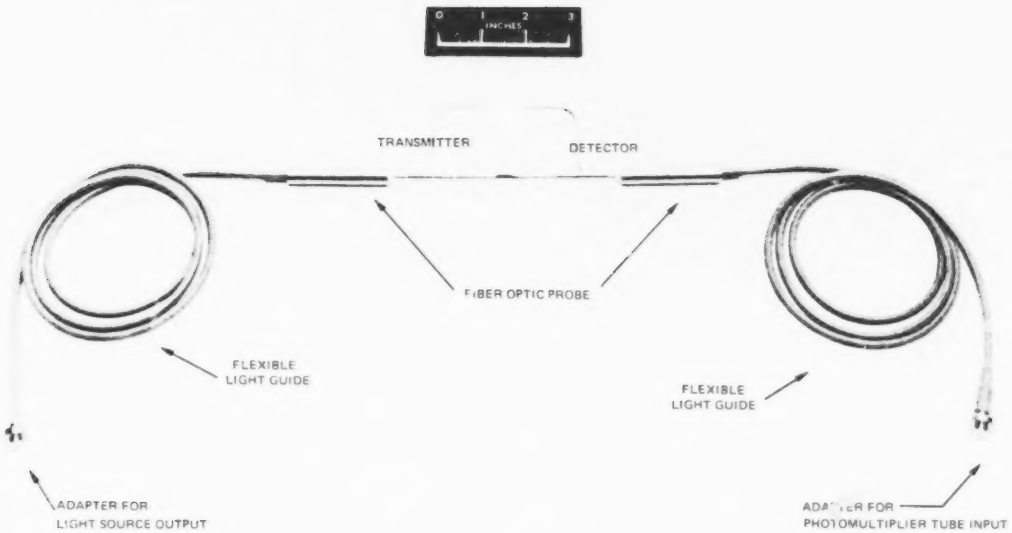

FIG. 20 **FIBER OPTIC PROBE**

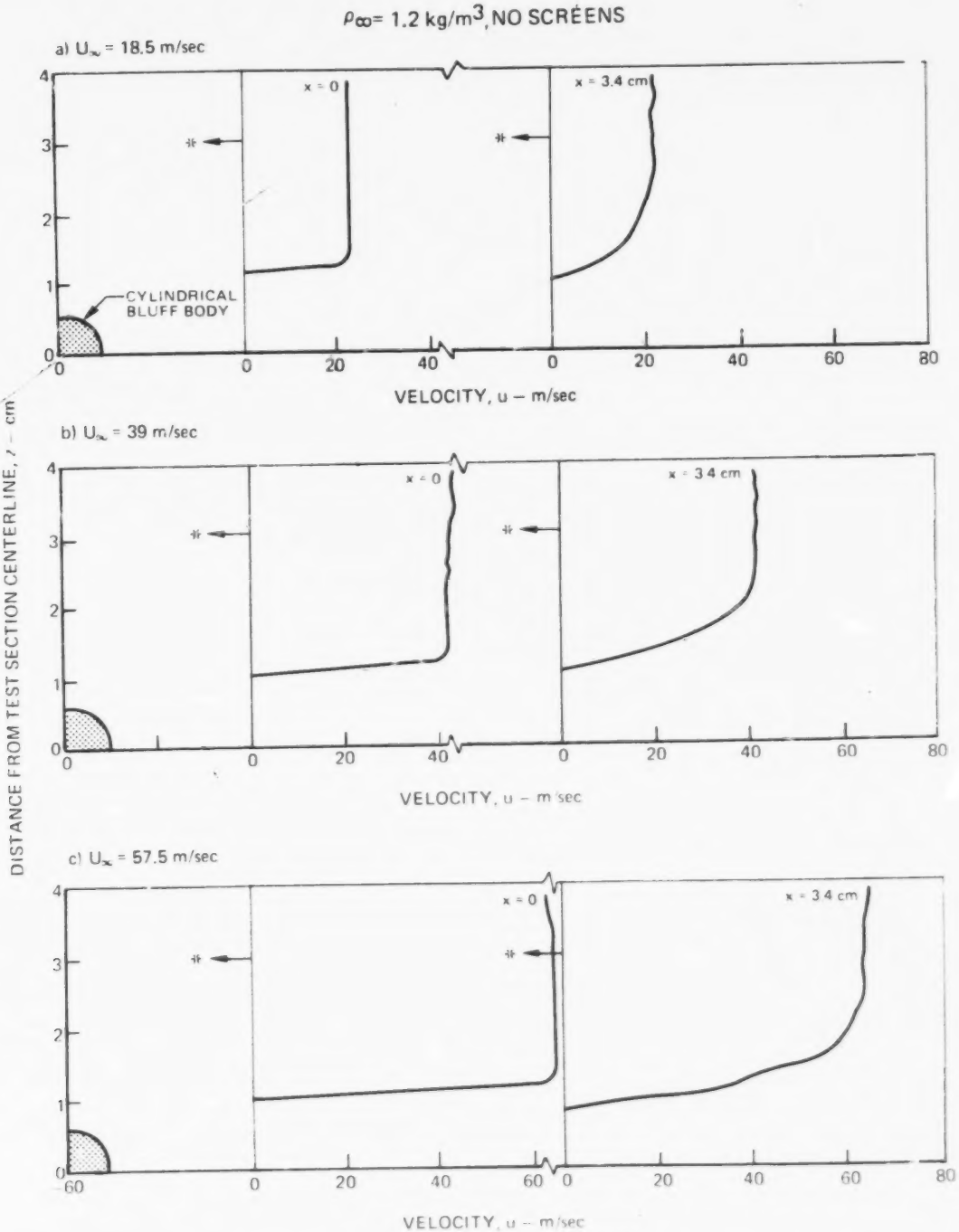
ρ_∞= 1.2 kg/m^3, NO SCREENS
a) U_∞ = 18.5 m/sec
x = 0
x = 3.4 cm
CYLINDRICAL BLUFF BODY
VELOCITY, u – m/sec
b) U_∞ = 39 m/sec
VELOCITY, u – m/sec
c) U_∞ = 57.5 m/sec
VELOCITY, u – m/sec
DISTANCE FROM TEST SECTION CENTERLINE, r – cm
* REGION WHERE PITOT PRESSURE IS LESS THAN STATIC PRESSURE

FIG. 21 TYPICAL VELOCITY PROFILES IN COLD FLOW TEST SECTION

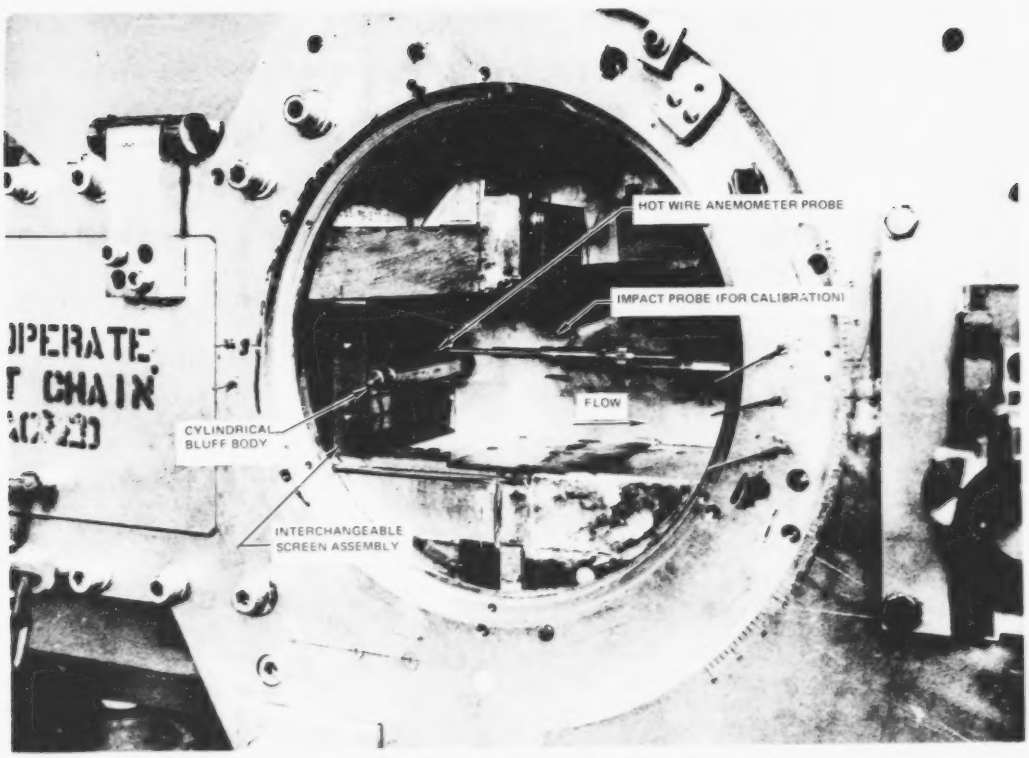

FIG. 22 COLD FLOW TEST SECTION WITH HOT WIRE PROBE INSTALLED

Tests were conducted at the two approach flow velocities 19.5 and 57.5 m/sec for each of four screens, which characteristics are given in Table X .

Mean wire voltages and velocity-component autocorrelations are recorded from tungsten wire sensors. The 0.0087 cm diameter, 0.25 cm long wires are mounted in an x-array for operation in a constant temperature mode using two DISA 55D01 constant temperature anemometers. It was assumed in the data reduction that the flow was incompressible with negligible temperature fluctuations.

Turbulence measurements at the two test locations were influenced to varying degrees by the vortex shedding phenomenon. Data obtained at position "1" are in good agreement with measurements reported in Ref. 21, as indicated in Fig. 23. Since the Ref. 21 data were obtained in the absence of outside influences, it may be concluded that the position "1" data are not affected significantly by the presence of the cylindrical bluff-body. At location "2", the time variant nature of the flow is clearly dominated by the periodic vortex shedding. The turbulence intensity at position "2" is found to be at the high levels of 9-12 percent independent of which screen is installed. Furthermore, the measured frequencies of the fluctuations at position "2" are in agreement with those computed from the expected Strouhal number (Ref. 5), using the body diameter and the velocity at the bluff-body location, ie., free stream velocity adjusted by the blockage ratio.

IV-A.3. Instrumentation

IV-A.3i. Fiber Optic System - Quantitative data acquisition in the cold flow investigation was accomplished using a fiber optic probe system (Appendix B) consisting of: (1) a fiber optic probe, (2) an optical photometer system, and (3) data acquisition and display electronics. The two identical units comprising the fiber optic probe, (Fig. 20) designated the transmitter and the detector unit, contain approximately 50 drawn glass fibers in a 0.25 cm diameter bundle encased within a stainless steel sheath. The probe transmits visible light above a wavelength of approximately 4000 Å.

IV-A.3ii. Flow Visualization - Flow field characteristics were observed using the laboratory schlieren system. In this effort, helium was utilized as the tracer medium to establish large density gradients. Recirculation zone geometrical parameters were determined from spark schlieren photographs. In addition, high speed (3,000 - 5,000 frames

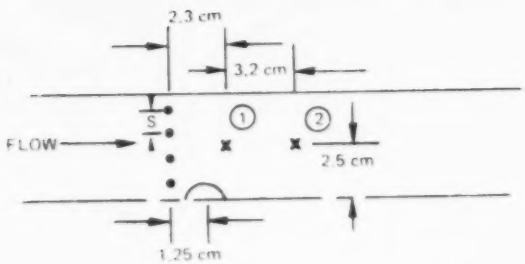

SYMBOL	S, cm	b, cm
△	1.25	0.203
□	1.25	0.160
◇	1.25	0.125
▷	1.25	0.104

U_∞ = 19.5 m/sec – OPEN

U_∞ = 57.5 m/sec – CLOSED

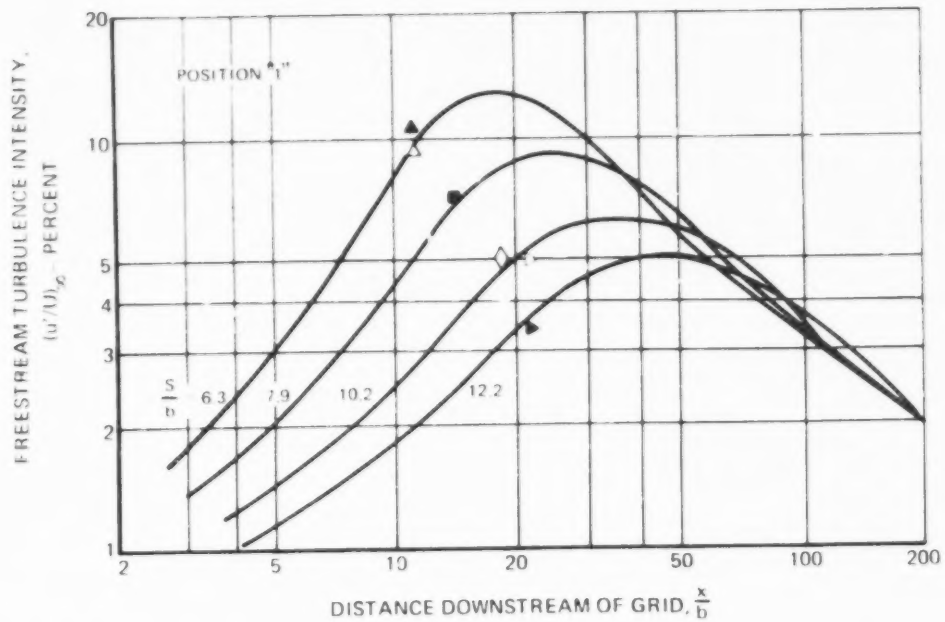

FIG. 23 TURBULENCE LEVEL DOWNSTREAM OF SCREENS.

per second) strobographic movies were taken at selected test conditions to facilitate study of the vortex shedding phenomenon.

IV-B. DISCUSSION OF RESULTS

The test matrix for the cold flow experiments, summarizing measurements made at each combination of free stream velocity, free stream density and screen, is contained in Table XI. Four types of test measurements were made including free stream pitot pressure distributions, recirculation zone geometrical parameters, and tracer concentration distributions and residence times in the recirculation zone. The matrix was evolved to insure that sufficient measurements were made to clearly define the variations of these major dependent variables.

Figure 24 is typical of the spark schlieren photographs obtained in the near-wake region using a helium tracer gas. The photograph indicates two clearly defined regions. Immediately downstream of the body, extending for a length of approximately two and one-half bluff-body diameters, is a region which encompasses the recirculation zone. The intersection of this region with the center plane of the flow can for all practical purposes be taken as the rear stagnation (closure) point, "r". A vortex which is being shed from the near-wake region also is distinguishable in the photograph of Fig. 24. The vortex shedding process results in significant local agitation of the flow and a marked distortion of that half of the recirculation zone from which the vortex issues. These vortex shedding effects are more discernable in the sequence of photographs shown in Fig. 25. No such vortex shedding effects were observed in the combustion experiments which were extracted from a high-speed schlieren motion picture of the flow. The recirculation zone length measured from the trailing edge of the cylinder to the closure point, and the maximum zone width, determined by doubling the maximum half-width of the undisturbed portion of the recirculation zone, are given in Fig. 26. The independent variable in this figure is the velocity at the bluff-body location computed from the approach velocity and the blockage ratio. As can be seen, within the scatter of the photographic data, no important changes in recirculation zone geometry occur for the conditions of the present study.

The increase in photometer system light transmission with time following the cessation of tracer material injection is shown for a typical case in the Fig. 27a oscilloscope trace. Information extracted from such photographs is used to determine relative tracer concentration varia-

TABLE XI

COLD FLOW TEST MATRIX

SCREEN (SEE TABLE VIII)	ρ_∞	1.7 kg/m^3			0.67 kg/m^3			0.41 kg/m^3		
	U_∞	24.0 m/sec	38.0 m/sec	72.0 m/sec	24.0 m/sec	38.0 m/sec	72.0 m/sec	24.0 m/sec	38.0 m/sec	72.0 m/sec
	Re	2.45×10^3	3.76×10^3	7.03×10^3	1.36×10^4	2.66×10^4	1.46×10^4	0.81×10^4	1.63×10^4	2.42×10^4
NONE		TCER	TCER	TCER	ER	CER	ER		CER	ER
1		TCER	TCER	TCER	R	CR	R	R	CR	R
2		TCER	TCER	TCER		CR			CR	
3		TCER	TCER	TCER	R	CR	R	R	CR	R
4		TCER	TCER	TCER		CR			CR	

T - PITOT PROBE TRAVERSES

C - FLOW VISUALIZATION

C - CONCENTRATION DISTRIBUTION

R - RESIDENCE TIME

U_∞ = 24 m/sec, NO SCREENS

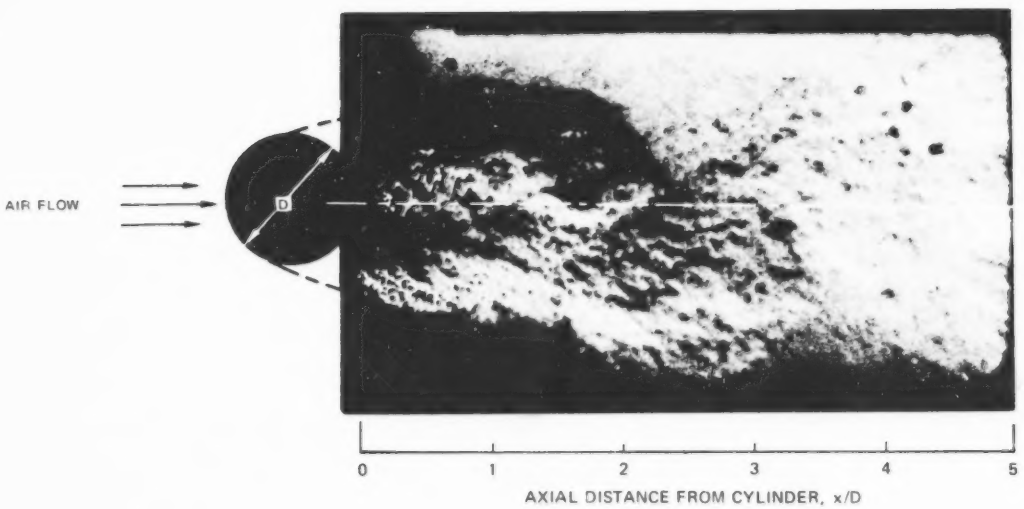

FIG. 24 SCHLIEREN PHOTOGRAPH OF NEAR–WAKE REGION

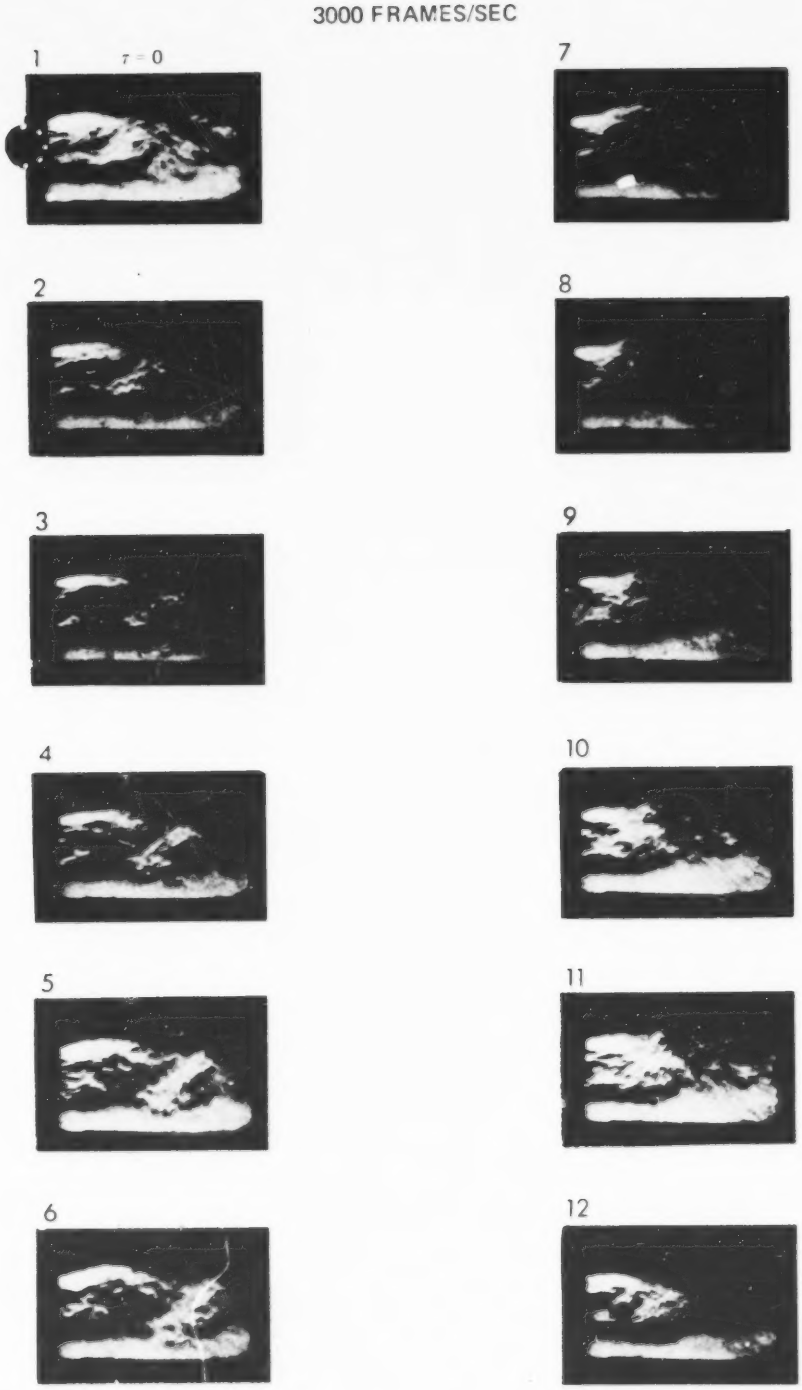

FIG. 25 VORTEX SHEDDING SEQUENCE.

$\rho_\infty = 1.2\ kg/m^3$

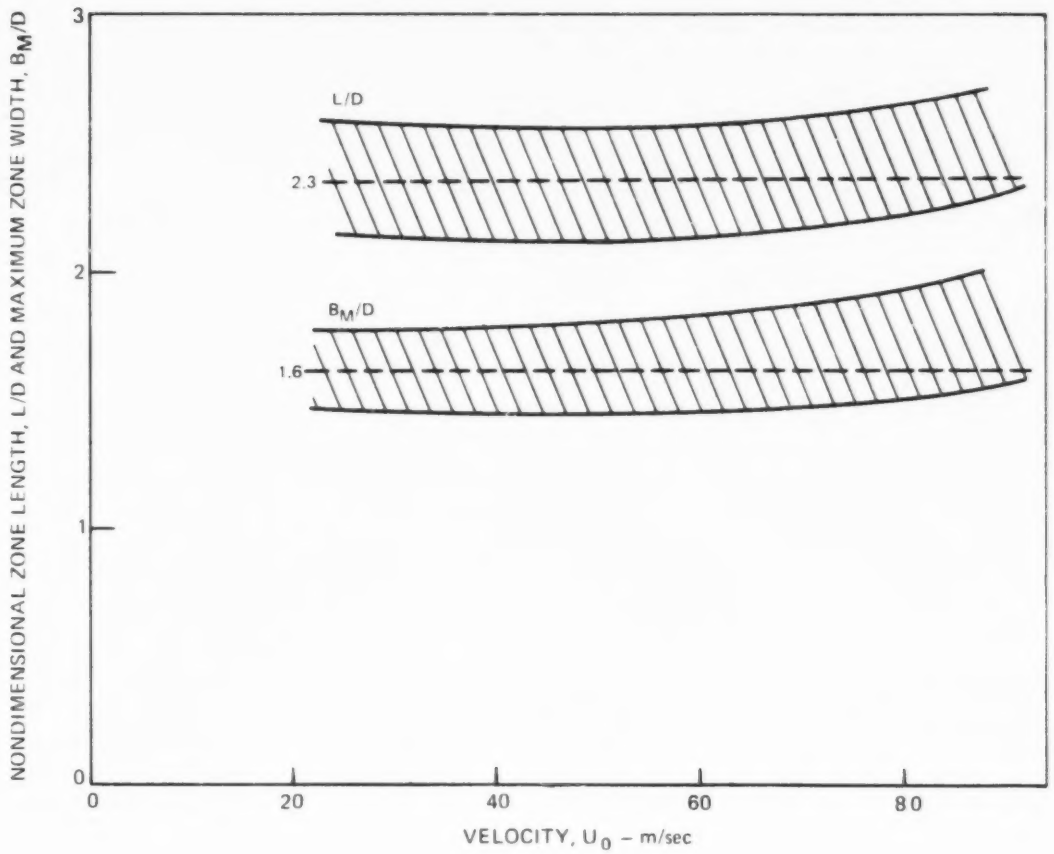

FIG. 26 RECIRCULATION ZONE GEOMETRICAL CHARACTERISTICS

tions with time by applying the Beer-Lambert Law (Ref. 22), as given in Appendix B, ie.,

$$y_t/\hat{y}_t = (\ln I/I_o)/(\ln \hat{I}/I_o) \tag{13}$$

where the tented parameters are reference quantities. In agreement with the results from Refs. 11 and 16, the relative tracer concentration is found to decrease in an exponential fashion with time until most of the tracer material has been transported out of the recirculation zone (Fig. 27b). The time required to reduce the tracer concentration to 1/e of its original concentration (the e-fold point) is taken as the tracer residence time, τ_t.

All residence time data acquired during the test program is provided in Table XII. Also shown is a residence time parameter, $(\tau_t U_o/D)\tau_v^{0.5}$, which according to the analytical development of Section II, should provide a correlation of the data. Note that the residence time correlation parameter varies within very narrow limits. This high degree of correlation is indicated more clearly in the Fig.28 presentation of typical results. No effect of free stream density is apparent indicating that the correct representation of $\hat{\rho}$ involves a direct dependence on $\sqrt{U_\infty}$. Furthermore, no trend is found with free stream turbulence level as augmented by screens placed immediately upstream of the bluff-body. In fact, a value of the correlating parameter of 2.4 ± 0.3 is appropriate for more than 90 percent of the data gathered, independent of the conditions of the free stream. This successful residence time correlation supports the view that body-related turbulent transport is the dominant mechanism for the near-wake region in the sub-critical Reynolds number regime.

It should be remarked that this finding is somewhat at variance with the work of Bovina (Ref. 16). In the cited work, $\tau_t U_o/D$ was found to be constant and independent of shedding period, in both cold and reacting flow experiments with two-dimensional V-shaped flameholders; these flameholders were 2 to 6 cm in size, with a 30 deg apex angle. Evidently, in these experiments, the transport mechanism was independent of whether or not a flame was stabilized on the bluff-body, suggesting that body-related turbulence for V-gutters (assuming vortex shedding occurs in cold flow) at Reynolds numbers of approximately 10^4, is not significant by comparison with turbulence produced from

U_∞ = 72 m/sec, ρ_∞ = 1.2 kg/m^3, SCREEN 2

a) OSCILLOSCOPE TRACE

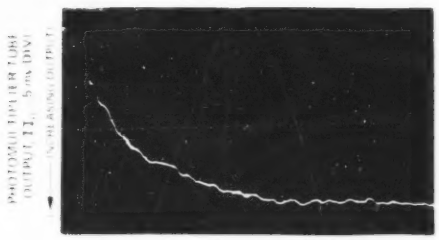

b) SEMI-LOG PLOT OF DATA

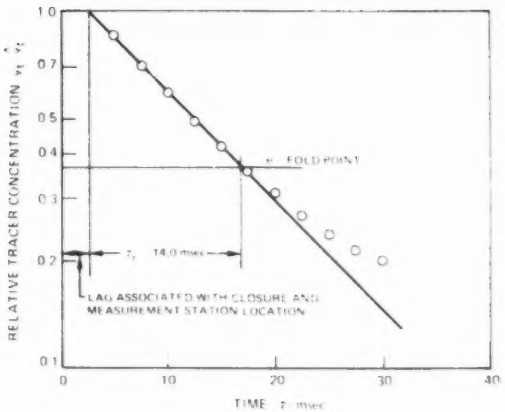

FIG. 27 RESIDENCE TIME DETERMINATION

TABLE XII

RESIDENCE TIMES AND CORRELATION PARAMETER

SCREEN (SEE TABLE VIII)	ρ_f KG/M^3	1.2			0.67			0.41		
	U_f M/SEC	24.0	48.0	72.0	24.0	48.0	72.0	24.0	48.0	72.0
	R_e	2.45×10^4	4.76×10^4	7.03×10^4	1.36×10^4	2.66×10^4	3.86×10^4	0.81×10^4	1.63×10^4	2.42×10^4
NONE	τ_1 MSEC	24	17	16	22	16	14	26	16	15
	$\left(\frac{\tau_1 U_f}{D}\right)\tau_1^{0.5}$ SEC$^{0.5}$	23	24	27	22	22	24	25	22	26
1	τ_2	23	18	15	26	15	14	26	15	13
	$\left(\frac{\tau_2 U_f}{D}\right)\tau_2^{0.5}$	23	25	25	25	20	24	25	20	21
	τ_2	25	17	14		15			15	
	$\left(\frac{\tau_2 U_f}{D}\right)\tau_2^{0.5}$	24	24	24		20			21	
2	τ_2	26	17	15	21	15	13	24	14	12
	$\left(\frac{\tau_2 U_f}{D}\right)\tau_2^{0.5}$	27	24	26	21	20	22	22	19	20
4	τ_2	29	18	16		17				
	$\left(\frac{\tau_2 U_f}{D}\right)\tau_2^{0.5}$	28	25	27		24				

NOTE: (1) $\rho_f U_f^2 \cdot g_c^{-1}$

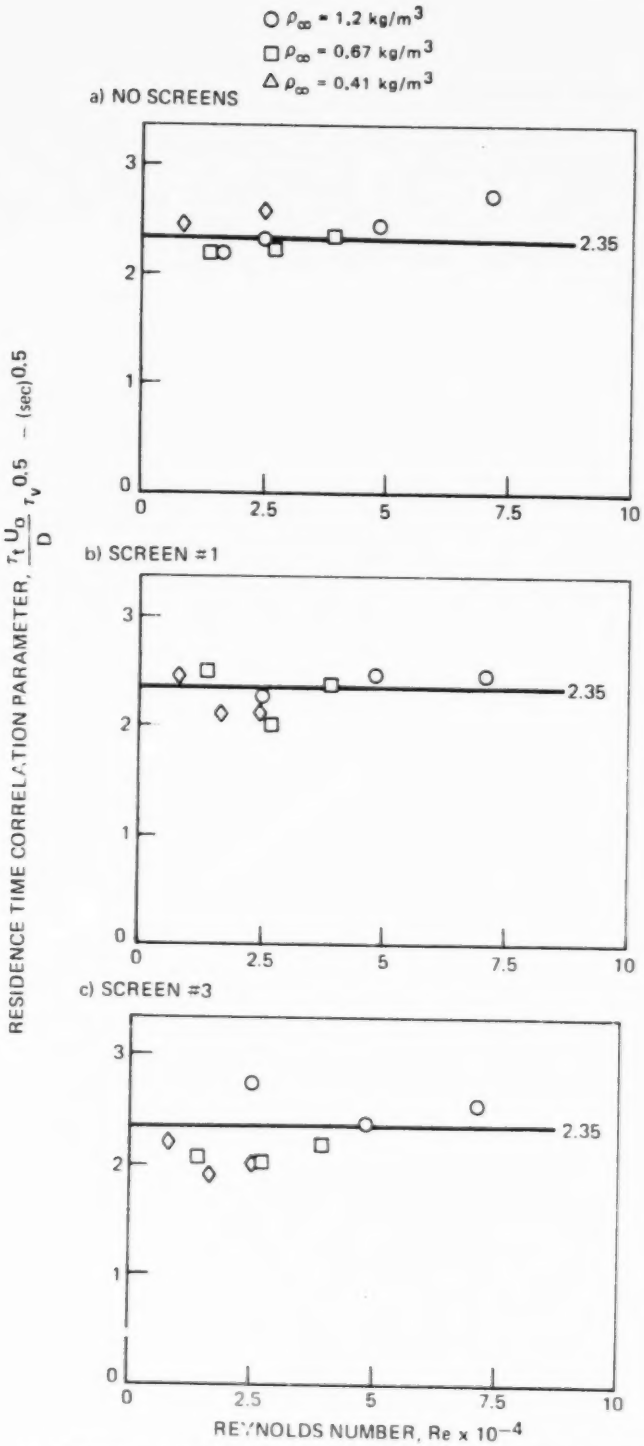

FIG. 28 RESIDENCE TIME CORRELATING PARAMETER FOR COLD FLOW

the interaction between the outer flow and the wake.

Tracer concentration distributions in the two-dimensional recirculation zone were obtained by taking axial traverses with the fiber optic probe at each of five transverse positions of the bluff-body. At each transverse bluff-body position, axial traverses were made both with and without tracer injection, see Fig. 29. Thus, at any given axial position, the output signal with tracer injection, I, can be normalized with the output signal obtained with no tracer, I_o.

Since the absolute magnitude of the tracer concentration in the recirculation zone is not particularly meaningful, it is convenient to provide a normalization with a reference concentration, $\hat{y}_t$. For the purposes of the present effort, the reference concentration was taken to be that concentration found at the test section center plane ($z = 0$), 1.2 cm downstream of the trailing edge of the bluff-body. This location was selected since the recirculation zone and the outer flow were found to be at the same temperature (to within 1°K - the expected experimental accuracy) downstream of this location, see Fig. 30.

All axial tracer concentration distributions measured displayed the features indicated in Fig. 31. Initially, there is a gradual reduction in concentration to a point approximately one diameter in length downstream of the bluff-body.

Thereafter, the concentration decreases rapidly with distance according to

$$y_t / \hat{y}_t \sim x^{\theta} \qquad (x \leq x_L) \tag{14}$$

where θ, the decay exponent, is found to vary between -1.0 and -1.5 but with most data indicating a value of approximately -1.3 (Fig.). An obvious change in the decay rate occurs at distances from the bluff-body of 2 to 3 diameters (Fig. 32) which correspond approximately to the longitudinal extent of the recirculation zone. Tracer concentration data in terms of the decay slope, θ, and the location at which the slope abruptly changes, $x_{L/D}$, are given in Table XIII.

The distribution of tracer material throughout the recirculation zone is displayed in the contour map of Fig. 33. It is significant that the transverse distributions of tracer material are quite flat. Evidently,

U_∞= 72 m/sec, ρ_∞= 1.2 kg/m^3, SCREEN #4

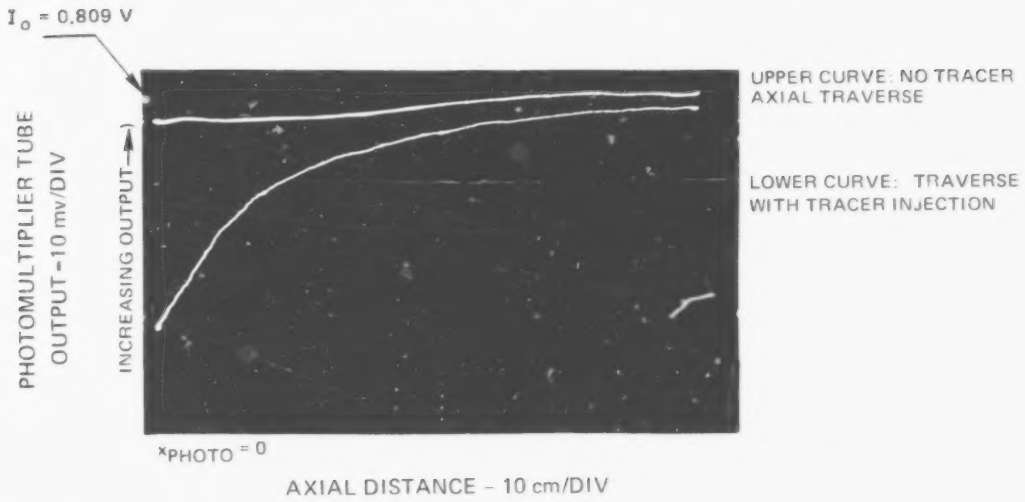
I_o = 0.809 V
PHOTOMULTIPLIER TUBE OUTPUT–10 mv/DIV
INCREASING OUTPUT
UPPER CURVE: NO TRACER AXIAL TRAVERSE
LOWER CURVE: TRAVERSE WITH TRACER INJECTION
x_{PHOTO} = 0
AXIAL DISTANCE – 10 cm/DIV

FIG. 29

OSCILLOSCOPE TRACE OF TYPICAL TRACER CONCENTRATION DISTRIBUTION

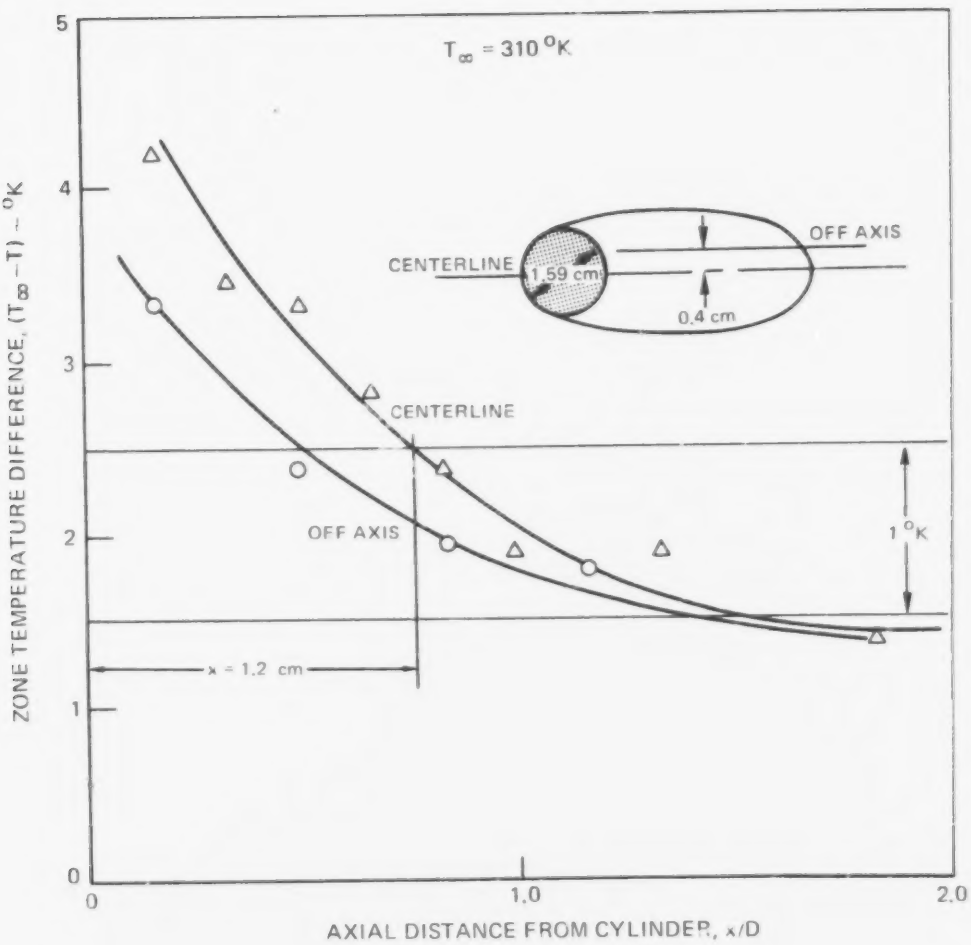

FIG. 30

AXIAL VARIATION OF TEMPERATURE IN RECIRCULATION ZONE

U_∞= 72 m/sec, ρ_∞= 1.2 kg/m^3, SCREEN #4

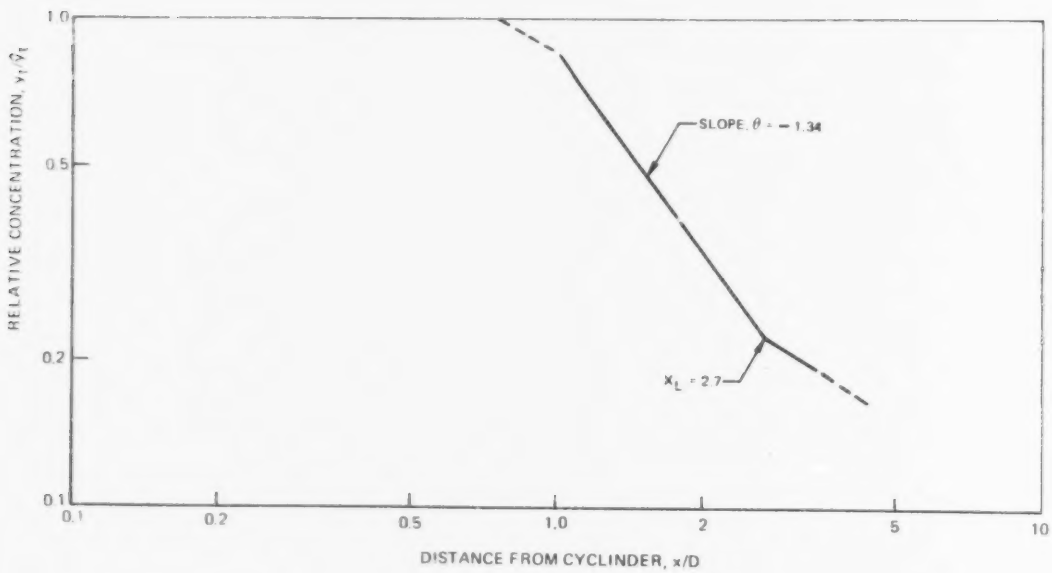

FIG. 31 TYPICAL TRACER CENTERLINE CONCENTRATION DISTRIBUTION

$$\frac{v_t}{v_t} \sim x^{\theta}; \qquad (x \leq x_L)$$

○ $\rho_\infty = 1.2\ kg/m^3$

□ $\rho_\infty = 0.67\ kg/m^3$

◇ $\rho_\infty = 0.41\ kg/m^3$

OPEN SYMBOLS: x_L / D

CLOSED SYMBOLS: $-\theta$

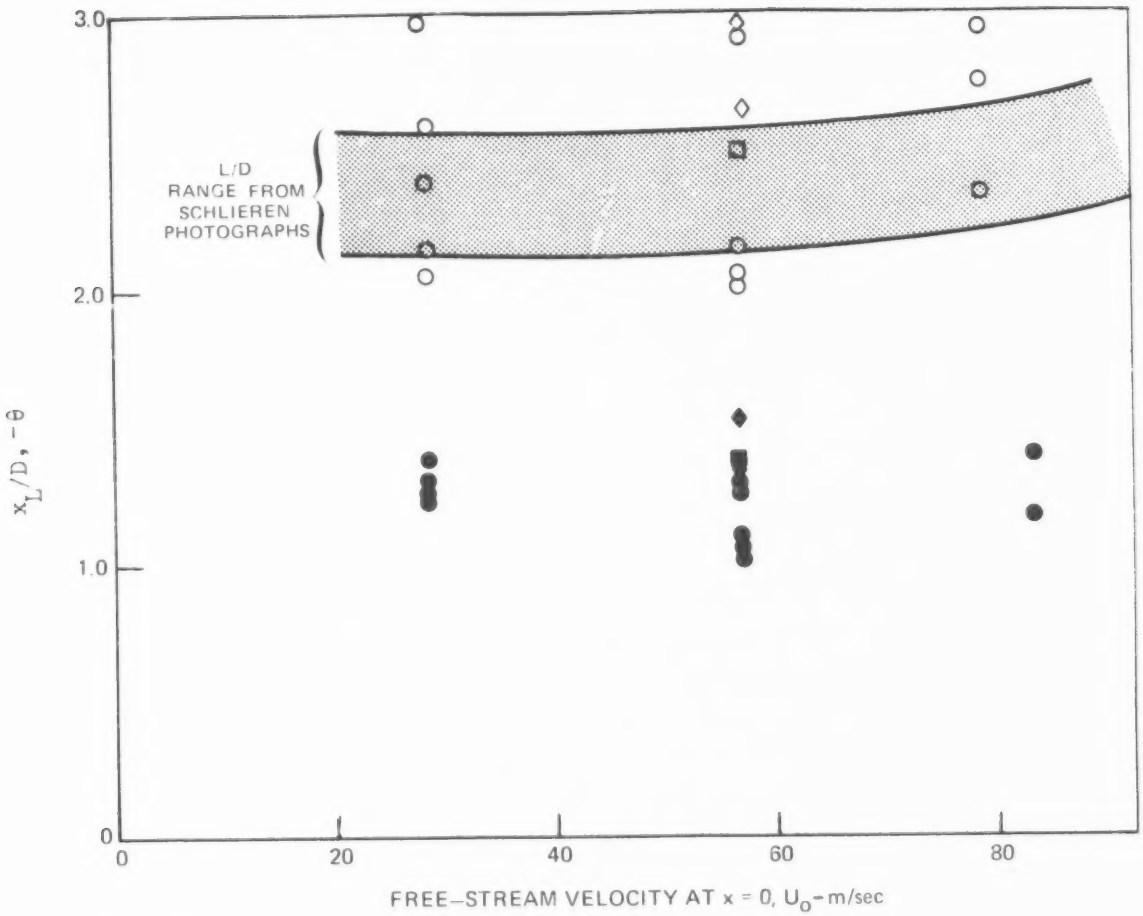

FIG. 32

TRACER CONCENTRATION DISTRIBUTION ON RECIRCULATION ZONE CENTERLINE

U_∞ = 24.0m/sec, ρ_∞ = 1.2 kg/m^3, SCREEN #1

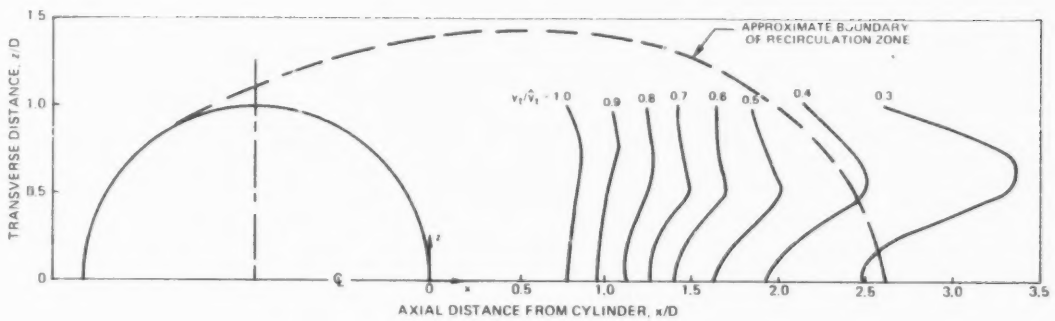

FIG. 33 TRACER CONCENTRATION CONTOUR MAP

TABLE XIII

TRACER CONCENTRATION DISTRIBUTION DATA

SCREEN (SEE TABLE X)	TRANSVERSE POSITION	CENTERLINE					Z/D = 0.25	Z/D = 0.50		
	R_o, KG-m^{-3}	1.2			0.67	0.41	1.2	1.2		
	U_o, M/SEC	24.0	48.0	72.0	48.0	48.0	24.0	24.0	48.0	72.0
	R_{e_D}	2.45×10^4	4.76×10^4	7.03×10^4	2.66×10^4	1.63×10^4	2.45×10^4	2.45×10^4	4.76×10^4	7.03×10^4
NONE	θ	1.29	1.1	1.17	1.09	1.52			1.15	
	*L/D	2.1	2.0	3.0	2.5	2.7			2.6	
1	θ	1.24	1.0	1.39	1.23		1.23	1.12	1.09	
	*L/D	3.0	3.0	2.4	—		3.1	3.0	3.0	
2	θ	1.29	1.05	—		1.32	1.36	—	1.06	
	*L/D	2.2	2.1			3.0	2.1		2.1	
3	θ		1.16		1.17		1.27	1.27		
	*L/D		2.2				2.4	2.4		
4	θ	1.26	1.03	1.13	1.17			1.1	1.2	1.21
	*L/D	2.4	2.3	2.6	3.0				2.0	2.0

TABLE XIII (CONT)
TRACER CONCENTRATION DISTRIBUTION DATA

SCREEN (SEE TABLE XI)	TRANSVERSE POSITION	Z/D = 0.50		Z/D = 0.75	Z/D = 1.0			
	R_o, KG-m^{-3}	0.67	0.41	1.2	1.2		0.67	0.41
	U_o, M/SEC	48.0	48.0	24.0	24.0	72.0	48.0	48.0
	R_{e_D}	2.66×10^4	1.63×10^4	2.45×10^4	2.45×10^4	7.03×10^4	2.66×10^4	1.63×10^4
SOME	θ	1.38	—	—	—	1.56	—	—
	*L/D	2.5	—	—	—	2.7	—	—
1	θ	1.33	—	1.15	1.41	—	—	—
	*L/D	—	—	2.6	2.65	—	—	—
2	θ	1.3	1.3	1.04	1.1	1.38	—	—
	*L/D	3.0	2.8	2.3	2.7	2.2	—	—
3	θ	1.35	1.33	1.02	1.1	—	—	1.1
	*L/D	2.2	3.4	2.6	2.2	—	—	—
4	θ	1.1	1.0	—	—	1.21	1.43	1.06
	*L/D	—	2.4	—	—	2.6	2.0	3.0

the motions within the recirculation zones operate to minimize transverse gradients and, therefore, a conceptually useful model of a one-dimensional recirculation zone might be appropriate.

It should be noted that the nature of the tracer concentration distributions found in the cold flow study reflect the absence of tracer in the outer flow. When a flame is anchored to the bluff-body, by contrast, chemical species including NO, and heat can move from the flame into the recirculation zone. Caution should be exercised, therefore, in applying the cold flow concentration data to the treatment of reacting flows.

SECTION V

ANALYTICAL INVESTIGATION

To assist in the interpretation of the results obtained from the combustion experiments (Section III) and to permit extrapolation of these results to conditions outside the range of the experimental investigation, an analytical model for nitric oxide formation in the combustor was developed. This analytical model is comprised of two separate parts: (1) a model for nitric oxide formation in the recirculation zone downstream from the flameholder and (2) a model for nitric oxide formation in the downstream flame as it spreads into the flow. In the following sections, the details of the two analytical models are presented and a comparison of the theoretical predictions with experimental results is made. Based on this comparison, certain limitations of the analytical models are apparent. These limitations are discussed and several recommendations for improved combustor modeling techniques are made.

V-A. RECIRCULATION ZONE MODEL FOR NITRIC OXIDE FORMATION

The experimental results obtained in the combustion experiments indicate that the gas temperature and species concentrations are essentially uniform throughout the recirculation zone. In the cold flow experiments, the variation of tracer concentration in the transverse direction in the recirculation zone was small, indicating that turbulent transport within the zone was moderately rapid. However, the observed axial decay of tracer concentration in the zone suggests that internal mixing rates are not sufficiently rapid to offset transport of tracer material out of the recirculation zone. In the combustion experiments, the observed recirculation zone temperature was found to be approximately 10% lower than the adiabatic combustion temperature for the freestream equivalence ratio. Furthermore, in both the combustion experiments and the cold flow experiments, the mass exchange rate between the recirculation zone and the outer flow could be characterized by a mean residence time. In the combustion experiments, the wake downstream from the flameholder was steady and did not exhibit vortex-shedding, as was observed in the cold flow experiments. All of the experimental observations outlined above are consistent with a model in which the recirculation zone, in the combustion experiments, is assumed to be a steady-state well-stirred reactor. The well-stirred reactor concept has been

applied to model the recirculation zone in an investigation of flame stabilization on bluff-body flameholders (Ref. 23). In the following section, a stirred reactor model for the recirculation zone is developed based on the analytical approach of Jones and Prothero (Ref. 24).

V-A.1. Stirred Reactor Model for the Recirculation Zone

It is assumed that the recirculation zone is an adiabatic, well-stirred reactor of volume $V(cm^3)$, containing combustion gas at pressure P(atm), density ρ (gm/cm^3) and uniform temperature $T(^\circ K)$. The overall flow rate of gas through the reactor is $\dot{m}(gm/sec)$ and the concentration of species S_i is denoted by σ_i°(mole/gm) on input and σ_i(mole/gm) on output.

The reaction mechanism for the stirred reactor may be written in the general form

$$\sum_i \nu'_{ij} S_i \rightleftharpoons \sum_i \nu''_{ij} S_i \qquad (15)$$

where ν'_{ij}, ν''_{ij} are integers representing the stoichiometric coefficients of species S_i in reaction j.

In steady-state operation, the governing equations for the stirred reactor may be written as follows:

Conservation of Mass

The mass conservation equation for each species S_i is given by

$$\frac{\dot{m}}{V}(\sigma_i^\circ - \sigma_i) = \sum_j (\nu'_{ij} - \nu''_{ij})(R_j - R_{-j}) \qquad (16)$$

where R_j and R_{-j} denote the overall forward and reverse reaction rates of reaction j. Eq. 16 states that the difference between the input and output flow rates of species S_i is equal to the net rate of production of species S_i by chemical reaction.

The overall reaction rates in Eq. 16 may be written:

$$R_j = k_j \prod_i (\rho\sigma_i)^{\nu'_{ij}}$$

$$R_{-j} = k_{-j} \prod_i (\rho\sigma_i)^{\nu''_{ij}}$$

where k_j, k_{-j} are the forward and reverse rate constants for reaction j. The general functional form of the rate constant k is:

$$k = A\, T^N \exp(E/RT)$$

Conservation of Energy

Conservation of energy for an adiabatic stirred reactor may be expressed by

$$\frac{\dot{m}}{V} \sum_i \left[\sigma_i^0 H_i^0(T^0) - \sigma_i H_i(T)\right] = 0 \qquad (17)$$

where $H_i^0(T^0)$ and $H_i(T)$ are temperature-dependent total molar enthalpies (cal/mole) (sensible enthalpy + chemical enthalpy) of species S_i in the input and output streams, respectively.

Equation of State

The gas in the stirred reactor is assumed to obey the perfect gas law,

$$P = \rho RT\sigma_m \qquad (18)$$

where R is the universal gas constant ($cm^3 \cdot atm/mole \cdot {}^\circ K$) and

$$\sigma_m = \sum_i \sigma_i$$

Eqs. 16 - 18 , together with appropriate values for the reactor input conditions, can be used to determine the composition, temperature and density of the gas in the reactor. These equations were programmed for computer solution using a Newton-Raphson iteration technique (Ref. 24). Use of reactor temperature as a dependent variable led to convergence difficulties; hence, it was necessary to carry out the calculations for a specified reactor temperature. In the computations discussed below, reactor gas compositions and densities were calculated for reactor temperatures encompassing the range of measured recirculation zone temperatures.

V-A.2 Calculation of Nitric Oxide Concentration in the Recirculation Zone

The stirred reactor model outlined in Section V-A.1 has been used to calculate the nitric oxide concentration in the recirculation zone for the conditions of the combustion experiments. In making these calculations, it is necessary to specify: (a) a reaction mechanism, (b) the reactor input conditions, (c) the reactor temperature and (d) the mean residence time of the gas in the reactor.

Reaction Mechanism

To calculate the nitric oxide concentration in the recirculation zone, two reaction mechanisms must be specified: (1) a nitric oxide formation mechanism and (2) a methane combustion mechanism. In the present investigation, it is assumed that nitric oxide is formed via an extended Zeldovich mechanism (Refs. 25 and 26),

$$O + N_2 \underset{k_{-19}}{\overset{k_{19}}{\rightleftharpoons}} NO + N \qquad (19)$$

$$N + O_2 \underset{k_{-20}}{\overset{k_{20}}{\rightleftharpoons}} NO + O \qquad (20)$$

$$N + OH \xrightarrow{k_{21}} NO + H \qquad (21)$$

The forward and reverse rate constants for Reactions 19 and 20 were taken from Ref. 27, and the forward rate constant for Reaction 21 was taken from Ref. 19. These rate constants are tabulated below

$$k_1 = 1.36 \times 10^{14} \exp(-75{,}400/RT) \text{ cm}^3/\text{mole} \cdot \text{sec}$$

$$k_{-1} = 3.10 \times 10^{13} \exp(-334/RT) \text{ cm}^3/\text{mole} \cdot \text{sec}$$

$$k_2 = 6.43 \times 10^{9} \, T \exp(-6250/RT) \text{ cm}^3/\text{mole} \cdot \text{sec}$$

$$k_{-2} = 1.55 \times 10^9 \, T \exp(-38{,}640/RT) \text{ cm}^3/\text{mole} \cdot \text{sec}$$

$$k_3 = 4.0 \times 10^{13} \text{ cm}^3/\text{mole} \cdot \text{sec}$$

where R = universal gas constant = 1.986 cal/mole°K and T is temperature (°K).

The nitric oxide formation process in the recirculation zone is coupled to the hydrocarbon chemistry. Two different degrees of coupling were considered in the present investigation. Initially, it was assumed that the nitric oxide formation process was decoupled from the hydrocarbon chemistry, and that the C-H-O chemistry was equilibrated prior to the onset of nitric oxide formation. In the context of this mechanism, the concentrations of C-H-O species were assumed to be in equilibrium at the measured recirculation temperature. As noted in Section III, the reduced recirculation zone temperature could not be explained in terms of heat transfer to the flameholder and test section walls. Longwell et al. (Ref. 23) have measured unreacted O_2 in the recirculation zone of bluff-body stabilized flames. In the present experiments, substantial departures from equilibrium were observed for radical concentrations in the recirculation zone. Hence, it seems reasonable to attribute the reduced recirculation zone temperature to unreacted fuel in the zone. The equilibrium calculations were carried out assuming adiabatic conditions with an amount of fuel unreacted so that the equilibrium temperature was equal to the measured recirculation zone temperature. The concentrations of O, OH and O_2 obtained from this equilibrium calculation were used, together with Eqs. 19 - 21 , to calculate the concentration of N and NO in the recirculation zone.

In the combustion experiments, measured OH-radical concentrations in the recirculation zone were significantly in excess of the concentrations calculated for a stirred reactor, assuming C-H-O equilibrium, Fig. 15. This observation indicates that the nitric oxide formation process in the recirculation zone may be closely coupled to the hydrocarbon chemistry. To model the case of coupled nitric oxide formation and hydrocarbon chemistry, the stirred reactor calculations were carried out using Eqs. 19 - 21 , together with the measured OH concentration and inferred O-atom concentration. Several investigators (Refs. 28, 29) have shown that various rapid bimolecular reactions involving radical species equilibrate early in the combustion process, prior to attainment of total equilibrium. The partial equilibration of these bimolecular reactions result in the concentrationsof various radical species being

inter-related. In the present study, the O-atom concentration was calculated from the measured OH concentration by invoking the partial equilibrium approximation for the rapid bimolecular reaction

$$OH + OH \rightleftharpoons O + H_2O \qquad (22)$$

The O-atom concentration is given by

$$C_O = K_{22}(T) \; C^2_{OH} / C_{H_2O}$$

where $K_{22}(T)$ is the equilibrium constant for Reaction 22 at the measured recirculation zone temperature. For the conditions of the present investigation, no significant error in the calculation of the O-atom concentration is introduced by using the equilibrium water concentration.

Reactor Input Conditions

The input conditions which must be specified for the stirred reactor calculations are the temperature and species concentrations in the input stream. The composition of the input stream is some mixture of burned and unburned gas, containing some of the radicals and nitric oxide formed in the flame zone surrounding the recirculation zone. The composition of the input stream cannot be well-defined since the state of the gas transported into the zone from the outer flow is not known. Hence, in the present calculation, the input concentration of all species except OH, O, N and NO were set equal to the equilibrium values associated with the recirculation zone temperature. The input concentrations of OH and O were set equal to their equilibrium values in the uncoupled stirred reactor model and to their measured (or inferred) non-equilibrium values in the coupled model. For all of the calculations, the input concentrations of N and NO were set equal to zero.

Reactor Temperature

As noted earlier, use of the reactor temperature as a dependent variable led to convergence difficulties in the stirred reactor numerical calculations; hence, in these calculations the reactor temperature was specified equal to the measured recirculation zone temperature. To determine the sensitivity of the predicted nitric oxide concentrations in the recirculation zone, the reactor temperature was varied ± 100°K

from the recirculation zone temperature.

Mean Residence Time

To obtain a solution to the governing equations for the stirred reactor, a value for the parameter $\dot{m}/V$ must be specified. For a well-stirred reactor, the parameter $\dot{m}/V$ may be expressed as, (Ref. 30)

$$\frac{\dot{m}}{V} = \frac{\tau_t}{\rho}$$

where τ_t is the mean residence time of gas elements in the reactor and ρ is an appropriate gas density. In the present computations, the mean residence time was taken equal to the measured residence time, (see Section III-D).

V-B. DESCRIPTION OF THE MIXING-COMBUSTION ANALYSIS

A flow diagram of the two-dimensional (x,z) bluff-body flow field to be modeled is shown in Fig. 34a. Distribution of the velocity, temperature, and species concentrations in the premixed methane-air stream and the high temperature near-wake region at the bluff-body location are assumed to be known. The mixing and chemical reaction between the outer, cold flow and the inner high temperature wake region is treated by dividing the combustor into a large number of stations a distance Δx apart, and solving the conservation equations in the manner of an initial value problem with the conditions at the end of one Δx segment becoming the initial conditions for the following segment. For a typical problem, the number of segments usually exceeds 5,000. Within each segment of the combustor there are a number of streamlines (20-30 for the present calculations) along which mixing is assumed to proceed independently of any chemical reaction effects. Therefore, when equations describing the conservation of mass, momentum, species concentration, and energy are written for the segment, terms involving the generation of heat and the production or loss of chemical species are omitted. After the fluid within the segment has mixed, chemical reaction effects are introduced on the basis of average conditions in Δx. This explicit coupling procedure has been adopted in order to avoid excess computation time.

In carrying out the analysis, the pressure is assumed to be a function only of the axial coordinate, that is, $P = P(x)$. The turbulent shear

a) BURNER FLOW SYSTEM TO BE MODELED

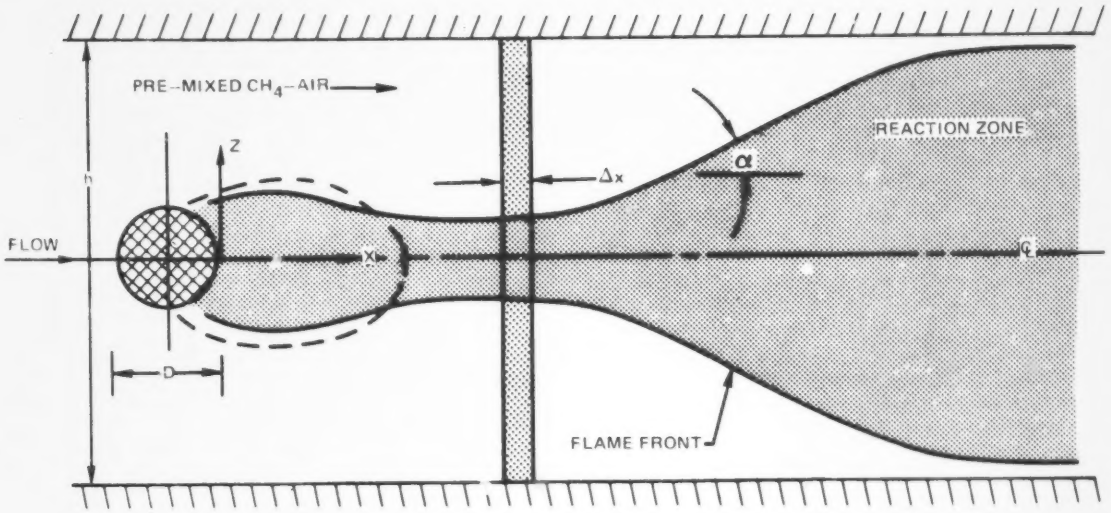

b) INITIAL CONDITIONS (x = 0)

INITIAL VELOCITY = $U_\infty (1/(1-B_R))$

INITIAL PRESSURE: AS MEASURED AT x = 0

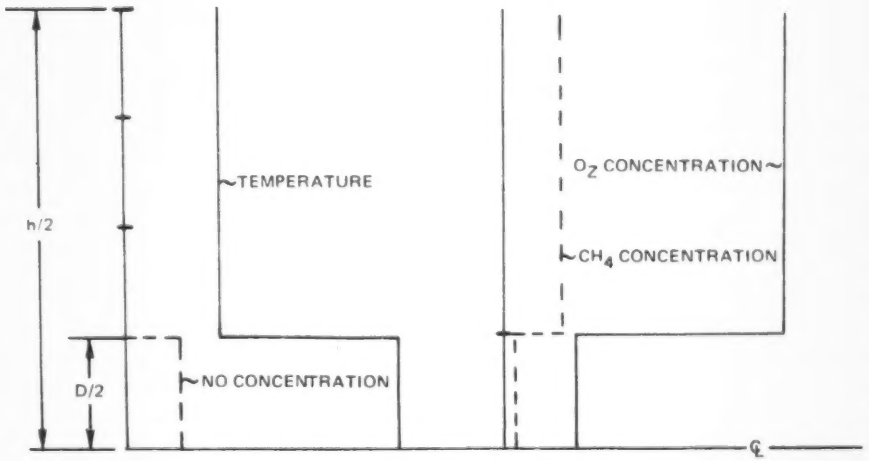

FIG. 34 **ANALYTICAL MODEL**

stress in the conservation of momentum equation is taken as the product of an eddy viscosity and the local velocity gradient in the manner of Boussinesq (cf., Ref. 10). Lewis and Prandtl numbers are taken equal to unity, eliminating distinction between the eddy coefficients of momentum, mass and heat. The conservation equations are transformed by the method of von Mises (cf., Ref. 31) from the physical (x, z) plane into a coordinate system in which streamlines are parallel, thereby yielding expressions of the "heat conduction" type. These are subsequently put in a form suitable for numerical solution by substituting finite difference approximations for all derivatives.

The solution of the resulting finite difference equations for each segment, Δx, is obtained for an incremental change in pressure which is impressed on the flow between the beginning of the segment, where all conditions are specified, and the end of the segment. The initial conditions typically are given as step profiles of temperature, velocity and species concentrations (Fig. 34b); within the Δx segment, the gas streams mix at a rate determined by the eddy viscosity which is a function of flow conditions. Conditions at the end of the segment are checked for compatibility by employing the conservation of mass. If inconsistencies are found, the pressure change across the segment is adjusted and the entire calculation is repeated until mass conservation is obtained.

Chemical reaction effects are coupled into the analysis at this point. Average values of temperature, pressure, concentrations, and velocity for all streamlines between the two stations are calculated and a test is made to determine if methane-air ignition has occurred locally (see later discussion of Eq. 39). In the event that ignition has not occurred along a particular streamline, no further chemistry computations are carried out for that streamline in the segment under consideration. For those streamlines on which ignition has occurred, the flow conditions determined for the segment under consideration are applied to the calculation of the equilibrium composition and temperature of the methane-air reacting gas mixture. In this calculation, a successive approximation procedure is used to find the simultaneous solution of the standard equations of chemical equilibria, conservation of (atomic) mass, and conservation of energy. Equilibrium CH_4-air reaction concentrations and temperature are subsequently applied to the calculation of NO concentration from auxiliary kinetics expressions. Finally, conditions at the downstream station are adjusted to reflect all chemical reaction effects to complete the analytical proce-

dure. The entire procedure is then repeated between the current station and the next station further downstream, and so on, until the entire reacting flow field is mapped out.

Other assumptions used in the analytical development include: (1) perfect gases, (2) adiabatic wall conditions, (3) turbulent eddy viscosity is much larger than the molecular viscosity.

V-B.1. Governing Equations

The system of (n + 6) equations which describes the mixing of variable density, turbulent streams within the framework of the present model has been derived by Vasiliu (Ref. 32). The well-known turbulent boundary layer assumptions were applied in this derivation. These equations contain the (n + 6) time-averaged unknowns m_i (i = 1, 2, . . ., n) ρ, u, v, P, H, and T, and the eddy viscosity, ϵ. Thus, once the eddy viscosity is specified, all parameters may be determined at every point throughout the flow field for selected boundary conditions. The governing equations include the perfect gas law, a relation for the specific enthalpy, and the following:

Global Continuity:

$$\frac{\partial(\rho u)}{\partial x} + \frac{1}{z^{\delta}} \frac{\partial(\rho v z^{\delta})}{\partial z} = 0 \tag{23}$$

Species Continuity:

$$\rho u \frac{\partial m_i}{\partial x} + \rho v \frac{\partial m_i}{\partial z} = \frac{\epsilon}{z^{\delta}} \frac{\partial}{\partial z} \left[z^{\delta} \frac{\partial m_i}{\partial z} \right] \tag{24}$$

Conservation of Momentum:

$$\rho u \frac{\partial u}{\partial x} + \rho v \frac{\partial u}{\partial z} = - \frac{dP}{dx} + \frac{\epsilon}{z^{\delta}} \frac{\partial}{\partial z} \left[z^{\delta} \frac{\partial u}{\partial z} \right] \tag{25}$$

Conservation of Energy:

$$\rho u \frac{\partial H}{\partial x} + \rho v \frac{\partial H}{\partial z} = \frac{\epsilon}{z^{\delta}} \frac{\partial}{\partial z} \left[z^{\delta} \frac{\partial H}{\partial z} \right] \tag{26}$$

Area Relation:

$$\int_z \rho u (2\pi z)^{\delta} \, dz = \text{CONSTANT} \tag{27}$$

In the above equations, δ is zero or unity depending on whether a two-dimensional or axisymmetric flow is being considered.

The transformation of Eqs. 23 through 26 by the method of von Mises requires the introduction of the stream function, ψ. In order to limit ψ to the region $0 \leq \psi \leq 1$ the following defining expressions are utilized for the stream function:

$$\frac{\partial \Psi}{\partial z} = \frac{\rho u}{Gh} \left(\frac{2z}{h} \right)^{\delta} \tag{28}$$

$$\frac{\partial \Psi}{\partial x} = - \frac{\rho v}{Gh} \left(\frac{2z}{h} \right)^{\delta} \tag{29}$$

where G is the total mass flux. Transforming Eqs. 23 through 26 by the application of Eqs. 28 and 29 with the nondimensional independent variables

$$\xi \equiv \frac{x}{L} \tag{30}$$

$$\eta \equiv \frac{2z}{h} \tag{31}$$

yields:

Species Continuity:

$$\frac{\partial m_i}{\partial \xi} = \beta \epsilon \frac{\partial}{\partial \Psi} \left[\rho u \eta^{2\delta} \frac{\partial m_i}{\partial \Psi} \right] \tag{32}$$

Conservation of Momentum:

$$\frac{\partial u}{\partial \xi} = -\frac{1}{\rho u}\frac{dP}{d\xi} + \beta\epsilon\frac{\partial}{\partial \Psi}\left[\rho u \eta^{2\delta}\frac{\partial u}{\partial \Psi}\right] \tag{33}$$

Conservation of Energy:

$$\frac{\partial H}{\partial \xi} = \beta\epsilon\frac{\partial}{\partial \Psi}\left[\rho u \eta^{2\delta}\frac{\partial H}{\partial \Psi}\right] \tag{34}$$

with $\beta \equiv D/(Gh)^2$.

The parabolic Eqs. 32 - 34 were put in finite difference form to allow their solution by numerical methods on a Univac 1108 computer. This is equivalent to replacing the continuous flow system by a rectangular finite grid network having an axial grid size of $\Delta\xi$ and a transverse grid size of $\Delta\psi$. In general, neither $\Delta\xi$ nor $\Delta\psi$ need be constant. Both ξ and ψ are in non-dimensional form and vary from zero to unity.

V-B.2. Eddy Viscosity Model

Before the system of finite difference equations can be solved, it is necessary to specify the variation of the transport coefficient or eddy viscosity for the reacting turbulent flow downstream of the recirculation zone. From Eq. 3 and again taking the mixing layer width to grow linearly in the flow direction, Ref. 9, it follows that

$$\epsilon/\hat{\rho} \sim b u_{\mathfrak{C}} \tag{35}$$

where $b = 0.27x$ for $b \leq h/2$ and $b = h/2$ thereafter. A local centerline velocity, $u_{\mathfrak{C}}$, is used to account for the flow acceleration which accompanies the pressure drop in an enclosed combustor. The reference density for mixing flows is taken from Ref. 33, with the result,

$$\epsilon = c_1\left[\frac{1+\rho_\infty/\rho_{\mathfrak{C}}}{2}\right]^{0.8} b u_{\mathfrak{C}} \tag{36}$$

where c_1 is a constant to be determined from experiment.

V-B.3. Chemistry

V-B.3i. Ignition Delay Time for CH_4-Air - Once mixing has occurred between two adjacent stations separated by a distance Δx, linear averages of the dependent variables may be computed on every streamline in Δx and applied to the determination of the ignition delay time, τ_{ID}, from data correlations. The dwell time, $\Delta\tau$, defined as

$$\Delta\tau \equiv \Delta x / \bar{u} \tag{37}$$

also may be calculated. This quantity is a measure of the average time fluid spends in the region Δx. The ignition delay time corresponds to the length of the preignition period during which little change in temperature or species concentration occur. Heat generation and conversion of reactive species occurs at equilibrium following the ignition delay time.

Ignition delay times were found from the high temperature portion of the CH_4-air data (Ref. 74) presented in Fig. 35. That is, for $\bar{T} \geq 1800°K$,

$$\tau_{ID} = 6.2 \times 10^{-22} C_{CH_4}^{0.4} C_{O_2}^{-1.6} \exp(44{,}280/\bar{T}) \tag{38}$$

where C_i denote species concentrations in moles/cc.

The ignition criteria used presumes that ignition occurs on any streamline at the axial location where the following condition is satisfied:

$$\sum_x \frac{\Delta\tau}{\tau_{ID}} \geq 1.0 \tag{39}$$

Once ignition has occurred on a given streamline, subsequent reaction between methane and oxygen is assumed to proceed to equilibrium instantaneously.

V-B.3ii. Equilibrium Chemistry Calculation for Fuel-Air Combustion - To calculate the equilibrium composition, expressed as a mole fraction, y_i, for each of n chemical species, for a given stoichiometry, temperature,

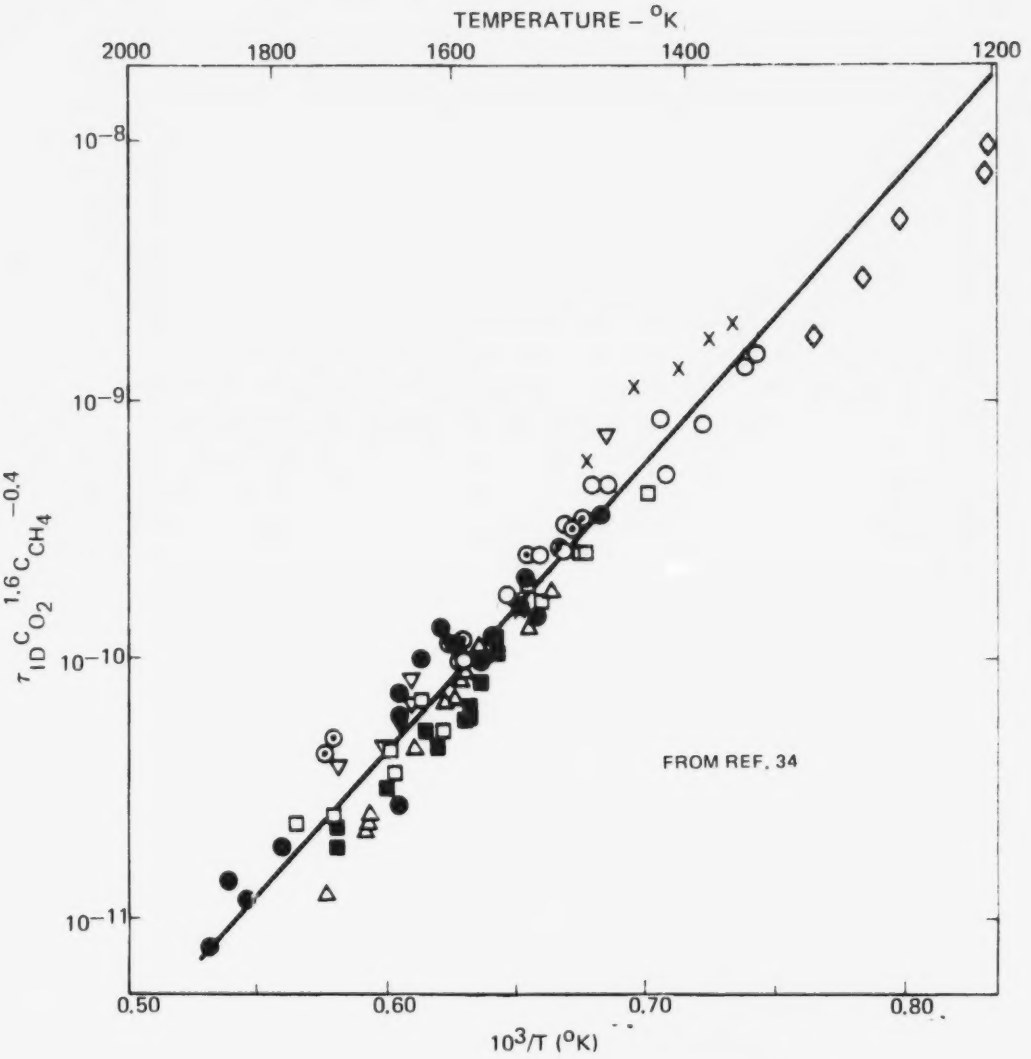

FIG. 35 **METHANE–AIR IGNITION DELAY TIMES**

and pressure at a station, the following equations must be satisfied:

Material balance: for each of q different atoms present in the n different chemical species,

$$N \sum_{i=1}^{n} \nu_{ij} y_i = b_j \tag{40}$$

$$y_i \geq 0 \quad (i = 1, 2, \ldots, q)$$

where N is the total (variable) number of moles of species present in the mixture, ν_{ij} is the stoichiometric coefficient for a given atom j in a given chemical species i (for example, for the hydrogen atom count in methane, CH_4, $\nu = 4$), and b_j equals the total number of atoms of j present in the system as specified by the input stoichiometry.

Free-energy minimization: the chemical potential (ie., the partial molar Gibbs free-energy) of the ith chemical species, μ_i, is given as

$$\mu_i - \mu_i^\circ = RT \ln (f_i / f_i^\circ) \tag{41}$$

where f_i is the fugacity of the ith species, and superscript $^\circ$ refers to the standard state of pure i taken as pure gas at unit pressure. Introducing the assumption of an ideal gas and a perfect mixture, there results

$$\mu_i = \mu_i^\circ + RT \ln p_i \tag{42}$$

in which p_i is the partial pressure of i in the mixture in atmospheres Thus, the total free energy, F, of the system is

$$F = N \sum_{i=1}^{n} y_i \mu_i \tag{43}$$

or, since $p_i = y_i P$, where P is the total pressure in atmospheres,

$$F = N \sum_{i=1}^{n} y_i \left(\mu_i^\circ + RT \ln P + RT \ln y_i \right) \tag{44}$$

The free energy per mole of pure i, μ_i°, can be obtained from the literature where it is tabulated as a function of temperature up to 6000°K, Ref. 35. This is the only species property required for solution of the equilibrium problem. The values of P and T are specified conditions.

Chemical equilibrium is attained when the total free energy of the system is a minimum. The problem, then, is to determine the set of values, y_j, which will minimize Eq. 44 , subject to the q constraints of Eq. 40. A computer program developed to solve this system of equations was incorporated into the present analytical procedure.

V-B.3iii. Nitric Oxide Formation Kinetics - For the present analytical model, all chemical species with the exception of nitric oxide (NO) and atomic nitrogen (N) are assumed to be in local chemical equilibrium on any streamline for which ignition has occurred, ie., where Eq. 39 has been satisfied. The nitric oxide concentration is determined following the equilibrium chemistry calculation using equilibrium conditions in an auxiliary chemical kinetics model.

The kinetics of formation of nitric oxide is modeled using a two-reaction mechanism (Ref.25):

$$O + N_2 \underset{k_{-19}}{\overset{k_{19}}{\rightleftarrows}} NO + N \qquad (19)$$

$$N + O_2 \underset{k_{-20}}{\overset{k_{20}}{\rightleftarrows}} NO + O \qquad (20)$$

Invoking a steady-state approximation for N, the nitric oxide formation rate may be expressed as,

$$\frac{dC_{NO}}{dt} = \frac{2k_{19}C_O C_{N_2}\left[1 - C_{NO}^2/KC_{N_2}C_{O_2}\right]}{1 + k_{-19}C_{NO}/k_{20}C_{O_2}} \qquad (45)$$

where C_i = concentration of species i (moles/cm^3), k_j = forward rate constant of reaction j (cm^3/mole-sec), k_{-j} = reverse rate constant of reaction j (cm^3/mole-sec) and $K = k_{19}k_{20}/k_{-19}k_{-20}$. Values for the rate constants in Eq. 45 were taken from Ref. 27, and tabulated earlier in Section V-A.

In the present calculations, Eq. 45 was used to calculate the nitric oxide formation rate assuming that O, O_2 and N_2 are in local chemical equilibrium. The quantity of NO formed on any streamline in Δx subsequently is added to the existing NO produced upstream of Δx, and all remaining species are adjusted to reflect chemical reaction effects before proceeding to the next downstream computational station.

V-C. COMPARISON OF EXPERIMENTAL AND ANALYTICAL RESULTS

V-C.1 Measured and Predicted Nitric Oxide Concentrations in the Recirculation Zone

The stirred reactor model, discussed in Section V-A, was used to compute nitric oxide concentrations in the recirculation zone for the conditions of the combustion experiments. The predicted nitric oxide concentrations are tabulated in Table VIII for a range of inlet velocities and equivalence ratios. In addition, typical comparisons of the predicted nitric oxide concentrations with measured values are illustrated in Figs. 16a and 16b. The equilibrium stirred reactor model predicts nitric oxide concentrations in the recirculation zone which are substantially less than were observed in the experiment. The non-equilibrium stirred reactor model, using measured radical concentrations, predicts nitric oxide concentrations which are relatively close to, although somewhat less than, the measured concentrations. In the stirred reactor model, it was assumed that the nitric oxide concentration in the input stream was zero. The difference between nitric oxide concentrations predicted by the non-equilibrium stirred reactor model and measured concentrations may be attributed to nitric oxide formed in the flame zone surrounding the recirculation zone and transported into the zone.

The non-equilibrium stirred reactor model correctly predicts trends in the variation of recirculation zone nitric oxide concentration with equivalence ratio and inlet velocity. The difference between the predicted and measured nitric oxide concentrations decreases as the inlet velocity increases. This trend may reflect an improvement in mixing rates in the recirculation zone as the flame bounding the zone undergoes a transition from laminar to turbulent with increasing inlet velocity (see Section III-B).

In two recent investigations of nitric production in stirred reactors (Refs. 30, 36), observed nitric oxide concentrations were substantially larger than the concentrations predicted by analytical models which

decouple the combustion chemistry from the nitric oxide chemistry. Predicted nitric oxide concentrations obtained from models which couple the nitric oxide chemistry to a detailed combustion mechanism for hydrocarbon fuels also were lower than observed concentrations. However, in both of these investigations, no attempt was made to measure radical concentrations in the stirred reactor. Without a measure of the concentrations of radical species, it is difficult to assess the validity of the analytical models used in these two studies.

Based on the foregoing observations, it is reasonable to conclude that a well-stirred reactor is a satisfactory model for the recirculation zone for the conditions investigated in the combustion experiments, providing some aspects of non-equilibrium hydrocarbon chemistry are included in the model.

V-C.2 Measured and Predicted Nitric Oxide Concentrations in the Exhaust Gas

The turbulent mixing/reaction model discussed in Section V-B, was applied to the computation of flame angles and temperature, velocity, and species concentrations in a two-dimensional combustor containing a cylindrical bluff-body flameholder (Fig. 34a). The four sets of flow conditions listed in Table XIV were investigated for the geometry of the burner rig. In the absence of definitive information, the inner hot region was assumed to have the same initial velocity as the outer pre-mixed methane-air cold flow. The initial temperature and nitric oxide concentration in the inner hot zone were taken from the burner experimental data discussed in Section III. Similarly, the inital pressure used in the calculation was taken from measurements at the bluff-body location (Fig. 34b).

Gradients of velocity, temperature, and species concentration were taken equal to zero at the combustor center-plane and at the combustor walls. As a result, wall boundary layer processes were not properly simulated in the analytical model.

The first task in the analytical study was the determination of the constant c_1 in Eq. 36. This was done by varying c_1 in calculations with test conditions number 2, Table XIV, until predicted and measured flame spreading angles were in agreement. The constant, c_1, was established at the value 0.121, which is consistent with the constant density, two-dimensional jet mixing value of 0.0135 (Ref. 37). Hence, c_1

TABLE XIV

SUMMARY OF ANALYTICAL RESULTS

TEST CASE	U_∞ (M/SEC)	Φ	TAN α_{max}		AV. NO CONC. (PPM--DRY BASIS BY WT.)		
			CALCULATED	MEASURED	CALCULATED		MEASURED
					X/D = 20	44	X/D = 44
1	20	0.778	0.057	–	0.6	–	65 ± 15
2	20	0.875	0.075	0.075	4.0	9	96 ± 10
3	20	0.972	0.079	0.082	10.0	19	140 ± 10
4	40	0.972	0.055	0.063	1.3	–	67 ± 15

was fixed at 0.0121 in the remaining analytical effort involving test cases 1, 3 and 4.

Analytical results presented in Figs.36- 39 for test case 2 are typical of all four test cases. The ignition envelope, which is a curve drawn through those points in the flow field where the ignition criterion, Eq. 39, is first satisfied, is shown in Fig.36. For purposes of this study, the ignition envelope and the flame boundary are coincident. The calculated flame boundary, in agreement with photographic observations (Fig. 9), initially necks down. Approximately 6 to 8 body diameters downstream from the bluff-body location, the flame begins to spread into the pre-mixed outer flow, ultimately displaying a growth which is linear with axial distance. The linear spread of the flame is conveniently characterized by the maximum flame angle α_{max}. At a distance downstream from the bluff-body of approximately 20 body-diameters, the analysis predicts that the flame reaches the burner wall. This behavior, which is at variance with the experimental observation that the flame bends away from the burner wall, results from incorrect boundary conditions. It is expected, however, that the details of the flow field are realistic throughout the burner except in the immediate vicinity of the burner wall.

Predicted flame angles for the four test cases are given in Table XIV and Figs. 10a and 10b. The correct trends of flame angle variation with approach flow velocity and equivalence ratio are reproduced.

Computed velocity profiles and nitric oxide concentration distributions throughout the flow field are shown in Figs.37 and 38 . As expected, the entire flow accelerates in the constant area burner. The hot, low density inner flow is accelerated more rapidly than the outer cold flow, however, thereby producing the characteristic reacting wake flow velocity distribtion. The spread of the flame into the cold flow is apparent in both Figs. 37 and 38. Note that at an axial distance of x/D = 24, essentially all of the flow has ignited and the methane-air chemistry is completed. However, nitric oxide production continues until the end of the burner at station x/D = 44 (Fig. 39). As a result, the NO concentration doubles in the last half of the burner test section. The buildup of CO, CO_2, and NO, in the reacting methane-air flow can be followed by referring to Fig. 39. It is predicted, for test case 2, that approximately nine ppm (dry basis by weight) of NO will be produced in the burner. Nitric oxide production

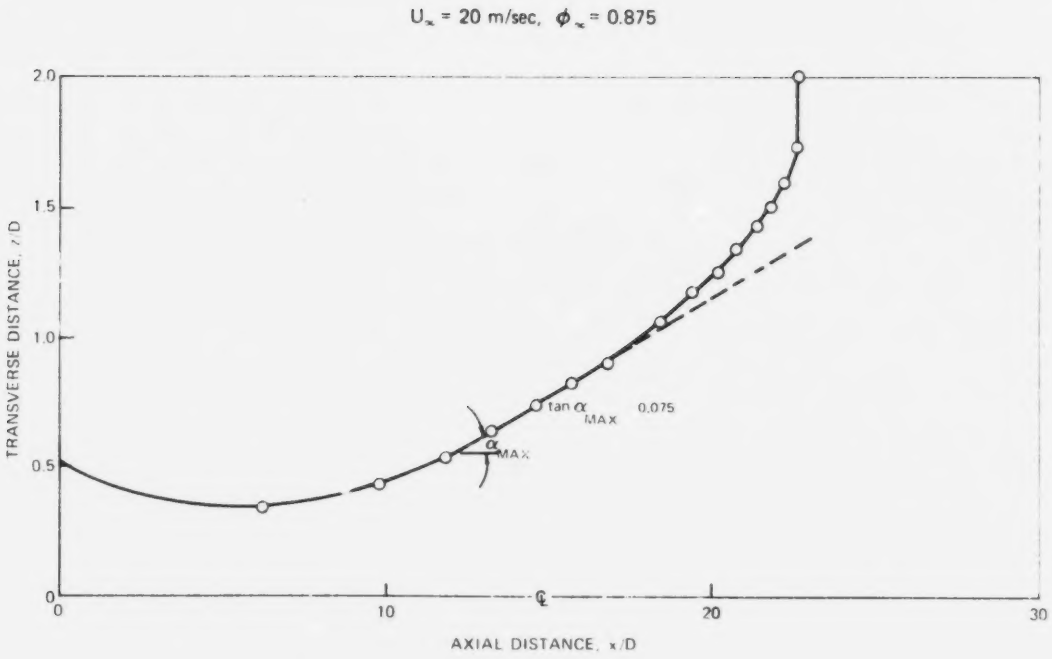

FIG 36 **CALCULATED FLAME BOUNDARY**

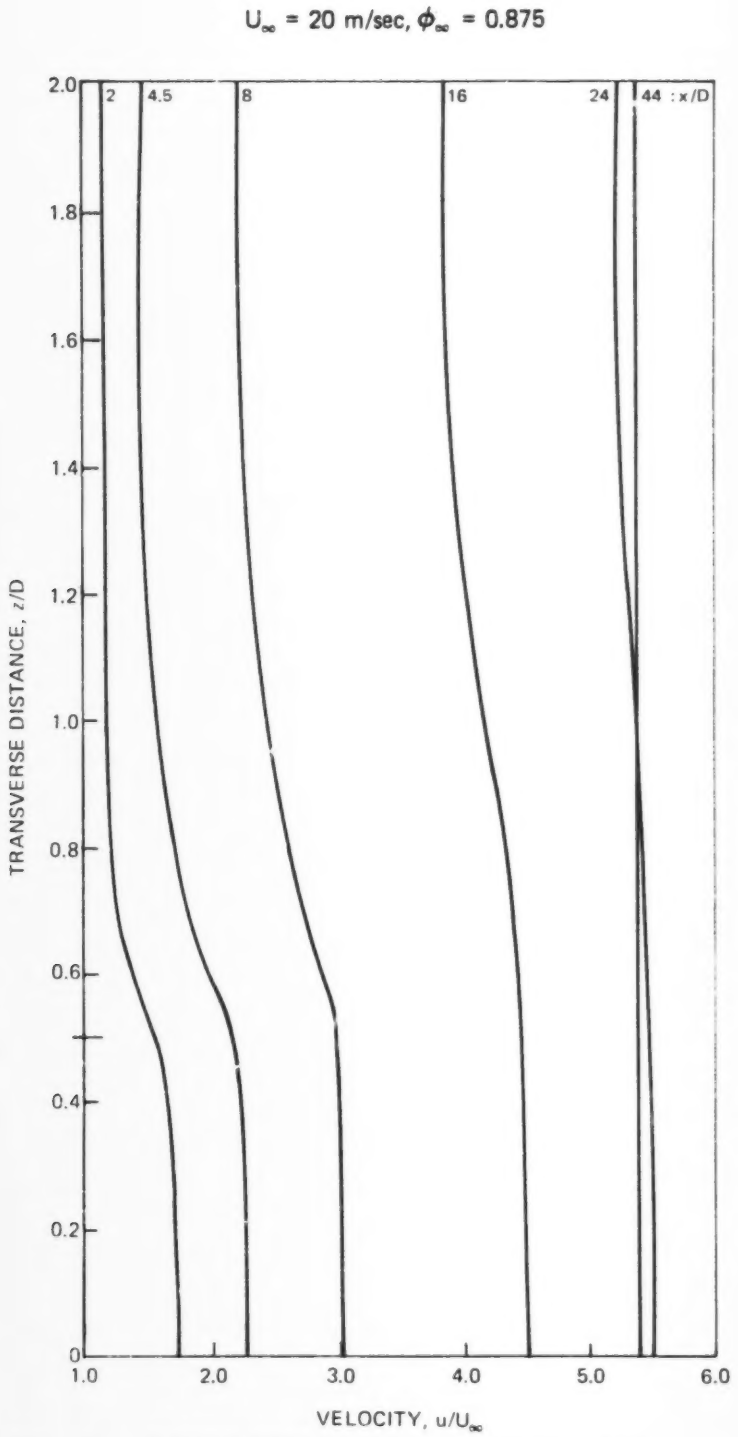

FIG. 37 **CALCULATED WAKE VELOCITY PROFILES**

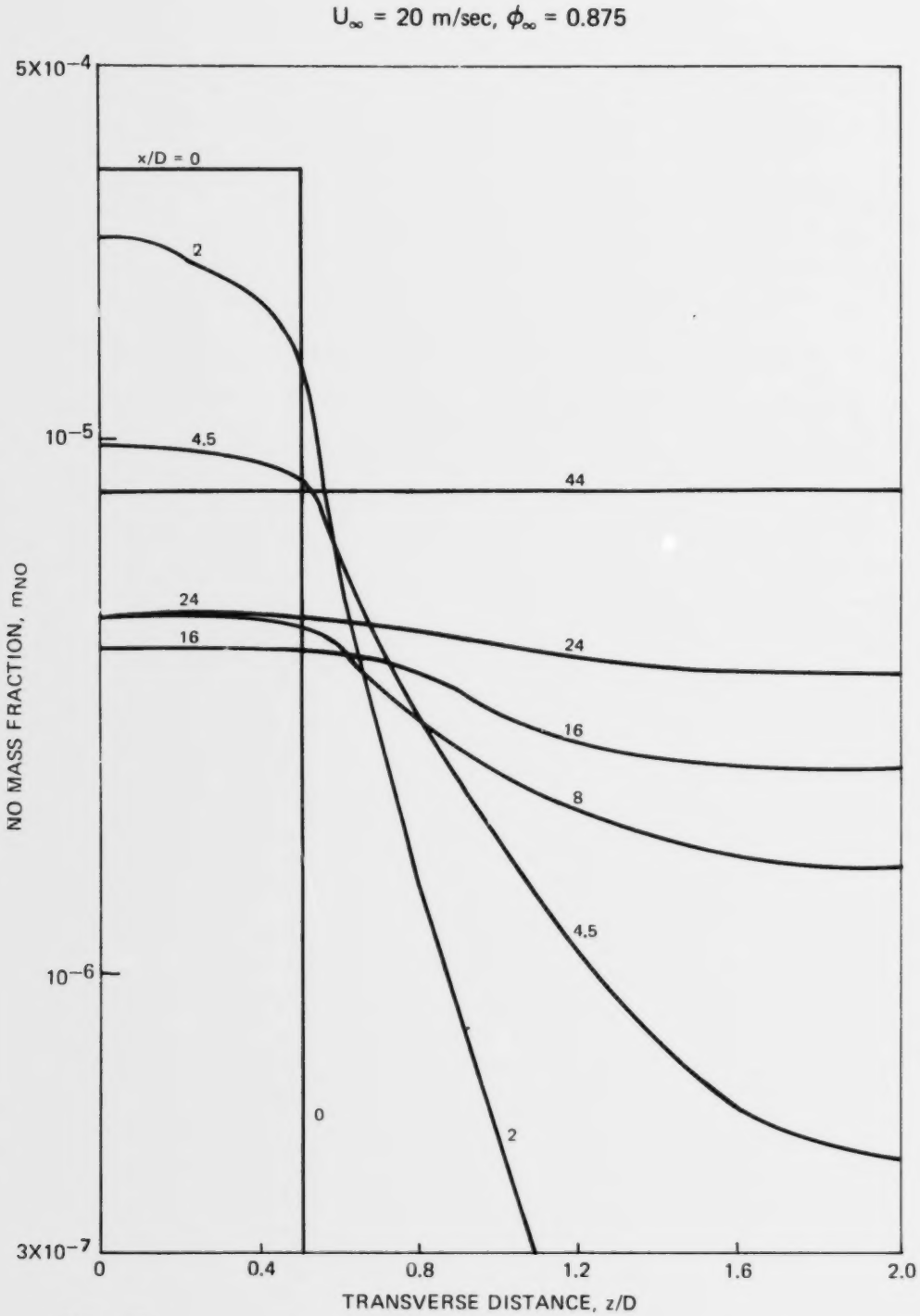

FIG. 38

NO CONCENTRATION DISTRIBUTION

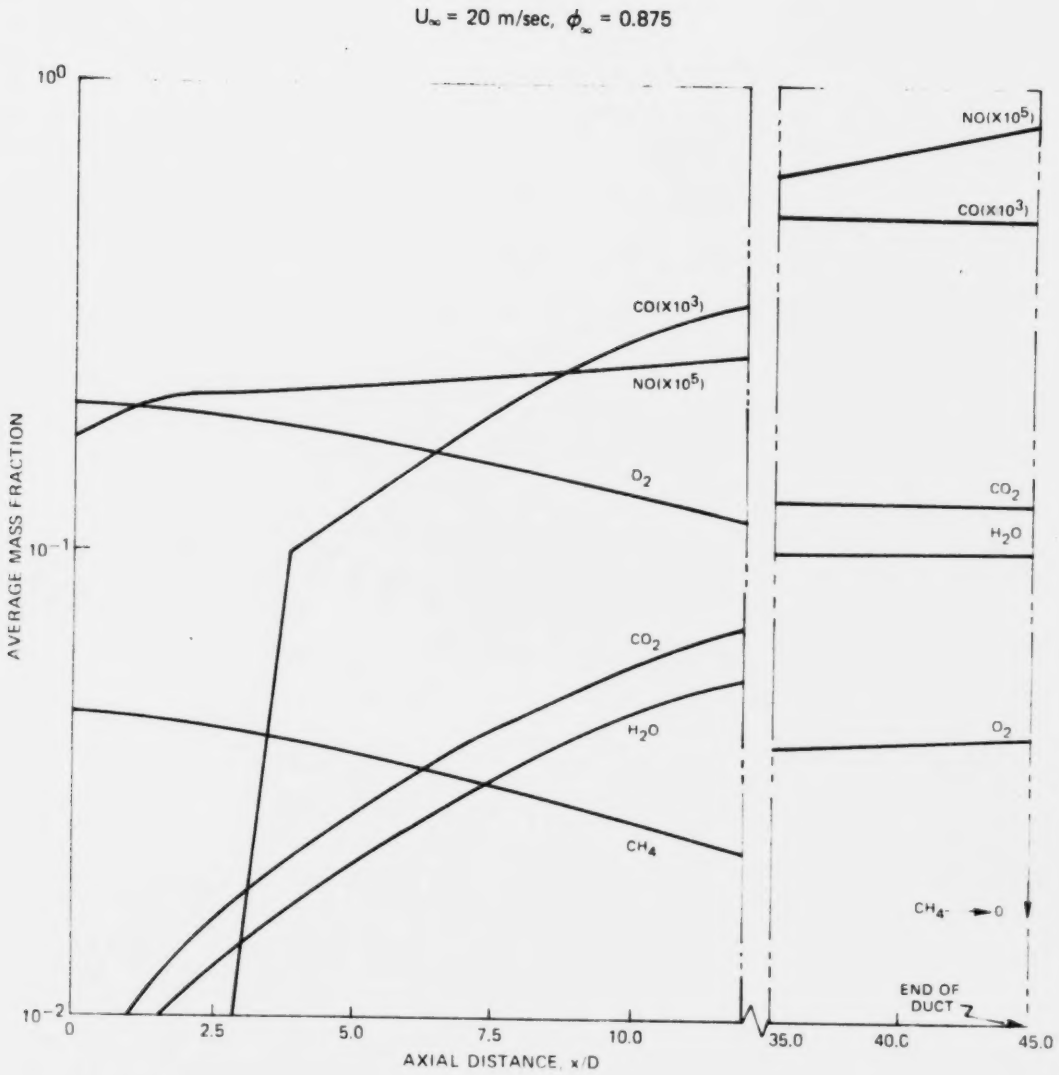

FIG 39 **CALCULATED SPECIES DISTRIBUTIONS**

levels for the other test cases are listed in Table XIV. In general, the predicted nitric oxide production levels are significantly lower than the levels measured at the burner exit using a time-of-flight mass spectrometer.

The analytical model correctly predicts the essential features of the flame spreading process in the burner. Hence, it is likely that the predicted distributions in the mean flow properties in the burner, ie., temperature, density and velocity are reasonably close to the actual distributions. It is suspected, therefore, that the discrepancy between predicted and measured nitric oxide concentrations can be attributed to two of the assumptions made in the analytical model. First, in the modeling of the methane-air chemistry, it was assumed that methane and air react to equilibrium products following an induction period. Hence, the analytical model does not consider the possible effect on non-equilibrium radical concentrations on the nitric oxide formation process. Measurements in the recirculation zone have shown that radical concentrations are significantly greater than equilibrium values. In studies in premixed, turbulent, methane-air flames (Ref. 38), radical concentrations in the flame zone were found to exceed equilibrium values. If radical concentrations in the flame are greater than equilibrium, then the actual nitric oxide formation rate will exceed that calculated using equilibrium radical concentrations. To bring predicted and measured exhaust nitric oxide concentrations into agreement would require O-atom concentrations more than an order of magnitude larger than equilibrium values. Such non-equilibrium O-atom concentrations are possible, but not likely, over the entire range of experimental conditions.

A second assumption incorporated in the analysis may contribute to underprediction of nitric oxide production in the turbulent flame. In the analysis, time-dependence of the flow properties was neglected. From the flow visualization studies, Section III-B, it is known that the downstream flame is characterized by turbulent fluctuations and eddies. The fluctuations in temperature, density, velocity and species concentrations about the time-mean values, particularly the temperature fluctuations, can result in an increased nitric oxide production rate. For the conditions of the present experiments, a temperature fluctuation of ±5% can increase the nitric oxide formation rate by approximately a factor of two.

SECTION VI

CONCLUSIONS

The experimental results obtained from the present investigation indicate that nitric oxide production in the recirculation zone downstream from the bluff-body flameholder depends on transport rates between the zone and the outer flow. These transport rates are strongly influenced by fluid dynamic phenomena, such as wake transition and vortex shedding (cold flow). It is essential that these fluid dynamic phenomena be considered in analytical models of nitric oxide formation in reacting flows with recirculation.

A stirred reactor model can adequately represent nitric oxide production in the recirculation zone downstream from the flameholder, providing non-equilibrium hydrocarbon chemistry is included in the model. A conventional eddy viscosity model, based on shear-generated turbulence, predicts flame angles which are in agreement with experimental observations. However, predicted nitric oxide concentrations in the burner exhaust, based on average local temperature, are substantially less than the measured values. The discrepany between predicted and measured nitric oxide production may be attributed to the neglect of non-equilibrium chemistry and turbulent fluctuations in the analytical model.

Volumetric nitric oxide production rates in the recirculation zone have been compared with overall volumetric nitric oxide production rates. For the present experimental configuration, nitric oxide production in the recirculation zone is not a major factor in the overall nitric oxide formation. This situation is the direct result of the relatively low temperature associated with the recirculation zone downstream from bluff-body flame stabilizers. It is expected that nitric oxide production in recirculation zones in practical combustion devices, such as furnaces and gas turbines, will be significant since the recirculation zone temperatures in these devices more nearly approach the adiabatic combustion temperature. The stirred reactor model for the recirculation zone indicates that an increase in temperature of approximately 100°K would increase the nitric oxide production rate by approximately a factor of five. Based on present results, the bluff-body flameholder appears to be an attractive method of flame stabilization from the standpoint of nitric oxide emissions.

Results from the present investigation point to the recirculation zone

as a major factor in nitric oxide production in practical combustion devices. The results indicate that combustor fluid dynamics strongly influence nitric oxide production rates in recirculation zones.

SECTION VII

REFERENCES

1. Niedzwiecki, R. W., and Jones, R. E., "Pollution Measurements of a Swirl-Can Combustor," NASA Technical Memorandum, TMX-68160, (1972).

2. Heap, M. P., Lowes, T. M., and Walmsley, R., "The Emissions of Nitric Oxide from Large Turbulent Diffusion Flames," Fourteenth Symposium (International) on Combustion (in press).

   Heap, M. P., Lowes, T. M., and Walmsley, R., "The Effect of Burner Parameters on Nitric Oxide Formation in Natural Gas and Pulverized Fuel Flames," paper presented at First American Flame Days, Chicago, Illinois, (1972).

3. Shoffstall, D. R., and Larson, D. H., "Aerodynamic Influences on Combustion and Pollution Emissions," paper presented at the Spring Meeting of the Combustion Institute, Central States Section, Champaign, Illinois, (1973).

4. Markovin, M. V., "Flow Around Circular Cylinder - A Kaleidoscope of Challenging Fluid Phenomena," Proceedings of the Symposium on Fully Separated Flows, AMSE, New York, p. 102 (1964).

5. Roshko A. and Fiszdon, W., "On the Persistance of Transition in the Near-Wake," Problems of Hydrodynamics and Continuum Mechanics, Soc. Ind. Appl. Math, Philadelphia , p. 606 (1967).

6. Bloor, M. S., "The Transition to Turbulence in the Wake of a Circular Cylinder," J. Fluid Mechanics, 19, p. 290 (1964).

7. Williams, G. C. Hottel, H. C. and Scurlock, A. C., "Flame Stabilization and Propagation in High Velocity Gas Streams," Third Symposium on Combustion, Flame and Explosion Phenomena, The Williams and Wilkins Co., Baltimore, p. 21 (1949).

8. Shigemitsu, Y., "Statistical Theory of Turbulence," Aerophysics Department, Mississippi State University, Research Report No. 64, (1966).

9. Abramovich, G. N., "The Theory of Turbulent Jets," M.I.T. Press, Cambridge, Mass. (1963).

10. Schlichting, H., "Boundary Layer Theory," McGraw-Hill Book Company, Inc., Fourth Edition, (1960).

11. Winterfeld, G., "On Processes of Turbulent Exchange Behind Flame Holders," Tenth Symposium (International) on Combustion, The Combustion Institute, Pittsburgh, p. 1265 (1965).

12. Zukoski, E. E. and Marble F. E., "The Role of Wake Transition in the Process of Flame Stabilization on Bluff Bodies," Combustion Researches and Reviews (Butterworth, London) p. 167 (1955).

13. Wright, F. H., "Bluff-Body Flame Stabilization: Blockage Effects," Combustion and Flame 3, p. 319 (1959).

14. Pein, R., Peschel, H., and Fetting F., "Recirculation Zone Concentrations and Temperatures of Bluff-Body Stabilized Turbulent Flames, Combustion Science and Technology 1, p. 327 (1970).

15. Gaydon, A. G. and Wolfhard, H. G., "Flames: Their Structure, Radiation and Temperature," Chapman and Hall, London, p. 234 (1960).

16. Bovina, T. A., "Studies of Exchange Between Re-circulation Zone Behind the Flameholder and Outer Flow," Seventh Symposium (International) on Combustion, Butterworth, London, p. 692 (1959).

17. Bowman, C. T., "Investigation of Nitric Oxide Formation Kinetics in Combustion Processes: The Hydrogen-Oxygen-Nitrogen Reaction," Combustion Science and Technology 3, p. 37 (1971).

18. Newhall, H. K., and Shahed, S. M., "Kinetics of Nitric Oxide Formation in High-Pressure Flames," Thirteenth Symposium (International) on Combustion, The Combustion Institute, Pittsburgh, p. 381 (1971).

19. Bowman, C. T., and Seery D. J., "Investigation of Nitric Oxide Formation Kinetics in Combustion Processes: The Methane-Oxygen-Nitrogen Reaction," Emissions from Continuous Combustion Systems, Plenum, New York p. 123 (1972).

20. Meinel, H., and Just, Th., "A New Analytical Technique for Continuous NO Detection in the Range from 0.1 to 5000 ppm," paper presented at the 41st Meeting of the AGARD Propulsion and Energetics Panel, London, (1973).

21. Baines, W. D. and Peterson, E. G., "An Investigation of Flow Through Screens," Transactions of the ASME, p. 467 (1951).

22. Glasstone, S., "Textbook of Physical Chemistry," Second Edition, D. Van Nostrand Company, Inc., Princeton, New Jersey, (1946).

23. Longwell, J. P., Frost, E. E. and Weiss, M. A., "Flame Stability in Bluff Body Recirculation Zones," Ind. Eng. Chem. 45, p. 1629 (1953).

24. Jones, A., and Prothero, A., "The Solution of the Steady-State Equations for an Adiabatic Stirred Reactor," Combustion and Flame, 12, p. 457 (1968).

25. Zeldovich, Ya. B., Sadovinkov, P. Ya., and Frank-Kamenetskii, D. A., "Oxidation of Nitrogen in Combustion," Academy of Sciences of USSR, Institute of Chemical Physics, Moscow-Leningrad (trans. by M. Shelef), (1947).

26. Heywood, J. B., "Gas Turbine Combustor Modeling for Calculating Nitric Oxide Emissions," paper presented at AIAA/SAE 7th Propulsion Joint Specialist Conference, Salt Lake City, Utah, (1971).

27. Baulch, D. L., Drysdale, D. D., and Lloyd, A. C., "Critical Evaluation of Rate Data for Homogeneous Gas-Phase Reactions of Interest in High-Temperature Systems," Department of Physical Chemistry, Report No. 4, Leeds, England, (1969).

28. Schott, G. L., "Kinetics Studies of Hydroxyl Radicals in Shock Waves. III. The OH Concentration Maximum in the Hydrogen-Oxygen Reaction," J. of Chemical Physics, 32, p. 710 (1960).

29. Milne, T. A. and Greene, F. T., "Mass-Spectrometric Studies of Reactions in Flames. II. Quantitative Sampling of Free Radicals from One-Atmosphere Flames," J. of Chemical Physics, 44, p. 2444 (1966).

30. Engleman, V. S., Edelman, R. B., Bartok, W., and Longwell, J. P., "Experimental and Theoretical Studies of NO_x Formation in a Jet-Stirred Combustor, Fourteenth Symposium (International) on Combustion (in press).

31. Cohen, L. S., "An Analytical Study of the Mixing and Nonequilibrium Chemical Reaction of Ducted Compressible Streams," Paper No. 66-617, AIAA Second Propulsion Joint Specialist Conference, Colorado Springs, Colo. (1966).

32. Vasiliu, J., "Turbulent Mixing of a Rocket Exhaust with a Supersonic Stream Including Chemical Reaction," J. Aerospace Sciences, 29, p. 19 (1962).

33. Cohen, L. S., "A Kinematic Eddy Viscosity Model Including the Influence of Density Variations and Preturbulence," Langley Conference on Free Turbulent Shear Flows, Langley, Va. (1972).

34. Seery, D. J., and Bowman, C. T., "An Experimental and Analytical Study of Methane Oxydation Behind Shock Waves," Combustion and Flame, 14, p. 37 (1970).

35. JANAF Tables of Thermochemical Data, Dow Chemical Co., Midland, Mich. (1964).

36. Pratt, D. T., and Malte, P. C., "Formation of Thermal and Prompt NO_x in a Jet-Stirred Combustor," paper 34b presented at the 75th National A.I.Ch.E. Meeting, Detroit, Michigan, (1973).

37. Forthmann, E., "Uber Turbulent Strahlansbreitung," Ingen.-Arch., 5, p. 42 (1934).

38. Thompson, D., Brown, T. D., and Beér, J. M., "NO_x Formation in Combustion," Combustion and Flame, 19, p. 69 (1972).

39. Zabielski, M. F., and McHugh, T.M., "Resolution Enhancement by Iterative and Fourier Techniques," paper presented at the 21st Annual Conference on Mass Spectrometry and Allied Topics, San Francisco, Calif., (1973).

40. Penner, S. S., "Quantitative Molecular Spectroscopy and Gas Emissivities," Addison-Wesley, Reading, Mass., p. 69 (1959).

41. Kiser, R. W., "Introduction to Mass Spectrometry and its Applications," Prentice Hall, Englewood Cliffs, New Jersey, p. 218 (1965).

42. Roboz, J., "Introduction to Mass Spectrometry: Instrumentation and Techniques," Interscience, New York, p. 314 (1968).

SECTION VIII

NOMENCLATURE

A	Pre-exponential factor
A_w	Recirculation zone surface area, cm^2
a	Absorption coefficient
B_M	Recirculation zone maximum width
B_R	Blockage ratio, D/h
b	Screen wire diameter, cm
b_j	Total number of atoms of species j present
C_i	Concentration of species i, moles/cc
c, c_1	Constants
D	Cylindrical bluff-body diameter, cm
d	Spacing between fiber optic probe units, cm
E	Activation energy, cal
F	Total free energy, kcal
f_i	Fugacity of species i, atm
G	Mass flux, gm/cm^2-sec
H	Specific enthalpy, kcal/mole
h	Test section height, cm
I	Intensity
K_j	Equilibrium constant of reaction j

k_j	Rate constant of reaction j
L	Recirculation zone length, cm
M_i	Molecular weight of species i, gm/mole
$\dot{m}$	Mass flow rate, gm/sec
m_i	Mass fraction of species i, gm i/gm mixtures
N	Total number of moles of species present, mole
$\dot{n}_i$	Molar flow rate of species i, mole i/sec
n	Total number of species
P	Pressure, atm
p	Partial pressure, atm
q	Number of different atoms present
R	Universal gas constant
R_j	Rate of reaction j
Re	Reynolds number
r	Denotes closure point
S	Screen mesh spacing, cm
S_i	Species i
Sh	Strouhal number
s	Denotes separation point
T	Temperature, $^{\circ}K$
U	Specific velocity designation, m/sec
u	Axial velocity, m/sec

u'	Fluctuating transverse velocity, m/sec
V	Volume, cc
v	Transverse velocity, m/sec
v'	Fluctuating transverse velocity, m/sec
w	Width of test section, cm
x	Axial distance from bluff-body, cm
y_i	Mole fraction of species i, mole i/mole mixture
z	Transverse distance, cm

Greek

α	Flame angle, deg
β	Defined as $D/(Gh)^2$
δ	Exponent for two-dimensional ($\delta = 0$) or axisymmetric ($\delta = 1$) flow
ϵ	Eddy viscosity, gm/cm-sec
η	Nondimensional transverse coordinate
θ	Slope of tracer concentration distribution
λ	Wavelength, $\mathring{A}$
μ_i	Partial molal Gibbs free energy of species i, kcal/mole
ν_{ij}	Stoichiometric coefficient for species i in chemical reaction j
ρ	Density, kg/m^3
σ_i	Specific molar concentration of species i, mole i/gm-i
τ	Time, sec

$\Delta\tau$	Dwell time, sec
τ_t	Residence time, sec
ϕ	Equivalence ratio $(\dot{m}_f/\dot{m}_a)/(\dot{m}_f/\dot{m}_a)_{stoichiometric}$
Ψ	Stream function
ξ	Nondimensional axial coordinate
ω	Exponent in rate equation or wavenumber, cm^{-1}

Subscripts

a	Air
f	Fuel
ID	Ignition delay
m	Mean value
max	Maximum value
NO	Nitric Oxide
o	Initial
t	Tracer
tot	Total
v	Vortex shedding
w	Recirculation zone
∞	Free stream

Other

$(\hat{\ })$	Reference quantity
$(\overline{\ })$	Average quantity

SECTION IX

APPENDICES

		Page
A.	Experimental Techniques in the Combustion Experiments	113
B.	Fiber Optic Measurement Techniques in the Cold Flow Experiments	129

APPENDIX A

EXPERIMENTAL TECHNIQUES IN THE COMBUSTION EXPERIMENTS

A.1 Flow Visualization Techniques

The flow visualization measurements, discussed in Section III-B, were made using the schlieren optical system shown in Fig. A-1. The light source used for the spark schlieren measurements was an air-gap spark with a 3-μsec duration. The knife-edge, used in conventional schlieren systems, was replaced in the present experiments by a 0.16-cm diameter circular aperture (pinhole). Use of the circular aperture permits measurement of refractive index gradients in both transverse and axial directions and facilitates determination of the recirculation zone boundary. The light source used for the time-exposure schlieren measurements was a 200 watt Hg-Xe dc arc lamp (Hanovia 901-B1). The schlieren photographs were recorded on 4" x 5" Polaroid 3000 film.

A.2 Modified Sodium Line Reversal Technique

The optical system used to make measurements of temperature and residence time in the recirculation zone is shown in Fig. A-2. Light from a tungsten filament lamp passes through the burner test section and enters a monochromator (McPherson Model 235) set on the 5890 Å sodium D-line. The intensity of the lamp and sodium emission from the flame at 5890Å is monitored by a photomultiplier (EMI 9558 BQ). The signal from the photomultiplier is fed to the y-axis amplifier of an x-y plotter (Houston Series 2000). The lamp current, and hence the brightness of the lamp, can be automatically ramped from zero to a maximum value, corresponding to a lamp brightness temperature of approximately 2400°K. A signal, proportional to lamp current, is fed to the x-axis amplifier of the x-y plotter. The optical system is calibrated to give the lamp brightness temperature as a function of x-axis voltage by manually ramping the lamp current and measuring the brightness temperature of the filament using an optical pyrometer. To minimize errors resulting from losses in the focusing optics and test section windows, the calibration is carried out using essentially the same optics as are used to make temperature measurements, Fig. A-2. The brightness temperature of the lamp at 5890Å is determined from the calibration carried out at 6550Å, using the correction factors in Ref. 15.

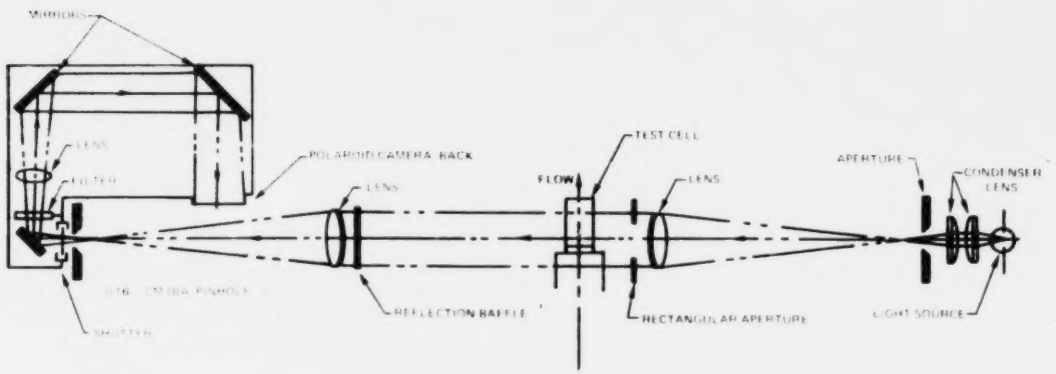

FIG. A1 SCHEMATIC DIAGRAM OF THE SCHLIEREN OPTICAL SYSTEM.

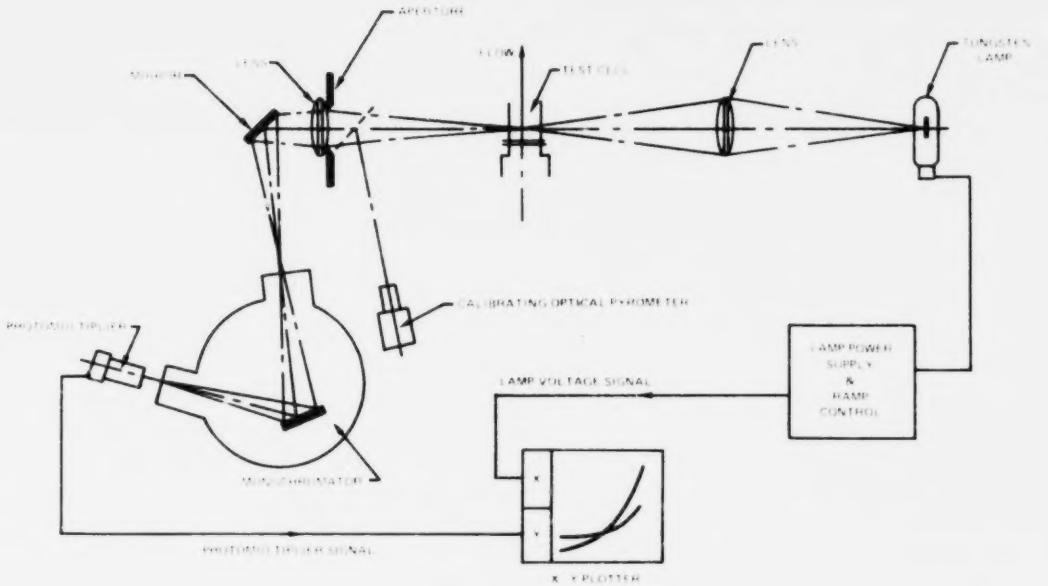

FIG. A2 SCHEMATIC DIAGRAM OF THE SODIUM D-LINE PHOTOMETER.

A.2.1 Experimental Procedure for Temperature Measurements - With no flow in the test section, the lamp current was manually set to its maximum value, and the brightness temperature of the filament was measured using the optical pyrometer. This measurement served to confirm the validity of the temperature-lamp current calibration. The lamp was ramped automatically to zero current, and the corresponding intensity (y-axis) -- brightness temperature (x-axis) curve was traced out by the x-y plotter, Fig. A-3. The lamp current was reset manually to its maximum value, and combustion was initiated in the burner. After steady-state conditions were established in the burner, sodium tracer was continuously injected into the recirculation zone. With the lamp set at its maximum brightness temperature ($\sim 2400^{\circ}K$), injection of sodium tracer results in a decrease in the lamp intensity, as observed by the photomultiplier, due to absorption of lamp radiation by sodium in the flame. The lamp was ramped automatically to zero current, and the corresponding intensity-brightness temperature curve was traced out by the x-y plotter, Fig. A-3. At the zero lamp current, the observed intensity, with sodium tracer, is the sodium D-line emission. The point where the curve with combustion intersects the curve with no combustion is the reversal point, and the flame temperature may be determined directly from the x-coordinate of the intersection. Following completion of the combustion run, the intensity-brightness temperature curve was determined again, with no flow, to verify the lamp calibration.

To assess the validity of the optical temperature measurement technique, temperatures measured near the flame zone in premixed methane-air flames on a Meker-type burner using the sodium-line reversal technique, were compared with temperatures measured using small, coated Pt/Pt-Rh thermocouples. The temperatures measured using the two techniques, after a suitable radiation correction was applied to the thermocouple measurements, were the same within experimental uncertainty ($\pm 25^{\circ}C$).

A.2.2 Experimental Procedure for Residence Time Measurements - Residence times of gas in the recirculation zone were determined by measuring the decay of injected tracer, following rapid shut-off of the tracer supply. The tracer material used in the present combustion experiments was sodium. In these experiments, a water/sodium chloride solution was injected into the recirculation zone through the rear of the flameholder. This injecting flameholder consisted of two concentric stainless-steel tubes, each having a series of small holes drilled through the wall facing in the downstream direction. A water/sodium chloride solution flowed through the inner tube

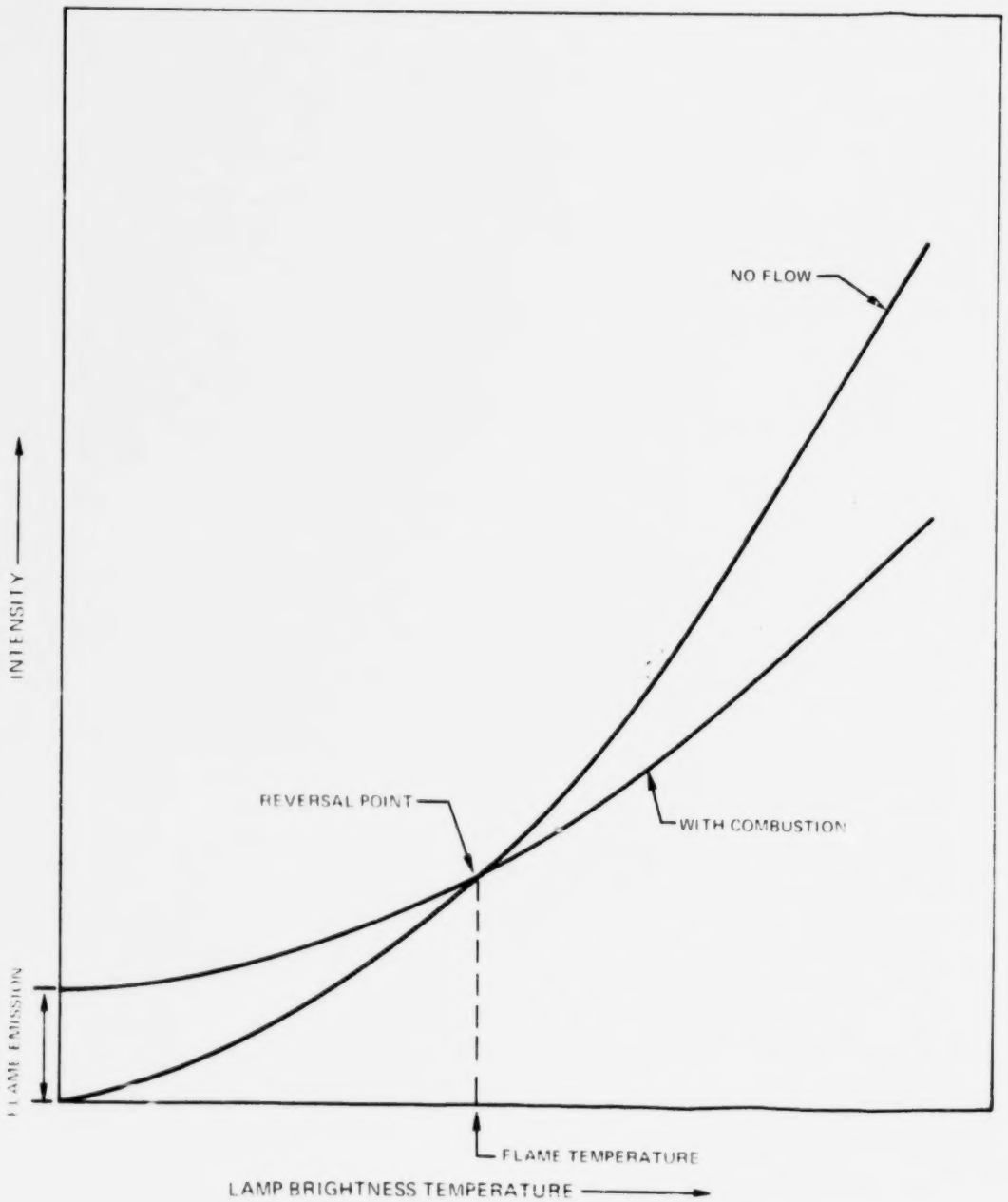

FIG. A.3 **TYPICAL EXPERIMENTAL TRACES OBTAINED FROM THE TEMPERATURE MEASUREMENT EXPERIMENTS.**

at all times. If the holes in the two tubes were aligned, by sliding the inner tube along its axis, a small amount of the water/sodium chloride solution could flow into the recirculation zone. If the inner tube was again moved along its axis, so that the holes were no longer aligned, the tracer solution flow into the recirculation zone stopped. The injecting flameholder was set to the open position by a solenoid-actuator, Fig. 4 , pulling against a pre-loaded spring. When the solenoid was de-energized, the pre-loaded spring rapidly moved the inner tube, shutting off the tracer supply. The calculated closing time of the injecting flameholder was 1.5 msec.

The optical system used to make the residence time measurements was essentially the same as was used for the temperature measurements. However, in the residence time experiments, the photomultiplier output was displayed on an oscilloscope (Tektronix 545B). The oscilloscope sweep was triggered on the closing of the solenoid-actuator. The 10-90% risetime of the photomultiplier/oscilloscope combination was approximately 10 μ sec.

Prior to an experiment, the tungsten filament lamp current was set to its maximum value. After steady-state combustion was established in the burner, the solenoid-actuator was energized, thereby turning on the tracer flow. After steady tracer flow was established, as evidenced by a relatively constant absorption of the tungsten lamp emission by the sodium in the recirculation zone, the solenoid-actuator was de-energized shutting off the tracer flow and triggering the oscilloscope. The resulting absorption decay curve was displayed on the oscilloscope and recorded on Polaroid film. A typical experimental trace is shown in Fig. A-4. As the tracer concentration in the recirculation zone decreased, the observed absorption of the tungsten lamp emission decreased. The absorption data, Fig. A-4, can be plotted on semi-logarithmic paper, Fig. A-5. Following an initial period (~ 1 msec) associated with the shutting off of tracer supply, the observed absorption decays nearly exponentially in time, with a characteristic time constant of 8.9 msec. In the residence time experiments, the maximum abosrption by the tracer material (at $\tau = 0$) was approximately 5% of the incident lamp intensity. For these low levels of absorption, the absorptivity is directly proportional to the tracer concentration, and the characteristic time constant of the absorption decay curve, Fig. A-5, may be equated to the mean residence time. In the temperature measurement experiments, injection of the tracer solution into the recirculation zone reduced the temperature by approximately 75°K. This relatively small reduction in recirculation zone temperature (less than 5%)

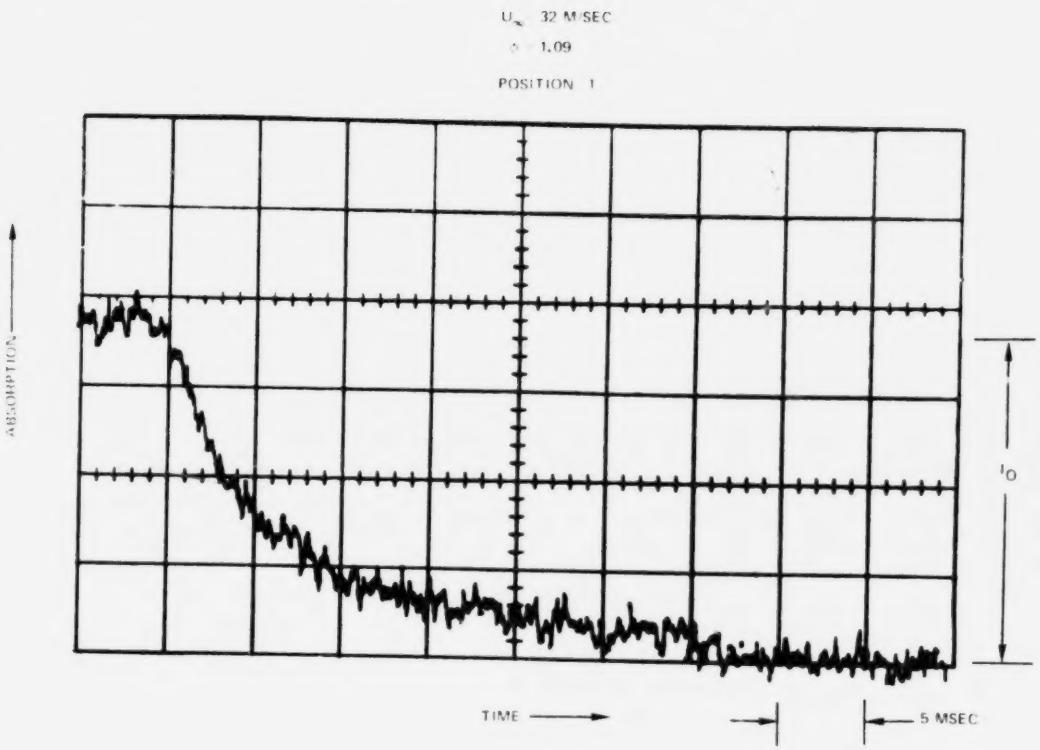

FIG A 4 TYPICAL OSCILLOSCOPE TRACE FROM RESIDENCE TIME EXPERIMENTS

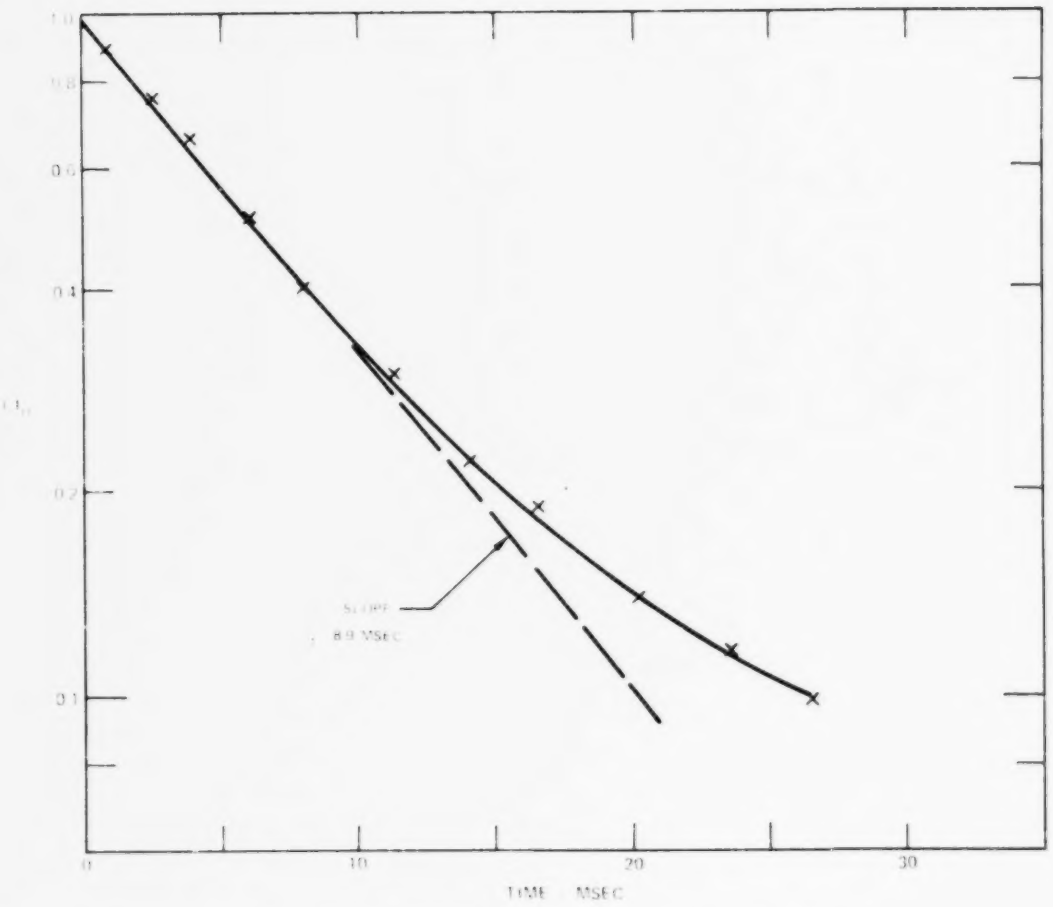

FIG. A5 TYPICAL SEMI-LOGARITHMIC PLOT OF ABSORPTION DECAY CURVE

suggests that the tracer flow is sufficiently small so as not to significantly perturb the flow pattern in the recirculation zone. Hence, it is reasonable to assume that tracer injection does not have a significant effect on the mass exchange rate.

A.3 Ultraviolet Absorption Technique

The concentration of OH and NO in the recirculation zone was measured using an ultraviolet absorption technique. A schematic diagram of the optical system used to make these concentration measurements is shown in Fig. A-6. Radiation from a 1000-watt, Hg-Xe dc arc lamp (Hanovia 528 B-1) passes through a beam splitter, a 13.8 cps chopping disc and is focused in the center of the combustor test section. A spherical mirror, located on the opposite side of the test section, reflects the beam back through the test section. The return beam passes through the chopper and is reflected by the beam splitter into a lens which focuses the beam on the entrance slit of a grating monochromator (McPherson Model 235). The light intensity at a specified wavelength is monitored by a photomultiplier (EMI 9558 BQ). The output signal from the photomultiplier passes through a phase-sensitive amplifier, synchronized to the chopping frequency. The dc output of the phase-sensitive amplifier, which is proportional to light intensity, is displayed on a chart recorder (Hewlett-Packard 7100B). Use of the two-path optical system, coupled with phase-sensitive detection, greatly enhances the ability to measure small absorption signals, and hence small concentrations of absorbing species.

A.3.1 OH Concentration Measurements - The mean OH concentration at a single location in the recirculation zone (position 1) was determined by measuring the absorption of ultraviolet radiation by the $\Sigma - \pi(0,0)$ band of the molecule at 3080Å. In a previous experimental investigation (Refs. 17 and 19) the optical system was calibrated to permit measurement of OH concentration.

A.3.2 Nitric Oxide Concentration Measurements -- Recirculation Zone - The mean nitric oxide concentration at several locations in the recirculation zone was determined by measuring the absorption of ultraviolet radiation by the $\gamma(0,0)$-band of the molecule. A similar optical technique has been used to measure nitric oxide concentrations in several recent investigations of pollutant formation in combustion processes (Refs. 17-20). In the present investigation, the optical system was calibrated by flowing known

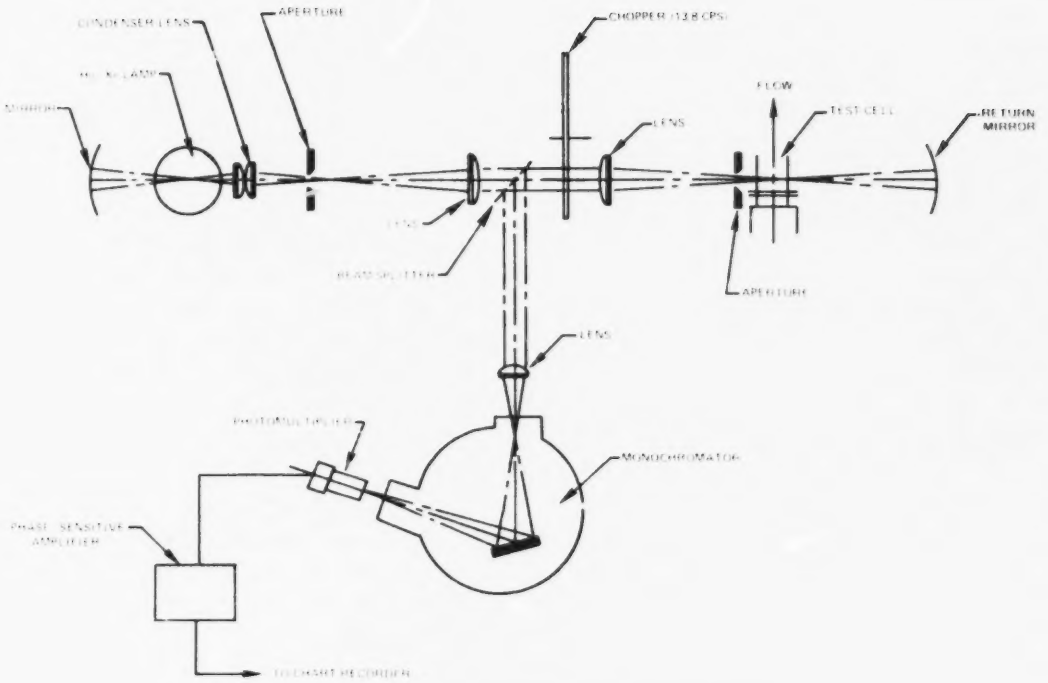

FIG. A-6 SCHEMATIC DIAGRAM OF THE UV PHOTOMETER.

mixtures of NO (CP Grade) and N_2 through the test section, scanning the monochromator over the wavelength range 2200-2300Å and measuring the absorption by the $\gamma(0,0)$ band near 2260Å. In these calibration runs the nitric oxide mole fraction in the gas stream was varied from 5.0×10^{-3} to 8.0×10^{-5}. A typical absorption spectrum, obtained from the calibration experiments, is shown in Fig. A-7. In this spectrum, the rotational structure and the sharply-defined band heads have been smeared by the slit function of the monochromator. The observed absorption spectrum was processed using a recently-developed analytical technique (Ref. 39), to remove some of the effects of slit-broadening. Using the processed (de-convolved) absorption spectrum, shown in Fig. A-7, an average absorption coefficient for the $\gamma(0,0)$ band was defined by

$$\bar{a} = \frac{1}{C_{NO}^{v=0}\,\ell}\left[\ell n\left(\frac{1}{\Delta\omega}\int_{\Delta\omega}\frac{I\omega}{I_\omega^o}\,d\omega\right)\right] \qquad \text{(A-1)}$$

where $\bar{a}$ = average absorption coefficient (cm^2/mole), $C_{NO}^{v=0}$ = nitric oxide concentration in the ground vibrational state (mole/cm^3), ℓ = 2 x test section width (cm), $\Delta\omega$ = width of the absorption band (cm^{-1}) and $I\omega/I_\omega^o$ = transmissivity at wave number ω. There are two major uncertainties in the optical system calibration. The first uncertainty is introduced by imprecise determination of the extent of the absorption band, $\Delta\omega$, (Ref. 40). At low nitric oxide concentrations, the short-wavelength tail of the absorption band, Fig. A-7, cannot be accurately distinguished from system noise. To reduce uncertainties associated with imprecise determination of $\Delta\omega$, the average transmissivity, Eq. A-1, was calculated for a bandwidth corresponding to 10% of the maximum absorptivity. Using this arbitrary definition for $\Delta\omega$, room temperature values of the average absorption coefficient were obtained which were essentially constant for the range of nitric oxide concentrations in the calibration experiments. The second major uncertainty in the optical system calibration is associated with extrapolation of the room temperature values of average absorption coefficient to the temperature range of the combustion experiments -- 1600 to 2000°K. The high temperatures and low densities associated with the recirculation zone in the combustion experiments produce changes in collisional and Doppler broadening of the rotational lines in the $\gamma(0,0)$ band. However, for the present experimental conditions, collisional and Doppler broadening of the $\gamma(0,0)$-band are not significant compared with instrument broadening. Hence, variations in the average absorption coefficient with temperature are neglected. At

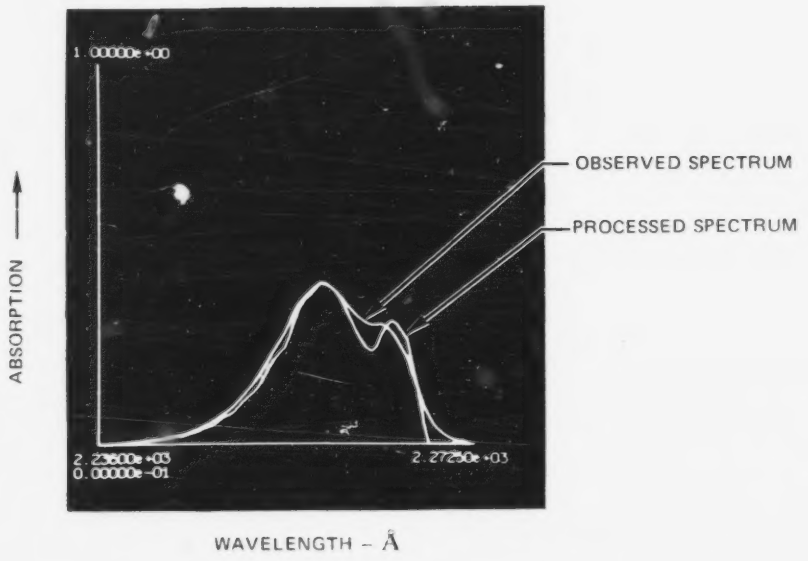

FIG. A-7 TYPICAL NITRIC OXIDE ABSORPTION SPECTRUM – NITRIC OXIDE MOLE FRACTION = 2×10^{-3}

elevated temperatures only a fraction of the nitric oxide molecules are in the ground vibrational state. To calculate the total nitric oxide concentration from the measured ground-state concentration, the nitric oxide was assumed to be in thermal equilibrium at the measured recirculation zone temperature.

A.4 Exhaust Concentration Measurement Technique

The concentration distributions of nitric oxide, methane, oxygen, carbon dioxide and carbon monoxide in the exhaust gas from the combustion test section were determined using a traversing sampling probe coupled to an on-line time-of-flight mass spectrometer. A schematic diagram of the sampling system and associated data processing equipment is shown in Fig. A-8. The water-cooled, stainless-steel sampling probe rapidly quenches the gas sample by an aerodynamic expansion across a choked 0.015-cm diameter orifice. A photograph of the sampling probe in the combustor exhaust is shown in Fig. A-9. The quenched gas sample passes through a heated, stainless-steel sample line to the inlet valve of the mass spectrometer. The sample line wall was held at a constant temperature of 125°C, and the sample line pressure was maintained at 3.00 ±0.05 torr. The time-of-flight mass spectrometer, used in the present investigation, is a portable, high-resolution instrument (United Aircraft Research Laboratories TOF-40). The output signal of the mass spectrometer is processed by a waveform eductor (Princeton Applied Research TDH-9) to enhance signal-to-noise ratio. The waveform eductor stores the processed mass spectra, which may then be displayed on a chart recorder (Hewlett-Packard 7100B) following completion of the experiment.

Prior to making exhaust concentration measurements, the probe sampling system and mass spectrometer were calibrated. This calibration was carried out by flowing known mixtures of methane, carbon dioxide, carbon monoxide, oxygen, nitric oxide and nitrogen through the test section and measuring the mass spectra of the gas at the test section exit. From the known mixture composition and the observed mass spectra, mass discrimination effects in the sampling system and the fragmentation patterns for various species of interest were determined. Mass discrimination effects and fragmentation patterns are required if a unique determination of exhaust gas composition is to be obtained from the measured mass spectra.

Although the mass spectrometer, used in the experimental study, is a high-resolution instrument, nitric oxide concentrations in the exhaust gas were

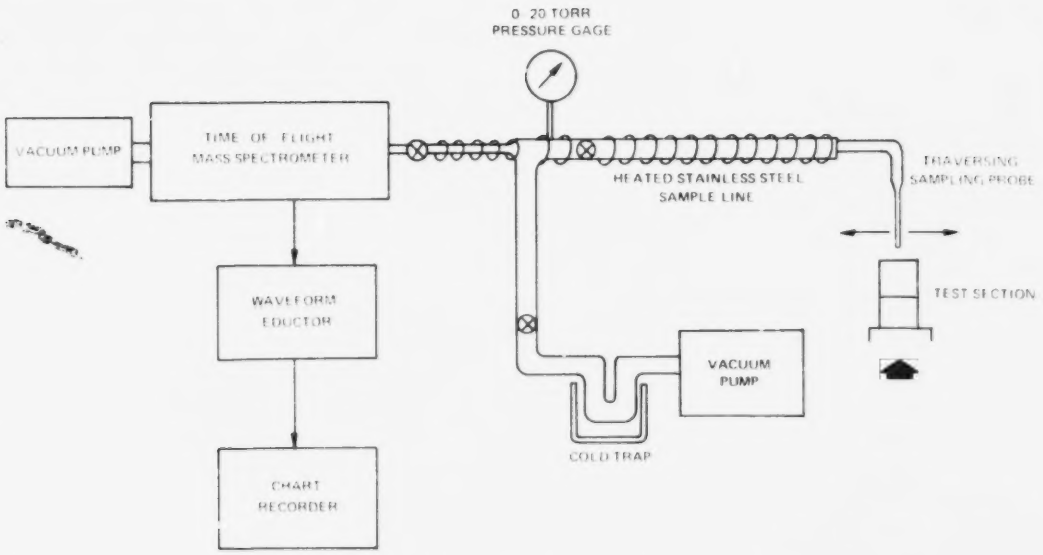

FIG. A.8 SCHEMATIC DIAGRAM OF PROBE AND SAMPLING SYSTEM USED FOR EXHAUST CONCENTRATION MEASUREMENTS.

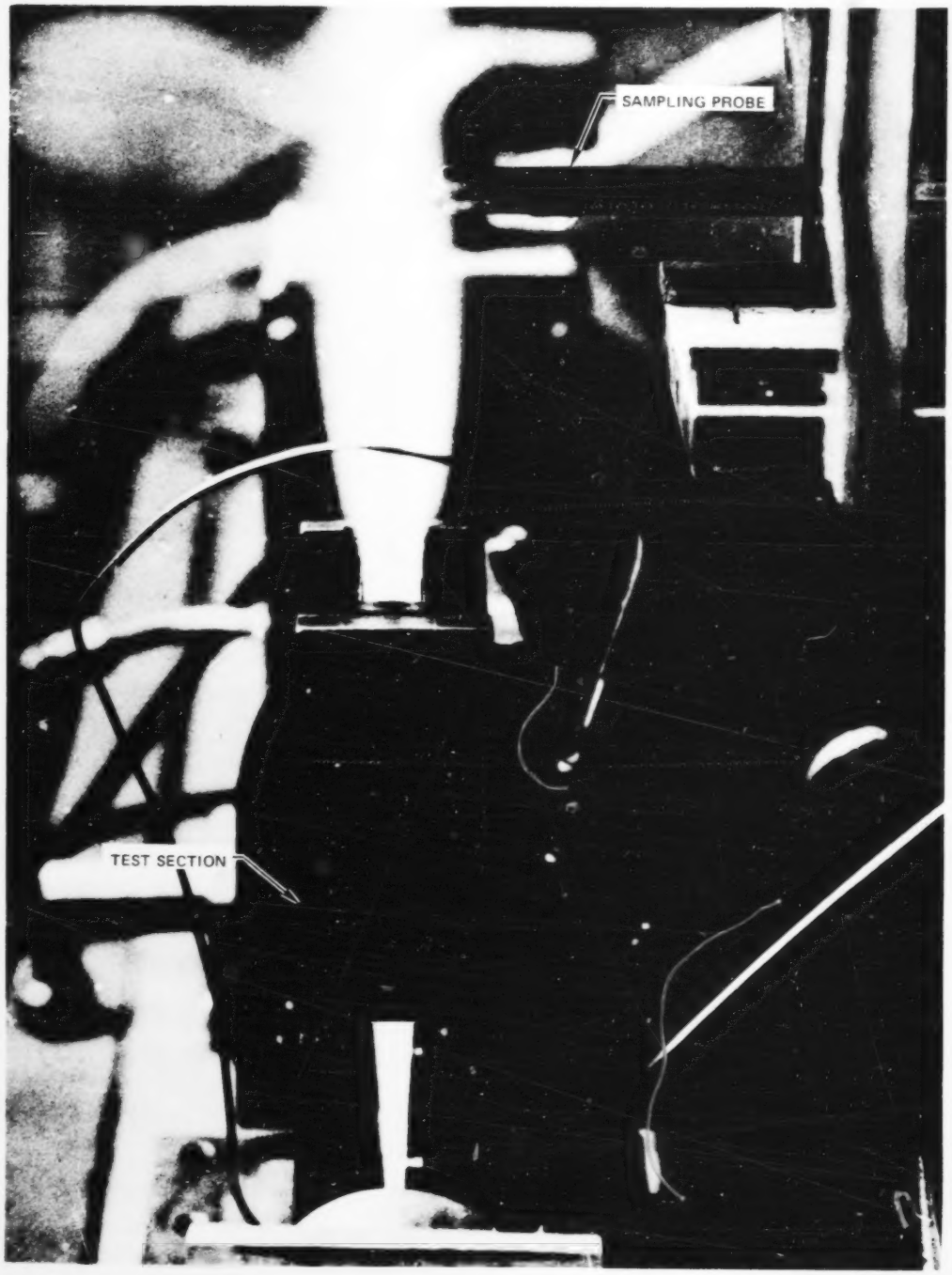

FIG. A-9 SAMPLING PROBE IN COMBUSTOR EXHAUST

sufficiently small so that the primary nitric oxide mass peak (m/e = 30) was overlapped to a certain extent by the m/e = 29 isotope of molecular nitrogen, Fig. A-10a. To improve the effective resolution of the mass spectrometer for nitric oxide, the mass spectra in the range m/e = 28-30 were processed using the analytical deconvolution technique previously discussed. The processed (de-convolved) spectra are shown in Fig. A-10b.

In the combustion experiments, the mass spectra of the exhaust gas was determined in the range m/e = 12-44. Many of the observed mass peaks in this range are not unique to a single species -- for example, m/e = 16 has components due to methane, oxygen, carbon dioxide, carbon monoxide and water. Hence to determine a unique exhaust gas composition, the observed mass spectra must be processed to account for overlapping mass peaks. To facilitate data processing a computer program was developed which uses standard analytical techniques (Refs. 41 and 42) to extract a unique composition from the observed mass spectra.

The principal mass peak for nitric oxide is m/e = 30. Of the major species present in the exhaust, only nitrogen and carbon monoxide make significant contributions to the observed m/e = 30 peak (due to the N_2^{15} and $C^{12}O^{18}$ isotopes). Minor species which would contribute to the m/e = 30 peak, if present in the exhaust, include formaldehyde (H_2CO) and ethane (C_2H_6). The observed mass spectra show that the concentrations of ethane and formaldehyde in the exhaust gas are below the detection threshold (~ 20 ppm (v)). Hence only contribution of nitrogen and carbon monoxide to the m/e = 30 peak must be accounted for. The carbon monoxide concentration in the exhaust was estimated from the measured methane and carbon dioxide concentrations through a carbon balance. The carbon monoxide mole fractions, inferred in this manner, ranged from 0 to 0.02. The correction on the m/e = 30 peak for contributions from isotopic nitrogen and carbon monoxide were in the range of 10-25 ppm (v).

To ascertain if nitric oxide is reduced to N_2 in the stainless-steel exhaust probe and sampling line in the presence of fuel, known mixtures of nitric oxide and methane were sampled. Negligible depletion of nitric oxide in these samples was observed.

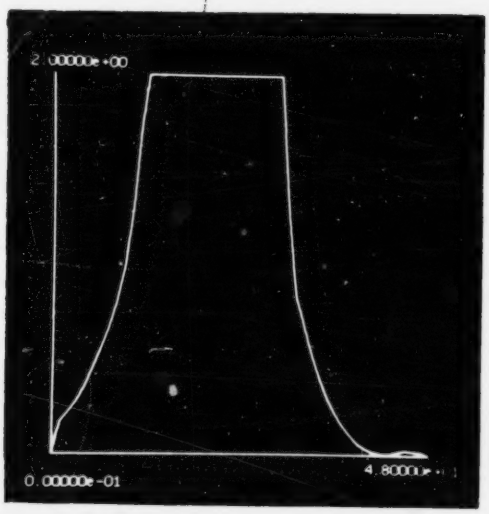

FIG. A-10a

TYPICAL OBSERVED MASS SPECTRA OF THE COMBUSTOR EXHAUST IN THE RANGE m/e = 28--30.

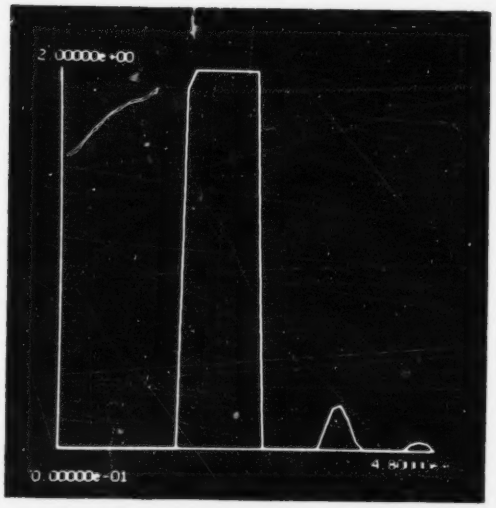

FIG. A-10b

m/e 28 29 30

TYPICAL DECONVOLVED MASS SPECTRA.

APPENDIX B

FIBER OPTIC MEASUREMENT TECHNIQUES IN THE COLD FLOW EXPERIMENTS

The fiber optic probe system (Fig. B-1) consists of: (1) a fiber optic probe, (2) an optical photometer system. and (3) data acquisition and display electronics. High intensity light for the fiber optic probe system is made available from a tungsten-halogen projection lamp powered by a regulated dc power supply (Kepco model JQE-15-12(M)). The light output from the lamp is directed to a narrow band pass optical filter (Baird-Atomic 460 B9/450 B5) which passes light in the range 4550-4690 Å, a wavelength range near optimum for absorption by the NO_2-N_2O_4 tracer material. The filtered light is channeled into the test chamber via the transmitter unit of the fiber optic probe. Subsequently, a fraction of the light is absorbed by the tracer material and the remainder is channeled through the detector unit of the probe to a photomultiplier tube (RCA 6199) powered by a high voltage dc power supply (Fluke model 412B); photomultiplier tube operation typically is at 750 volts.

Photomultiplier system output is displayed simultaneously on a Hewlett Packard digital volt meter and a cathode oscilloscope (Tektronix 531A). Oscilloscope traces are recorded photographically using a Polaroid camera.

The optical efficiency of each component in the optical photometer system as a function of wavelength is given in Fig. B-2. The total system response of approximately 10 percent of the input light intensity was obtained by multiplying all component efficiencies at each wavelength.

The light absorption by the tracer material is a function of the absorption coefficient, a, the tracer concentration, y_t, and the spacing between the transmitter and detector units of the fiber optic probe, d, according to the Beer-Lambert law (Ref. 22):

$$I/I_o = \exp(-q \cdot d \cdot y_t) \qquad \text{(B-1)}$$

An increase in any of the three parameters contained in Eq. (B-1) will result in increased absorption; however, only the absorption coefficient varies with wavelength.

The tracer material used for the optical investigations consisted of an equilibrium mixture of NO_2 and N_2O_4. According to Ref. 43, absorption above 4000 Å is due exclusively to the concentration level of NO_2. Hence, increasing the amount of NO_2 in the tracer mixture by raising the temperature to shift the equilibrium to favor NO_2 production results in increased absorption. The equilibrium composition of NO_2-N_2O_4 mixtures is given in Fig.B-3a as a function of temperature. In order to establish satisfactory absorption levels for the current experiments, it was necessary to operate at elevated temperatures, see Fig.B-3b.

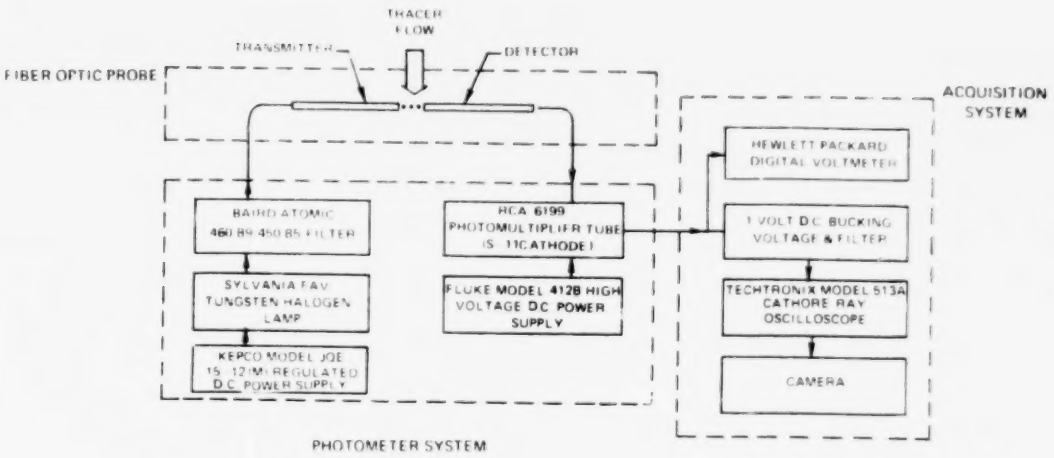
TRACER FLOW
TRANSMITTER
DETECTOR
FIBER OPTIC PROBE
ACQUISITION SYSTEM
HEWLETT PACKARD DIGITAL VOLTMETER
BAIRD ATOMIC 460 89 450 85 FILTER
RCA 6199 PHOTOMULTIPLIER TUBE (S-11 CATHODE)
1 VOLT D.C. BUCKING VOLTAGE & FILTER
SYLVANIA FAV TUNGSTEN HALOGEN LAMP
FLUKE MODEL 412B HIGH VOLTAGE D.C. POWER SUPPLY
TECHTRONIX MODEL 513A CATHODE RAY OSCILLOSCOPE
KEPCO MODEL JQE 15-12M REGULATED D.C. POWER SUPPLY
CAMERA
PHOTOMETER SYSTEM

FIG. 8.1 SCHEMATIC DIAGRAM OF FIBER OPTIC INSTRUMENTATION

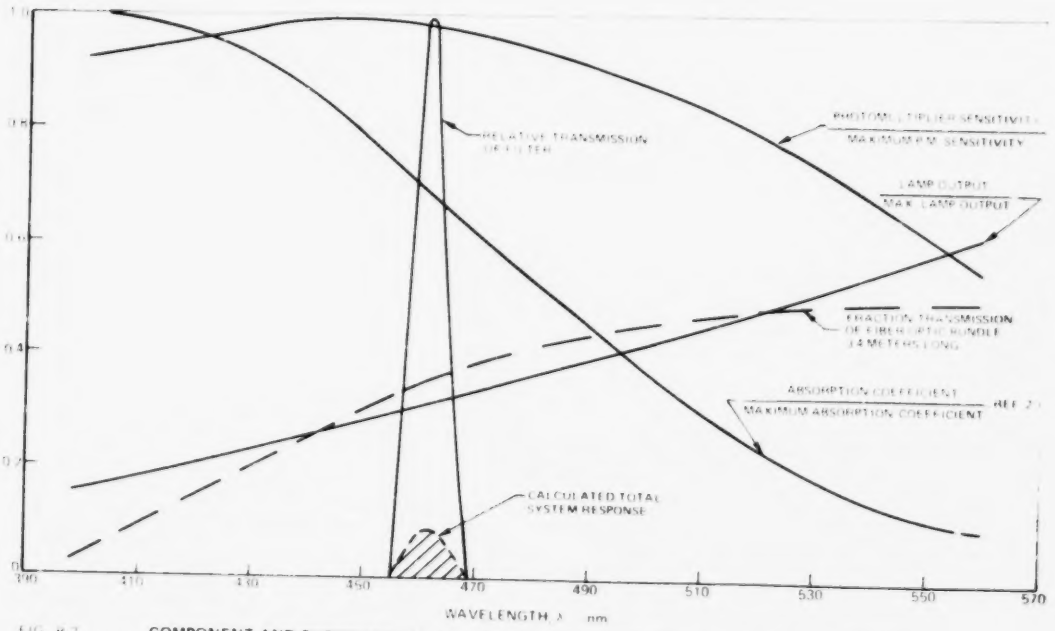

FIG. 8.2 COMPONENT AND SYSTEM PERFORMANCE OF FIBER OPTIC PROBE FOR NO_2–N_2O_4 TRACER

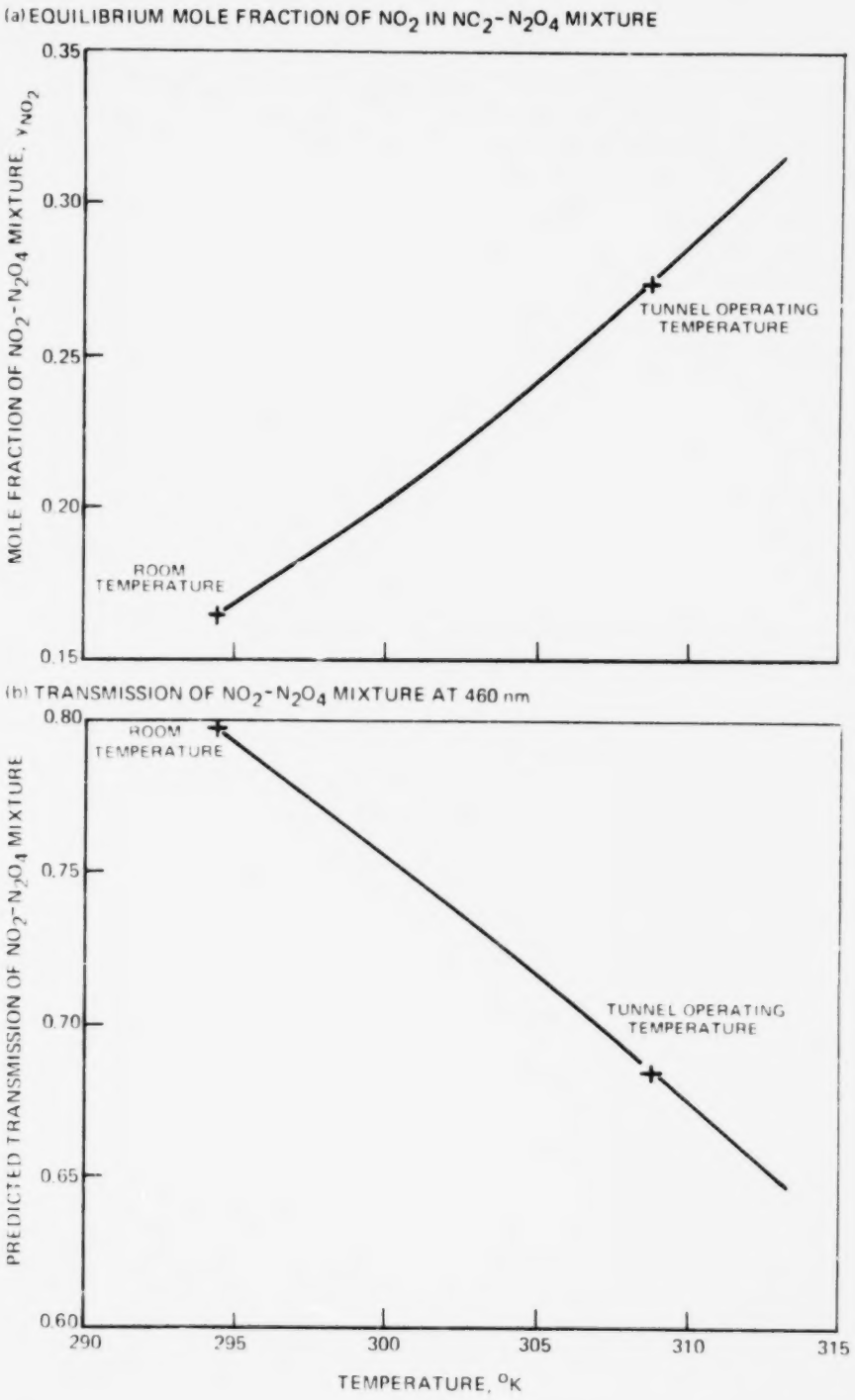

FIG. B-3 PROPERTIES OF NO_2–N_2O_4 TRACER